2016

Design of Surface Texture for the Enhancement of Tribological Performance

Cong Shen
Louisiana State University and Agricultural and Mechanical College

DESIGN OF SURFACE TEXTURE FOR THE ENHANCEMENT OF TRIBOLOGICAL PERFORMANCE

A Dissertation

Submitted to the Graduate Faculty of the
Louisiana State University and
Agricultural and Mechanical College
in partial fulfillment of the
requirements for the degree of
Doctor of Philosophy

in

The Department of Mechanical and Industrial Engineering

by
Cong Shen
B.S., Nanjing University of Aeronautics and Astronautics, 2007
M.S., Nanjing University of Aeronautics and Astronautics, 2010
August 2016

ACKNOWLEDGEMENTS

The author would like to express his sincere appreciation to Dr. Michael M. Khonsari, the major professor and committee chairman, for his continuous support and guidance throughout the period of research at the Louisiana State University. The author would also like to thank Dr. Shengmin Guo, Dr. Guoqiang Li, Dr. Joonyoung Jang and Dr. Guoli Ding for serving as members of the committee. Their valuable advices and help are greatly appreciated.

TABLE OF CONTENTS

ABSTRACT

Surface texturing is a method of surface modification that fabricates micro patterns on the contacting surfaces to improve the tribological performance in sliding, lubricated system. It is found that the geometric design of textures has a significant influence on the performance of textured surfaces. Some important geometric parameters, such as the area ratio and the depth-over-diameter ratio, have been identified for textures in the form of circular dimples.

The current study aims to improve the friction reduction effect of surface texturing by using textures with novel designs. Some new factors considered in the design of textures are: internal structure and geometric shape. A new type of texturing is also proposed for the application in piston rings to reduce engine friction.

In the research on the dimple with internal structures, both experimental and numerical studies are conducted to compare the performance of dimples with three internal structural shapes: rectangle, oblique triangle and isosceles triangle. The numerical model uses Jakobsson-Floberg-Olsson (JFO) cavitation theory to predict the load-carrying capacity of textures. It is found that the value of cavitation pressure plays an important role in the implementation of the JFO theory. Therefore, the analysis on the selection of cavitation pressure is performed for the steady state lubrication. In the work of texture shape optimization, a numerical approach based on the sequential quadratic programming (SQP) algorithm is used to determine the optimum texture shape for different operating conditions, including unidirectional and bidirectional sliding and rotating. The optimization result for rotating is further verified by experiments. For the application of surface texturing in piston rings, a new design of lasered oil pockets is proposed to improve the lubrication at the piston ring/cylinder liner interface. Its friction reduction effect is evaluated with both bench tests of piston ring prototypes and motorized engine tests of production piston rings.

CHAPTER 1 INTRODUCTION

Tribology is the science of friction, wear and lubrication between interacting surfaces in relative motion [1]. It is estimated that the application of tribological principles and practices can result in savings of 1.0% to 1.4% of the GNP of developed countries [2, 3]. A study concentrated on the energy consumption in passenger cars shows that 28% of the fuel energy is used to overcome the friction in engine, transmission and tires [4]. By reducing the friction and wear in automobiles, the savings from reduced fuel usage in the United States are estimated to be up to $ 120 billion per year [5]. Hence, there is now and always will be a need to explore new technologies to improve the tribological performance of machineries. In recent years, surface texturing has emerged as a technical solution for improving lubrication and reducing friction and wear. Its development and mechanism are explained in the following sections.

1.1 Surface Texturing

Surface texturing is a method that fabricates micro patterns — such as dimples, grooves, and etc. — on the contacting surfaces to enhance the tribological performance. Figure 1-1 shows some examples of textured surfaces. One of the earliest work on surface texturing is reported by Hamilton and co-workers in 1966 [9]. They presented a lubrication theory for parallel surfaces with micro-irregularities and pointed out that the addition of micro-patterns can improve the load-carrying capacity. Experimental data of a face seal with etched surface textures was also provided in the paper to verify their theory.

With the development of the micro-machining technologies it has become possible to fabricate micro structures on the surfaces of various materials. As a result, in the last two decades, numerous studies were conducted on the application of surface texturing for enhancing tribological

performance. The reported benefits of textured surface include: increasing load-carrying capacity [10], reducing friction force and wear [11-12], expanding the range of hydrodynamic lubrication [13], and improving seizure resistance [14].

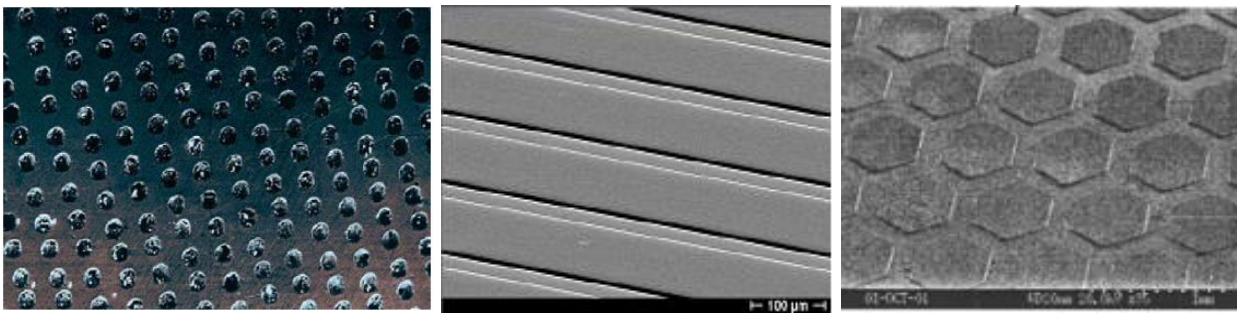

Figure 1-1 Examples of surface patterns. From left to right: micro-dimples by Etsion [6], micro-grooves by Petterson et al. [7] and micro-hexagon asperities by Siripuram et al. [8].

One accepted mechanism for the improved performance is that the textured surface can generate additional hydrodynamic pressure to increase load-carrying capacity (LCC) [10-12]. The micro-textures form a diverging-converging geometry within each dimple or groove. As a result, the lubricant film cavitates in the diverging region and the pressure in this area cannot fall below the cavitation pressure. This leads to an asymmetric pressure distribution and a net force that gives load carrying capacity in each dimple or groove. Other possible mechanisms of surface texturing include: acting as micro oil reservoirs under starved lubrication [15] and trapping wear debris to prevent severe abrasive wear [16].

1.2 Design of Surface Texture

The geometric parameters of surface textures, such as shape, size, orientation and distribution, have a significant influence on the tribological performance. Over the last two decades, a great deal of theoretical and experimental studies has been devoted to study the effect of these geometric parameters. As a result, many important parameters have been identified and investigated, including depth-to-diameter ratio, area ratio and dimple size.

An early work on this subject is carried out by Etsion et al. [17] who developed a numerical model for hydrodynamic lubrication of a textured seal ring and investigated the design parameters of spherical shape dimples. They found that the depth-to-diameter ratio is the most critical parameter and its value should be less than 0.05 for seal parameters greater than 1. Wang et al. [10] experimentally investigated the effects of dimple diameter, depth and area ratio on the performance of SiC thrust bearing under water lubrication. Their results show that the best performance of the textured bearing was obtained when using dimples with diameter of 350 μm, depth of 3.2 μm and area density of 5%. More references on this subject can be found in [18-26]. Table 1-1 lists some

Table 1-1 Preferred geometric designs of surface textures in experimental studies

Author/Year	Testing condition	Shape	Area density	Size (μm)	Depth (μm)	References
Ryk 2002	Steel ring/cast iron liner reciprocating	Circular dimple	13%	100 (diameter)	10	[18]
Wang 2004	Steel /steel pin on disk	Transverse ellipse	7%	150/37.5 (a / b)	8	[19]
Kovalchenko 2005	Steel / steel pin on disk	Circular dimple	12%	78 (diameter)	5.5	[20]
Costa 2007	Brass cylinder/ steel plane reciprocating	Chevron groove	7.3%	35 (width)	4.5	[21]
Galda 2009	Cast iron / steel block on ring	Spherical dimple	12.5%	900 (diameter)	60	[22]
Yan 2010	Chromium coated ring /cast iron ring	Circular dimple	5%	100 (diameter)	10	[23]
Yu 2011	Cast iron / cast iron reciprocating	Transverse ellipse	10.4%	500/80 (2a / 2b)	8-10	[24]
Grabon 2013	Piston ring/cast iron liner reciprocating	Circular dimple	13%	150-200 (diameter)	5	[25]
Vladescu 2015	Steel ring/fused silica reciprocating	Transverse groove	7%	80 (width)	8	[26]

of the preferred geometric designs used in various experimental studies. These geometric parameters correspond to the best tribological performance (lowest friction coefficient or highest film thickness) in each study.

1.3 Research Objective

In order to maximize the beneficial effects of surface texturing, the current research concentrates on the design of surface textures for different applications. New factors, such as internal structure and geometric shape, are considered in the design of textures. Several studies involving cavitation pressure, dimple's internal structure and shape optimization are performed to understand the behavior and design of textured surfaces. For the friction reduction at piston ring/cylinder liner interface, a new type of texturing is proposed for the piston ring surface.

As discussed in previous sections, the load-carrying capacity mechanism for surface textures is believed to be the unsymmetrical pressure distribution caused by cavitation. Therefore, the theoretical model of surface textures needs to predict cavitation accurately. It is found that the value of cavitation pressure can significantly influence the results of Jakobsson-Floberg-Olsson (JFO) cavitation model. In this research, the selection of cavitation pressure for textured surface under steady state lubrication will be discussed in detail based on both experimental and simulation results.

In most published research on the texturing of lubricated surfaces, the hemispherical or cylindrical dimples are commonly used due to the ease in manufacturing. There are very few studies available that investigate the effects of dimple's internal structural shape, which is thought to be an important geometric parameter for hydrodynamic lubrication. A fabrication method to create dimples with different profiles will be developed first. Then the effect of dimple internal structural shape on hydrodynamic lubrication will be studied both experimentally and numerically.

The geometric shape (circular, elliptical, triangular and etc.) is another important factor for the design of surface textures. Previous studies show that some texture shapes, like ellipse or long-drop shape, perform better than others in terms of lowering the friction coefficient or increasing the LCC. However, the global-optimum texture shapes for parallel flat surfaces are still open questions. Thus, this research aims to solve this problem by using numerical optimization methods. And experimental work will also be conducted to verify the theoretical results.

For the application of surface texturing in piston rings, a new design of lasered oil pockets is proposed, which can efficiently enhance the piston ring lubrication and has a lower requirement for the texture fabrication. Both experimental and theoretical studies are needed to investigate the effects of the pocket geometry on the tribological performance.

1.4 Outline

This dissertation presents studies on the novel design of surface textures for the enhancement of tribological performance. Both experimental and theoretical analysis are performed to evaluate the performance of those texture designs under lubrication. Chapter 2 focuses on the choice of cavitation pressure for the numerical simulations of textured surfaces, which lays a solid foundation for the following theoretical analysis of textures. Chapter 3 is on the effect of dimple's internal structure. It presents a method to fabricate dimples with different internal structural shapes and investigates the effect of the internal structure on the lubrication behavior. In Chapter 4, a numerical method for the texture shape optimization is developed. The novel shapes that produces the maximum LCC for unidirectional and bidirectional sliding motion are proposed and analyzed. Chapter 5 applies the numerical method to texture optimization for seal-like specimens under rotary motion. Experimental tests are carried out to compare the performances of optimal textures with those of regular shapes and verify the optimization results. Chapter 6 proposes a new design

of lasered pockets for the friction reduction at the piston ring/cylinder liner interface. The optimal range for geometric parameters of the pockets was found based on experimental and theoretical analysis. Chapter 7 deals with the further verification of the performance of pocketed piston rings. A motorized engine test rig is used to evaluate the tribological and sealing performance of the production piston rings with lasered pockets. Chapter 8 summarizes and concludes the dissertation work. Potential future work on this topic is also suggested.

1.5 References

[1] Khonsari, M. M. and Booser, E. R., 2001, "Applied Tribology-Bearing Design and Lubrication," John Wiley & Sons, Inc., Sussex, UK.

[2] Jost H.P., 1990, "Tribology – Origin and Future," Wear, 136, pp. 1–17.

[3] Jost H.P., 2005, "Tribology micro & macro economics: A road to economic savings," Tribology & Lubrication Technology, 61, pp. 18-22.

[4] Holmberg, K., Andersson, P., Erdemir, A., 2012, "Global energy consumption due to friction in passenger cars," Tribol. Int., 47, pp. 221–34.

[5] Fessler R., 1999, "US department of energy workshop on industrial research needs for reducing friction and wear," Argonne National Laboratory.

[6] Etsion I., 2004, "Improving tribological performance of mechanical components by laser surface texturing," Tribol. Int., 17, pp. 733–737.

[7] Pettersson U., Jacobson S., 2003, "Influence of surface texture on boundary lubricated sliding contacts", Tribol. Int., 36, pp. 857–864.

[8] Siripuram, R.B., Stephens, L.S., 2004, "Effect of deterministic asperity geometry on hydrodynamic lubrication", ASME J. Tribol., 126(3), pp. 527–534.

[9] Hamilton, D.B., Walowit J.A., Allen, C.M., 1966, "A theory of lubrication by micro-irregularities," Transaction of. ASME, Journal of Basic Engineering, 88, pp. 177–185.

[10] Wang X., Kato K., Adachi K., Aizawa K., 2003, " Loads carrying capacity map for the surface texture design of SiC thrust bearing sliding in water," Tribol. Int., 36, pp. 189–97.

[11] Etsion, I., Kligerman Y., 1999, "Analytical and experimental investigation of laser-textured mechanical seal faces," Tribol. Trans., 42, pp. 511–516.

[12] Etsion I., Halperin G., Brizmer V., Kligerman Y., 2004, "Experimental investigation of laser surface textured parallel thrust bearings," Tribol. Lett., 17, pp. 295–300.

[13] Kovalchenko A., Ajayi O., Erdemir A., Fenske G., Etsion I., 2005, "The effect of laser surface texturing on transitions in lubrication regimes during unidirectional sliding contact," Tribol. Int., 38, pp. 219–225.

[14] Wang X., Kato K., 2003, "Improving the anti-seizure ability of SiC seal in water with RIE texturing," Tribol. Lett., 14, pp.275–280.

[15] Pettersson,U., Jacobson, S., 2003, " Influence of surface texture on boundary lubricated sliding contacts," Tribol. Int. 36, pp. 857–864.

[16] Suh, N.P., Mosleh, M., Howard, P.S., 1994, "Control of Friction," Wear, 175, pp. 151–158.

[17] Etsion, I., and Burstein, L., 1996, "A model for mechanical seals with regular micro surface structure," Tribol. Trans., 39, pp. 677–683.

[18] Ryk G., Kligerman Y., Etsion I., 2002, "Experimental investigation of laser surface texturing for reciprocating automotive components," Tribol. Trans., 45, pp. 444 - 449.

[19] Wang, X., S.M. Hsu, 2004, "An integrated surface technology for friction control: a new paradigm effects of geometric shapes on friction", in The 4th China International Symposium on Tribology. Xi'an.

[20] Kovalchenko A., Ajayi O., Erdemir A., Etsion I., 2005, "The effect of laser surface texturing on transitions in lubrication regimes during unidirectional sliding contact," Tribol. Int., 38, pp. 219-225.

[21] Costa H.L., Hutchings I.M., 2007, "Hydrodynamic lubrication of textured steel surfaces under reciprocating sliding conditions," Tribol. Int., 40, pp. 1227-1238.

[22] Galda L., Pawlus P., and Sep J., 2009, "Dimples shape and distribution effect on characteristics of Stribeck curve," Tribol. Int., 42, pp. 1505-1512.

[23] Yan D., Qu N., Li H., Wang X., 2010, "Significance of Dimple Parameters on the Friction of Sliding Surfaces Investigated by Orthogonal Experiments," Tribol. Trans., 53, pp. 703-712.

[24] Yu H., Deng H., Wang X., 2011, "The effect of dimple shapes on friction of parallel surfaces", Proc. IMechE. Part J: J. Engineering Tribology, 225, pp. 693-703.

[25] Grabon W., Koszela W., Pawlus P., Ochwat S., 2013, “Improving tribological behavior of piston ring–cylinder liner frictional pair by liner surface texturing,” Tribol. Int., 61, pp. 102-108.

[26] Vladescu S.C., Olver A.V., Pegg I.G., Reddyhoff T., 2015, “The effects of surface texture in reciprocating contacts – An experimental study,” Tribol. Int., 82, 28-42.

CHAPTER 2 ON THE MAGNITUDE OF CAVITATION PRESSURE OF STEADY-STATE LUBRICATION [1]

2.1 Introduction

Cavitation is a phenomenon that describes the formation of vapor bubbles in a liquid upon reduction in pressure. In fluid-film lubrication, two types of cavitation are recognized: gaseous cavitation and vapor cavitation. Lubricating oil usually contains dissolved gas. Gaseous cavitation forms when the oil pressure falls below the atmospheric saturation pressure and the dissolved gas comes out of the solution. If the pressure is further reduced to below that of the vapor pressure, then the oil begins to boil and bubbles are formed, causing vapor cavitation [1]. Regardless of the forms of cavitation, however, they represent a rupture in the lubricant film and this effect can affect the tribological performance considerably. Much attention has been devoted to the study of cavitation under steady-state lubrication [2-16].

There are several models available to take into account the effect of cavitation in hydrodynamic lubrication. The well-known boundary conditions are: Gumbel (half-Sommerfeld), Swift-Stieber (Reynolds) and Jakobsson-Floberg-Olsson (JFO) [1]. They were first implemented in dealing with prediction of pressure in a journal bearing wherein the geometric configuration involves a convergent-divergent gap. In the divergent film region, the oil pressure drops below the ambient pressure and hence cavitation occurs. Among these models, the JFO boundary conditions is considered to be the most realistic, for it accounts for both film rupture and film reformation and satisfies mass conservation. According to JFO theory, the magnitude of the pressure in the entire cavitation region remains constant at the cavitation pressure P_{cav}, which is "predetermined".

[1] This chapter previously appeared as Shen C., Khonsari M. M., "On the magnitude of cavitation pressure of steady-state lubrication", Tribology Letters, 51(2013), pp. 153-160. It is reprinted by permission of Springer.

The film rupture starts at the location where the pressure derivative with respect to the normal direction is zero. The film reformation boundary is described by the following formula:

$$\frac{h^2}{12\mu}\frac{\partial p}{\partial n} = \frac{V_n}{2}\left(1-\frac{\rho}{\rho_c}\right) \tag{1}$$

where V_n is the fluid velocity in normal direction, ρ and ρ_c are local and cavitation density of the fluid. However, because of the complexities of locating film rupture and reformation boundaries, the implementation of the JFO boundary conditions is quite cumbersome.

Major progress was made by Elrod and Adam [7] who developed a universal form of Reynolds equation to implement the JFO theory, which can describe both the full-film and the cavitated region and also automatically distinguish the cavitation boundaries. Known as Elrod's mass–conservative algorithm, this feature was realized by incorporating using a switch function, g, as a cavitation index and a dimensionless variable θ ($=\rho/\rho_c$) as fractional film content in cavitated region. When $\theta \geq 1$ or $P \geq P_{cav}$, $g(\theta)=1$ and lubricating flow operates in full-film region. When $\theta<1$ or $P<P_{cav}$, $g(\theta)=0$ and the flow in the cavitation region. Vijayaraghavan and Keith [10, 11] improved the Elrod's algorithm to avoid the trial-and-error step and enhance the computational efficiency. The simulation results from Elrod's algorithm are validated by comparing to the experimental results of Jakoboson and Floberg [3] and Brewe [9]. Nowadays, the mass-conserving JFO theory and its numerical implementation (Elrod algorithm) are widely used for cavitation simulation in different applications, such as in journal bearings [10], in seals [17] and recently in evaluation of performance of surface textures [18, 19]. However, the JFO theory may not fully explain the cavitation phenomenon under steady state lubrication and further work will be needed to develop the theory. Etsion and Ludwig [8] reported that in their experiment of submerged journal bearing the pressure in cavitation zone, measured by a travelling pressure transducer, is significantly not constant. This is contrary to the assumption of JFO boundary conditions. Also, a reverse flow in

cavitation region is observed in the visualization tests. Later, Groper and Etsion [12, 13] developed a new cavitation model with consideration of reverse flow. The JFO boundary conditions also neglect the effect of surface tension, which could be important for oil-gas interface. Coyne and Elrod [5, 6] developed new boundary conditions with the effects of gravity, inertia and surface tension and applied them to an infinitely wide sider bearing. Though this paper focuses on cavitation pressure for mass conservative algorithm and does not consider the above affects, the interested reader can refer to the above-mentioned references.

2.2 Cavitation Pressure in Journal Bearing

Elrod's computational scheme requires specification of the cavitation pressure *P*cav. The choice of cavitation pressure can affect the location and area of cavitation region significantly. Unfortunately, pertinent data on cavitation pressure of lubricant oil are not readily available in the literature. Consequently, published papers have resorted to different assumptions on the magnitude of the cavitation pressure. For steady-state lubrication analysis, the cavitation pressure is commonly assumed to be equal to the ambient pressure, i.e. *P*cav=0 (gage) or 101.325 kPa (absolute). However, different experimental tests report sub-ambient pressures in the lubricant film. For example, Jakoboson and Floberg [3] measured the circumferential pressure distribution in a plain journal bearing (without oil groove) submerged in oil. They presented two non-dimensional cavitation pressures, $\overline{P_c} = -1$ and $\overline{P_c} = -0.1$, depending on the operating conditions. These correspond to the dimensional pressure of -72.137 kPa (gauge) and -5.612 kPa (gauge). Floberg [4] also carried out tests in journal bearing with an axial groove wherein the supply lubricant was nearly at the atmospheric pressure. The measured cavitation pressures are around -10 kPa (gauge) and slightly different under different conditions.

Table 2-1 lists the cavitation pressures and corresponding operating conditions in the two experiments by Jakoboson and Floberg [3] and Floberg [4]. As shown in Table 2-1, the cavitation pressure of steady-state journal bearing depends on the operating conditions, i.e. the lubricant supply and the load. According to their results, in a journal bearing with oil groove, the cavitation pressure is around 90 kPa. In the case of the submerged bearing, the cavitation pressure varies with the applied load. Results indicate that under low load, the cavitation pressure is close to that of the grooved bearing. However, under high load, its value is as low as 29.2 kPa.

Table 2-1 Operating conditions for different cavitation pressures of journal bearing

	Case 1	Case 2	Case 3	Case 4
P_{cav} (kPa, gage)	-72.1	-5.6	-10.0	-15.0
P_{cav} (kPa, absolute)	29.2	95.7	91.3	86.3
Lubricant supply	submerged	submerged	axial groove	axial groove
Load (N)	2250	620	9585	8640
Journal diameter (mm)	100	100	100	100
Bearing width (mm)	133	100	135	135
Radial clearance (C/R)	0.00291	0.00364	0.00825	0.00825
Viscosity (Pa·s)	0.0127	0.0153	0.0161	0.0161
Rotational speed (rad/s)	48.1	48.6	64.4	64.4
Eccentricity ratio (e/C)	0.60	0.60	0.51	0.53

2.3 Cavitation Pressure in Textured Surfaces

One accepted mechanism associated with enhancement of performance of textured surfaces is the capability to generate additional hydrodynamic pressure to increase load carrying capacity [20-24]. Surface textures form a diverging-converging geometry within each dimple or groove. Hence, it is argued that the lubricant film cavitates within the diverging region. Due to the effects of cavitation, the pressure in the diverging zone cannot fall below the cavitation pressure and this leads to an asymmetric pressure distribution and a net force that gives load carrying capacity in each dimple or groove.

Early attempts at prediction of the load-carrying capacity of textured surfaces involved the use of Swift-Stieber (Reynolds) boundary condition. Good agreement between theoretical predictions using Reynolds boundary condition and experimental results was reported at the high load range [21, 22]. More recently the JFO theory and Elrod algorithm are applied. Ausas et al. [18] compared simulation results in a micro-textured journal bearing using the Reynolds boundary condition with that of the mass-conserving model proposed by Elrod and Adams. They found that Reynolds boundary condition largely underestimated the cavitation area. Qiu and Khonsari [19] applied JFO theory to predict the pressure distribution in dimpled surface of a seal-like structure and compared it with half-Sommerfeld and Reynolds boundary conditions. The results showed the load carrying capacity calculated by JFO theory is the smallest and Reynolds and half-Sommerfeld boundary conditions overestimate the pressure generation in a dimple. However, the choice of cavitation pressure used in the simulation of surface textures with JFO model is problematic, because it is an assumed value. Qiu and Khonsari [25] conducted simulations of a single dimple with different cavitation pressures ranging from 95 kPa to 0 Pa to examine the effects of cavitation pressure on load-carrying capacity. The results showed that the cavitation pressure can significantly affect the

predicted load-carrying capacity of dimpled surface. Yet specification of cavitation pressure for steady state lubrication still remains to be an open problem. In the following sections, the authors begin by first examining the results of published papers and subsequently introduce a method for specifying the cavitation pressure. Further, a mechanism is proposed to explain the variation of cavitation pressure. The results of series of experiments are presented to authenticate the proposed mechanism.

2.4 Cavitation Morphology in Surface Textures

Recent experimental results to visualize the cavitation zone within surface textures and comparison with simulations using the JFO theory sheds some light on the value of cavitation pressure. Zhang and Meng [26] investigated the cavitation morphology and frictional behavior of grooved parallel thrust bearings, both experimentally and theoretically. In their simulations, three cavitation pressure values of 10, 30 and 90 kPa were used and compared. The results showed that the cavitation zone and friction coefficient in steady-state matched with the predicted results using the JFO model with cavitation pressure of 30 kPa. It is also found that the simulation results of JFO model is strongly influenced by the cavitation pressure. Usually, a higher cavitation pressure predicts a larger cavitation zone. Cross et al. [27] developed a thrust washer test rig to visualize cavitation inside a cylindrical pocket and measure friction of the pocketed washer. They applied the Schnerr and Sauer method in ANSYS Fluent software with the cavitation pressure of 100 kPa to determine the cavitation zone. They reported that the simulation results closely correlated with the experiment results. Table 2-2 summarizes the visualization investigations on cavitation within surface textures [19, 26, 27]. The cavitation morphology of experiment and simulations is shown in Figure 2-1 [19, 26, 27]. It can be seen that even though the simulations show good agreement with experimental results the choice of cavitation pressure varies widely.

Table 2-2 Visualization investigations on the cavitation within surface textures

Reference	Test type	Lubricant supply	Texture type	Theoretical model	Cavitation pressure
Qiu et al.[19]	ring-on-ring	submerged	hemispherical dimple	JFO	90 kPa
Zhang et al.[26]	ring-on-ring	submerged	radial groove	JFO	30 kPa
Cross et al.[27]	ring-on-ring	submerged	cylindrical dimple	Fluent	100 kPa

2.5 Analysis of Cavitation Pressure

In order to find a suitable cavitation pressure for surface textures, the authors used the modified Elrod algorithm, proposed by Vijayaraghavan and Keith [10, 11], to simulate the experiments with different cavitation pressures. The simulations were carried out for experiments of Zhang et al. [26] and Cross et al. [27]. Figure 2-2 shows the simulation results. By comparing with experimental results in Figure 2-1, it can be observed that the simulations with cavitation pressure of 90 kPa overestimate the cavitation region. The cavitation pressure of 30 kPa seems to be reasonable for surface textures, and this agrees with the findings of Zhang and Meng [26] (refer to Figure 2-1 b).

Both direct test of journal bearing and simulation of surface textures validate a low cavitation pressure around 30 kPa. However, in view of experiments of Floberg [4], for example, a cavitation pressure close to ambient pressure was also observed. This raises the question of how does one properly specify the cavitation pressure?

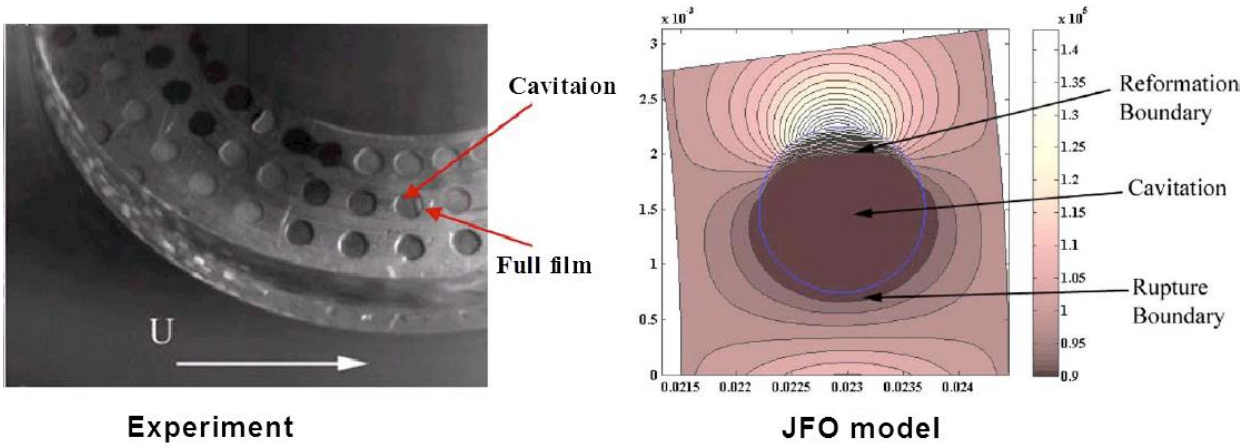

(a)

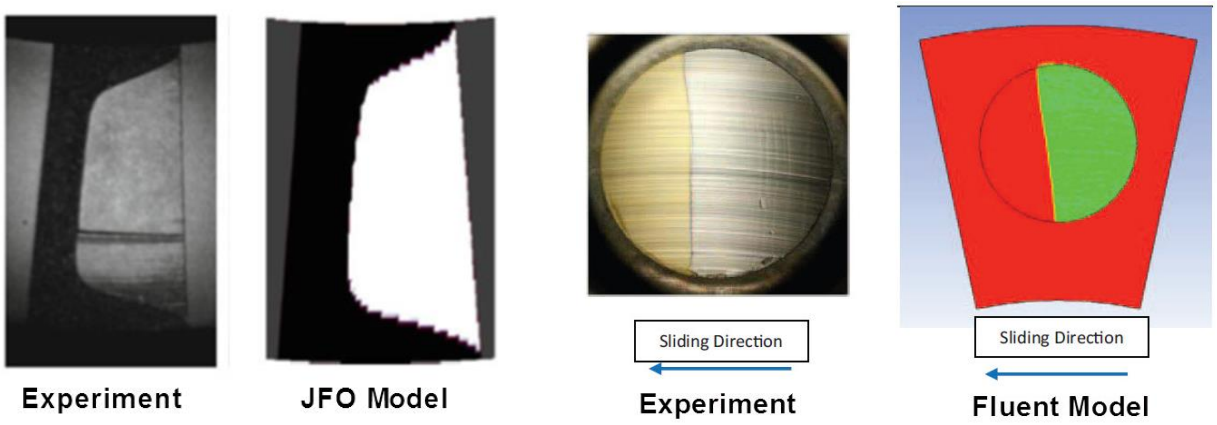

(b) (c)

Figure 2-1 Cavitation morphology of experiment and simulation (a) results from Qiu et al. [19]; (b) results from Zhang et al. [26]; (c) results from Cross et al. [27]

Examination of the results indicates that the cavitation pressure is affected by the replenishment of lubricant. Low cavitation pressure occurs in submerged lubrication for both steadily-loaded journal bearing and textured parallel thrust bearing while a journal bearing lubricated by an oil groove always has a cavitation pressure close to the ambient pressure. As mentioned in Section 2.1, there are two types of cavitation in fluid film lubrication: gaseous and vapor. Since the vapor pressure of lubricant oil is very low, the cavitation in steady-state lubrication is commonly gaseous. The gas in cavitation zone is supplied from the emergence of air dissolved in the oil out of the solution.

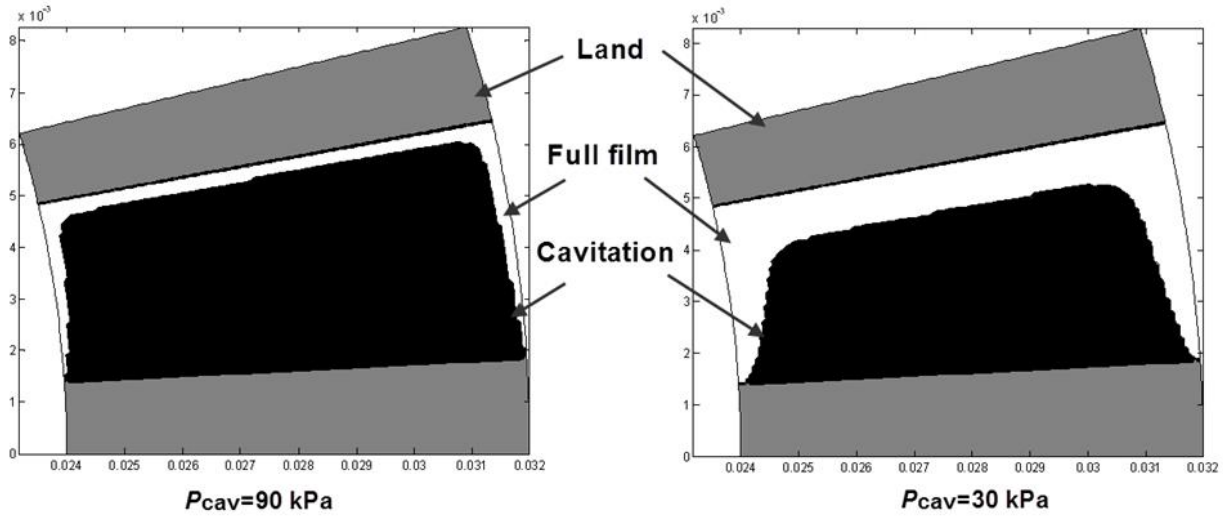

(a)

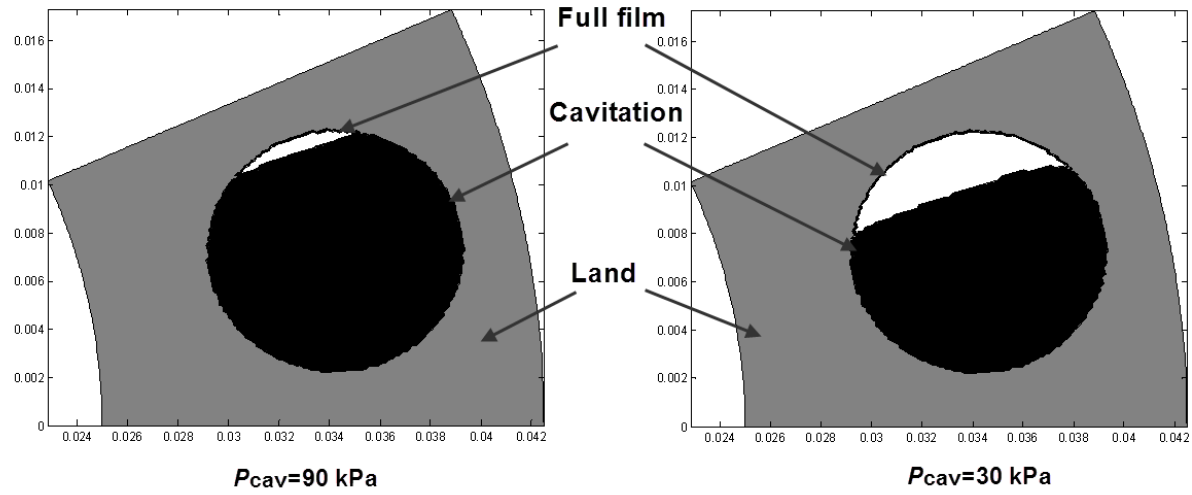

(b)

Figure 2-2 Simulation results with different cavitation pressures for (a) Zhang and Meng experiment [26]; (b) Cross et al. experiment [27]

In the case of submerged lubrication, oil can only be supplied at the bearing sides. When the film thickness is small, the amount of fresh oil that flows into the bearing is limited. As a result, the air released from the oil is insufficient to form a large cavitation zone and the lubricant film can sustain a low cavitation pressure. However, in a journal bearing lubricated with an oil groove, a large amount of fresh oil can be supplied into the bearing with additional air content to the cavitation

region. Consequently, the cavitation pressure is likely to be close to the saturation pressure, i.e. near the atmospheric pressure.

To sum up, a review of the available research publications reveals that the cavitation pressure in steady-state lubrication film can be depending on the operating conditions and that its value is affected by the gas supply from the oil film. If the gas emitted from lubricant film is sufficient to form the cavitation zone, the cavitation pressure will be close to ambient pressure. Otherwise, a sub-ambient pressure, as low as 30 kPa, can be reached in lubricant film.

2.6 Experimental Validation

In this section, we present an investigation of the load-carrying capacity in a textured surface to confirm the validity of the concluding statements in previous section. Specifically, the load carrying capacity of large dimples on parallel thrust bearing is studied both experimentally and theoretically. In the experiment, a torsional rheometer (MCR 301, Anton Paar Inc.) equipped with tribology accessory unit is used. The apparatus allows one to control the rotating speed (10^{-5} to 3000 rpm), the gap width (1 to 1000 μm) and the temperature (-40 to 200°C). The recorded normal force provides the measurement of the specimen's load-carrying capacity under a specified gap and speed. The measurement of load-carrying capacity involves maintaining a constant gap between the upper plate and the lower specimen and measuring the normal force produced by textured surface. A schematic of the test rig and textured lower specimen are shown in Figure 2-3. Table 2-3 lists the specimen parameters and test conditions. The lower specimen is made of stainless steel (17-4 PH) with 10 cylindrical dimples located at the median radius. After laser texturing of the dimples, it is polished to achieve a surface roughness (Ra) of 0.05 μm for un-textured area. During the experiment, the bulk temperature of lubricant and rotational speed are kept constant, while the gap between upper plate and lower specimen is increased in a stepwise

fashion. The test period of each gap is 3 minutes, and the reported values correspond to stable data averaged over the last minute. Also, an Elrod algorithm with different cavitation pressures was applied to simulate the experiment. By comparing the simulation results of different cavitation pressures, it is found that the cavitation pressure can influence the load-carrying capacity significantly but has little effect on the friction torque. Hence, the experimental and theoretical results of load-carrying capacity are compared to reveal the value of cavitation pressure for textured surface.

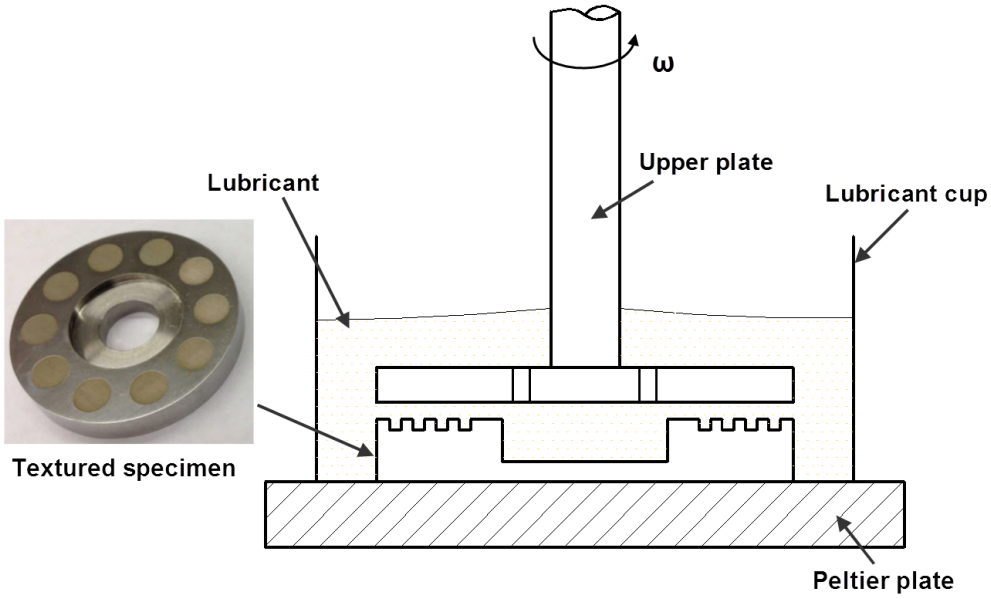

Figure 2-3 Load-carrying capacity test rig and specimen

Figure 2-4 shows the comparison between experimental and simulation results. It can be seen that the simulation results using the cavitation pressure of 30 kPa match test results in the small-gap region (gap < 40 μm). However, as the gap increases the experimental results become closer to simulation results with cavitation pressures of 60 kPa and 90 kPa. This means the cavitation pressure in the test tends to increase as the gap increases. In order to confirm this phenomenon, load-carrying capacity tests are carried out with small and large gaps separately. During the tests,

the gap is maintained at 30 μm for small gap and 80 μm for large gap, while the rotational speed is increased from 200 to 800 rpm. Figure 2-5 presents the test and simulation results under the two gaps. The same trend can be observed that the test results are closer to the simulation results with a higher cavitation pressure as the gap is increased.

Table 2-3 Parameters of specimen and test conditions

Inner diameter (mm)	Outer diameter (mm)	Dimple diameter (mm)	Dimple depth (μm)	Rotating speed (rpm)	Gap distance (μm)	Dimple shape	Lubricant
19	38	6	26.5	600	29~80	cylindrical	SAE 30

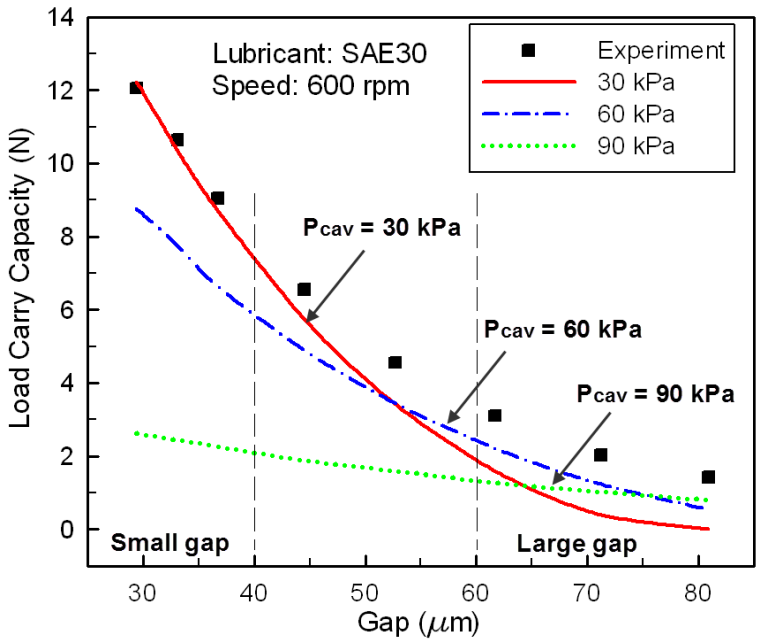

Figure 2-4 Comparison between experimental and simulation results under different gaps

This phenomenon can be explained as follows. In this experiment, the lubricant is supplied into the gap from the sides of the bearing. When the gap is small, the oil flow is limited and very little air is supplied to the oil film, causing a low cavitation pressure. As the gap increases, more fresh

oil flows into the lubrication region with dissolved air, which leads to a higher cavitation pressure. Therefore, the cavitation pressure should be treated as a variable and depend on the operating conditions in the experiment.

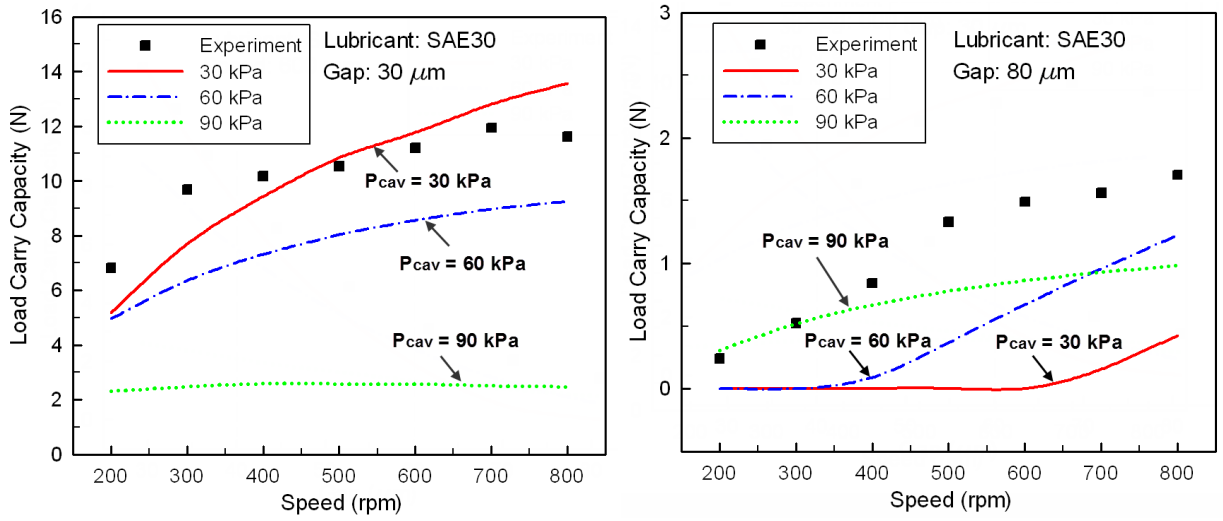

(a) (b)

Figure 2-5 Comparison between experimental and simulation results under different speeds (a) small gap (b) large gap

2.7 Conclusions

The choice of cavitation pressure P_{cav} can strongly influence the simulation results from Elrod algorithm which implements the JFO theory. Yet no guideline is available for choosing a reasonable cavitation pressure in steady-state lubrication. This paper attempts to provide some insights into this problem by analyzing previous researches on cavitation. A common practice in lubrication simulation is to approximate the cavitation pressure to ambient pressure or saturation pressure (only a few percent below ambient pressure). However, this may not apply to all situations. According to the experiments of journal bearing and cavitation visualization in textured surface, low gaseous cavitation pressure around 30 kPa is possible. The JFO model using cavitation pressure of 90 kPa usually overestimates the cavitation region and underestimates the load-

capacity of surface textures comparing with experiment results. Based on the mechanism of cavitation, it proposed that the cavitation pressure in steady-state lubrication film is affected by the gas supply from the oil film. If the gas emitted from lubricant film is sufficient to form the cavitation zone, the cavitation pressure will be close to ambient pressure. Otherwise, a sub-ambient pressure, as low as 30 kPa, can be reached in lubricant film. This assumption is supported by an investigation of textured surface's load-carrying capacity. The comparison of the experimental and simulation results shows that the cavitation pressure increases with the increasing gap. A possible reason is that as the gap increases more fresh oil flows into the lubrication region, bringing in more dissolved air. With sufficient air supply, the cavitation pressure becomes close to the saturation pressure.

2.8 References

[1] Khonsari, M. M. and Booser, E. R., 2001, "Applied Tribology-Bearing Design and Lubrication," John Wiley & Sons, Inc., Sussex, UK.

[2] J.A. Cole, C.J. Hughes, 1956, "Oil flow and film extent in complete journal bearings," Proceedings of the Institution of Mechanical Engineers, 170, pp. 499-510.

[3] Jakobsson, B. and Floberg, L., 1957, "The finite journal bearing considering vaporization," Report No.190, Transactions of Chalmers University of Technology, Guthenburg, Sweden.

[4] Floberg, L., 1957, "The finite journal bearing considering vaporization," Report No.189, Transactions of Chalmers University of Technology, Guthenburg, Sweden.

[5] Coyne, J.C. and Elrod H.G., 1970, "Conditions for the rupture of a lubricating film, Part I: theoretical model," J. Lubric. Technol., 92, pp. 451-456.

[6] Coyne, J.C. and Elrod H.G., 1970, "Conditions for the rupture of a lubricating film, Part II: new boundary conditions for Reynolds equation," Transactions of the ASME, No.70-lub-3.

[7] Elrod, H. G. and Adams, M., 1974, "A computer program for cavitation," 1st Leeds-Lyon Symposium on Cavitation and Related Phenomena in Lubrication, I.M.E., Mechanical Engineering Publication, New York, 103, pp. 37-41.

[8] Etsion, I., Ludwig, L.P., 1982, "Observation of pressure variation in the cavitation region of submerged journal bearings," J. Lubr. Technol. Trans. ASME, 104, pp. 157–163.

[9] Brewe, D. E., 1986, "Theoretical modeling of the vapor cavitation in dynamically loaded journal bearings," ASME Journal of Tribology, 108, pp.628-638.

[10] Vijayaraghavan, D. and Keith, T. G. Jr., 1990a, "An efficient, robust and time accurate numerical procedure applied to a cavitation algorithm," ASME Journal of Tribology, 112, pp.44-51.

[11] Vijayaraghavan, D. and Keith, T. G. Jr., 1990b, "Grid transformation and adaption techniques applied to the analysis of cavitated journal bearings," ASME Journal of Tribology, 112, pp.52-59.

[12] Groper, M., Etsion, I., 2001, "The effect of shear flow and dissolved gas diffusion on the cavitation in a submerged journal bearing," J. Tribol. Trans. ASME, 123, pp. 494–500.

[13] Groper, M., Etsion, I., 2002, "Reverse flow as a possible mechanism for cavitation pressure build-up in a submerged journal bearing,"J. Tribol. Trans. ASME, 124, pp. 320–326.

[14] Kasolang S., Dwyer-Joyce R. S., 2008, "Observations of film thickness profile and cavitation around a journal bearing circumference," Tribology Transactions, 51, pp. 231-242.

[15] Braun, M.J., Hannon, W.M., 2010, "Cavitation formation and modelling for fluid film bearings: a review," Proc. Inst. Mech. Eng. J, 224, pp. 839–863.

[16] Matteo Giacopini, Mark T. Fowell, Dini Daniele, Antonio Strozzi, 2010, "A Mass-Conserving Complementarity Formulation to Study Lubricant Films in the Presence of Cavitation," J. Tribol. Trans. ASME 132, 041702-1.

[17] Salant R F, Homiller S.J., 1992, "The effect of shallow groove patterns on mechanical seal leakage," Tribology Trans, 35(1), pp. 142-148.

[18] Ausas, R., Ragot, P., Leiva, J., Jai, M., Bayada, G., and Buscaglia, G., 2007, "The impact of the cavitation model in the analysis of micotextured lubricated journal bearing," ASME Journal of Tribology, 129, pp. 868-875.

[19] Qiu, Y. and Khonsari, M. M., 2009, "On the prediction of cavitation in dimples using a mass-conservative algorithm," ASME Journal of Tribology, 131, pp. 041702:1-11.

[20] Etsion, I, 2005, "State of the Art in Laser Surface Texturing," ASME Journal of Tribology, 127, pp. 248-253

[21] Etsion, I., Halperin, G., Brizmer, V., Kligerman, Y., 2004, "Experimental investigation of laser surface textured parallel thrust bearings," Tribology Letters, 17, pp.295–300.

[22] Ryk, G., Kligerman, Y., Etsion, I., 2002, "Experimental investigation of laser surface texturing for reciprocating automotive components," Tribology Transactions, 45, pp. 444–449.

[23] Wang, X., Kato, K., Adachi, K., Aizawa, K., 2003, "Loads carrying capacity map for the surface texture design of SiC thrust bearing sliding in water," Tribology International, 36, pp. 189–197.

[24] Qiu, Y. and Khonsari, M. M., 2011, "Experimental investigation of tribological performance of laser textured stainless steel rings," Tribology International, 44, pp. 635-644.

[25] Qiu, Y. and Khonsari, M. M., 2011 "Performance analysis of full-Film textured surfaces with consideration of roughness effects," ASME Journal of Tribology, 133, pp.021704:1-10.

[26] Zhang, J. Y. and Meng, Y. G., 2012 "Direct observation of cavitation phenomenon and hydrodynamic lubrication analysis of textured surfaces," Tribology Letters, 46, pp.147-158.

[27] Cross, A. T., Sadeghi, F., Cao, L. J., Rateick, R. G. and Rowan, S., 2012, "Flow visualization in a pocketed thrust washer", Tribology Transactions, 55, pp. 571-581.

CHAPTER 3 EFFECT OF DIMPLE INTERNAL STRUCTURE ON HYDRODYNAMIC LUBRICATION [2]

3.1 Nomenclature

g Switch Function

h Local film thickness (m)

h_0 Minimum film thickness (m)

h_d Dimple depth (m)

$\bar{h}$ Dimensionless local film thickness, h/h_0

p Local Pressure (Pa)

p_a Ambient pressure (Pa)

p_c Cavitation Pressure (Pa)

$\bar{p}$ Dimensionless pressure, p/p_a

r Local coordinate in radial direction (m)

r_i Inner radius of the specimen (m)

r_o Outer radius of the specimen (m)

r_d Dimple radius (m)

r_c Radial coordinate of the dimple center (m)

$\bar{r}$ Dimensionless radial coordinate, r/r_i

[2] This chapter previously appeared as Shen C., Khonsari M. M., "Effect of dimple's internal structure on hydrodynamic lubrication", Tribology Letters, 52 (2013), pp. 415-430. It is reprinted by permission of Springer.

$\bar{T}$ Dimensionless frictional torque

$\bar{W}$ Dimensionless load-carrying capacity

β Bulk modulus of the lubricant (Pa)

ε Convergence criterion

θ Angular coordinate (rad)

θ_0 Angular extent of one sector (rad)

θ_c Angular coordinate of the dimple center (rad)

φ Film content parameter

μ Lubricant viscosity (Pa.s)

λ Characteristic number, $6\mu\omega r_i^2/\beta h_0^2$

ρ Local fluid density (kg/m^3)

$\bar{\tau}$ Dimensionless shear stress, $\tau h_0/\mu_0\omega_0 r_i$

ω Angular velocity of the upper specimen (rad/s)

3.2 Introduction

Surface texturing is an effective method to improve tribological performance of mechanical parts. It involves creating micro patterns — such as dimples, grooves, and etc. — on the contacting surfaces to improve the frictional behavior. In recent years, a great deal of effort has been devoted to study the effects of texture's geometric parameters [1-16]. One of the often cited literatures on the subject is the work of Etsion et al. [2] who developed an analytical model for hydrodynamic

lubrication of a seal ring textured with micro-pores. They found that the ratio of dimple's depth over the diameter has significant effect on the performance and that there exists an optimum value which yields the highest load-carrying capacity (LCC). Wang et al. [4] experimentally investigated the performance of water-lubricated dimpled SiC thrust bearings and reported values of diameter, depth and area ratio of the dimples that result in optimum LLC. Qiu and Khonsari [7] studied the tribological performance of dimpled surface by a mass-conserving algorithm with consideration of surface roughness. Their conclusions also show that there exists optimum dimple depth and dimple density that produce the highest LCC. The optimum parameters are highly dependent on the operating conditions. Besides, the effects of some other geometrical characteristics of surface textures, such as partial texturing, texture region, shape effect and orientation effect are also discussed in literatures [3, 11, 12, 14].

In most published research on the surface texturing of lubricated surfaces, the dimple internal structure is uniform. Because of the ease in manufacturing, the commonly explored dimples are hemispherical or cylindrical with semicircular or rectangular cross-sections. There are very few studies available that investigate the effects of dimple's internal structural shape, which is thought to be an important geometric parameter for hydrodynamic lubrication. Notably, Nanbu et al. [9] applied an elasto-hydrodynamic lubrication (EHL) model to evaluate the EHL performance of different texture bottom shapes. They demonstrated that dimples with flat bottom and those that form a convergent wedge can yield thicker lubrication film under a constant load.

In this paper, both experimental and numerical analyses of dimple internal structural shape's effects are presented. For this purpose, a fabrication technique for constructing dimples with different profiles was developed. The load-carrying capacities generated by dimples with different internal structures were examined as a function of rotational speed, film thickness and viscosity.

Furthermore, prediction of cavitation and pressure distribution for different dimple internal structures are presented based on the numerical simulations that apply a mass-conservative algorithm implementing the Jakobsson-Floberg-Olsson (JFO) boundary conditions.

3.3 Experiment

3.3.1 Test Rig

A versatile torsional rheometer (MCR 301, Anton Paar Inc.) equipped with tribology accessory is used in the experimental testing. It allows one to control the rotating speed, gap width and temperature, and is capable of measuring normal force (-50 to 50 N with an accuracy of ±0.03N) and the frictional torque (0 to 200 mN·m with an accuracy of 0.2 μN·m). The rheometer is also equipped with a Peltier plate, which is capable of controlling the temperature in the range of -40 to 200°C while maintaining the bulk temperature of lubricant to within ±1°C. The tribology accessory enables this rheometer to function as a high resolution tribometer [17]. The apparatus works with a "parallel-disk" type configuration submerged in a lubricant in a specially-designed cup, as shown in Figure 3-1.

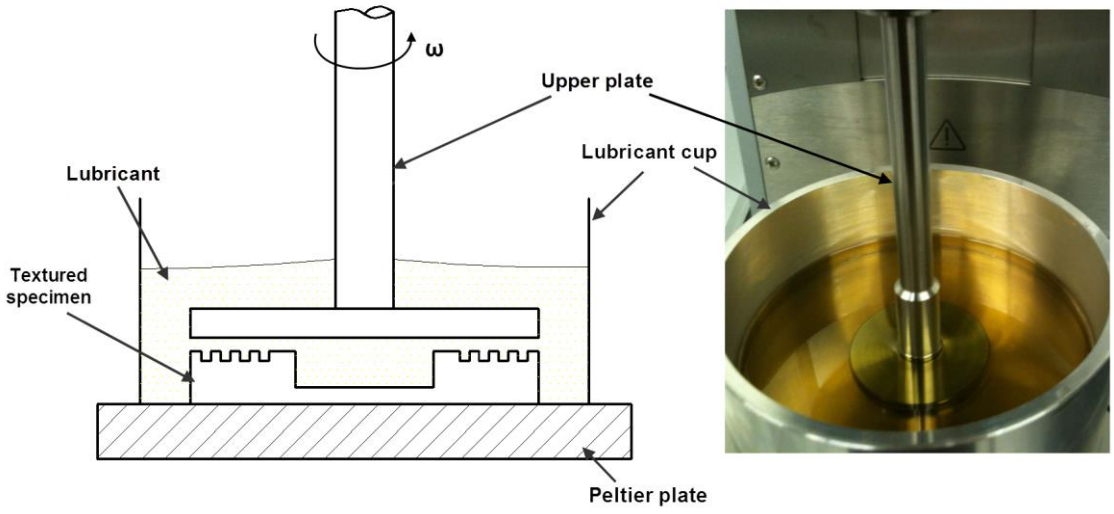

Figure 3-1 A schematic and photo of the test rig

Tests were conducted to determine the LCC of different dimples. The test procedure involves maintaining a constant gap between the upper plate and the lower textured specimen and measuring the normal force produced by textured surface under different rotating speeds.

3.3.2 Specimens: Materials and Preparation Procedure

The upper plate is the rotating disk with a smooth surface (roughness average Ra = 0.04 μm). Dimples were created on the surface of the stationary lower specimen. Both the rotating disk and the specimen were made of stainless steel (17-4 PH). The diameter of upper disk is 40 mm. The lower specimen's inner and outer diameters are 19 and 38 mm, respectively.

A laser marking system (Electrox Inc.) was used to fabricate texture patterns on the specimen surface. The design of patterns was first generated with CAD software and then imported into the laser machine. The machine uses Nd:Ytterbium fiber laser to remove material from specimen and engrave the desired patterns. The depth of patterns can be controlled by the number of times that laser scans the area since the laser beam removes the same amount of material during each pass. Figure 3-2 shows the linear relationship between the number of repeats and pattern depth for the material of specimen.

Shown in Figure 3-3 are dimples with various internal structural shapes manufactured by dividing a circular dimple into many segments along its centerline in which each segment has a specific depth. The depth of each part within a dimple is controlled by the number of laser scanning repeats within that area. In this study, three types of dimple profile were made for comparison: rectangle (R), oblique triangle (T1) and isosceles triangle (T2).

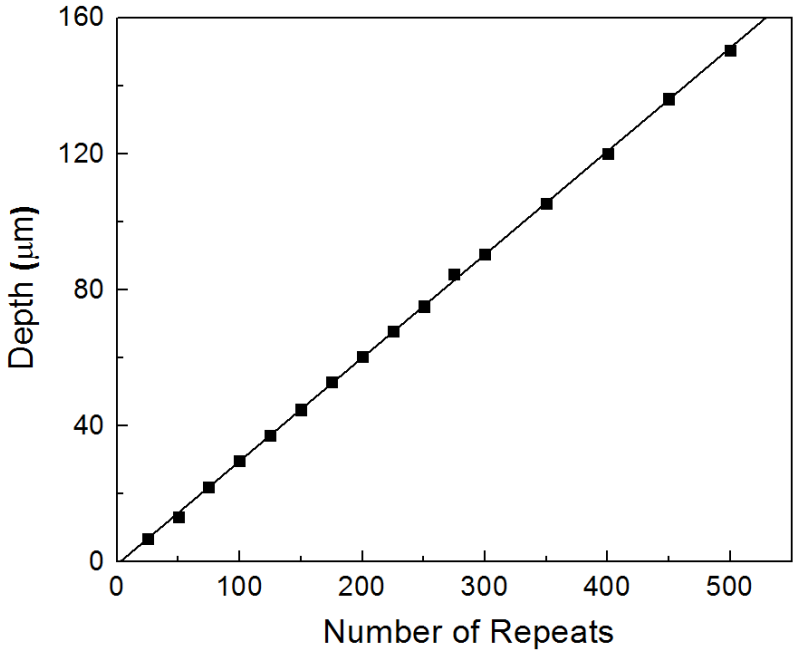

Figure 3-2 Linear relationship between number of repeats and depth

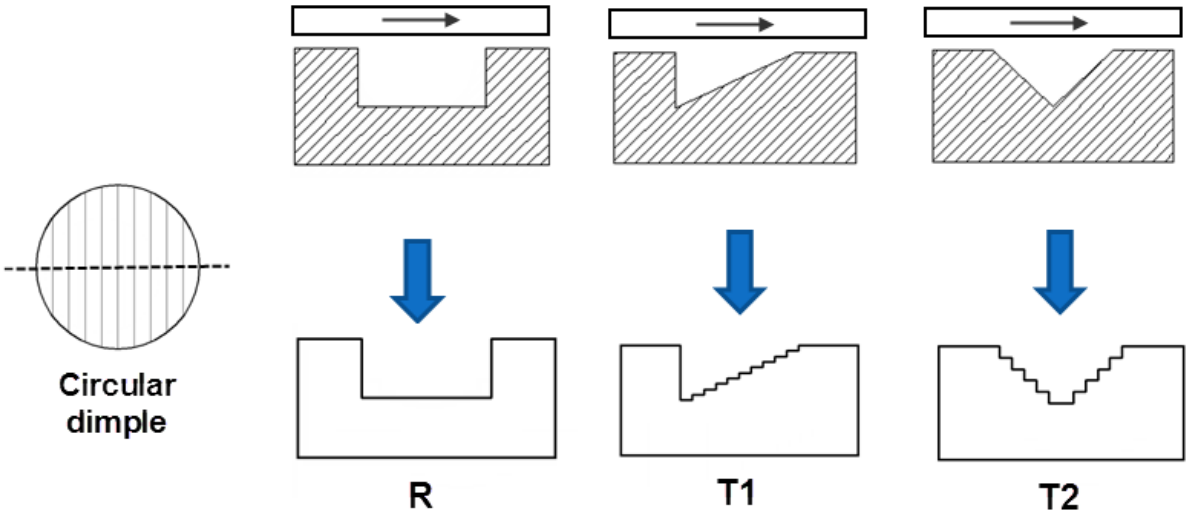

Figure 3-3 Fabrication of different dimple profiles

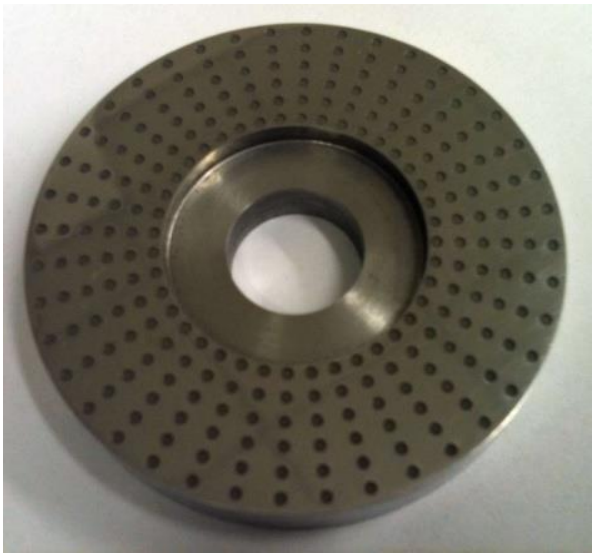

Figure 3-4 Small-dimple specimen

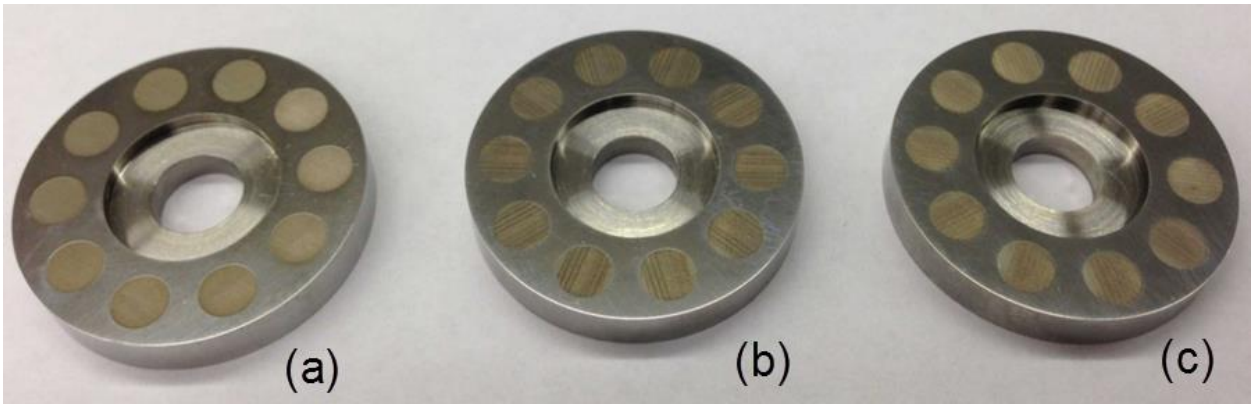

Figure 3-5 Large-dimple specimen — (a) R shape (b) T2 shape and (c) T1 shape

Two sizes of dimples were fabricated, as shown in Figures 3-4 and 3-5. For small-dimple specimens, there were 6 dimples in radial direction and 40 columns circumferentially giving a total of 240 dimples on the surface. For large-dimple specimens, 10 dimples were evenly located at the median radius of the specimen. Table 3-1 shows the geometrical parameters for the two groups of dimpled specimens. The dimples' cross-sectional shapes obtained from a stylus profiler are shown in Figures 3-6 and 3-7. Each dimple of T1 and T2 specimens is divided into five parts for small dimple and ten parts for large dimple to form a specific profile. Since this study focuses on the

effects of the internal structural shape, the geometric parameters of the dimples (see Table 3-1) are kept the same. All the dimples were fabricated on the surface of stationary lower specimen and distributed evenly in the radial direction. After laser texturing, all the specimens were polished to remove protrusions around the dimples and achieve a surface roughness (Ra) of 0.05 μm for un-textured area.

Table 3-1 Geometric parameters of specimens

No.	Dimple diameter (μm)	Maximum dimple depth (μm)	Total no. of dimples	Dimple density (%)
S_R	800	37.1	240	14.2
S_T1	800	36.8	240	14.2
S_T2	800	37.2	240	14.2
L_R	6000	26.5	10	33.2
L_T1	6000	27.6	10	33.2
L_T2	6000	28.1	10	33.2

In this study, a low dimple density was chosen for the small-dimple specimens. Experimental researches show that optimal value of dimple density varies in the range of 5 to 15 % [15]. Therefore, based on the geometry of specimen and distribution of dimples, a design with dimple density of 14.2% was used for the experiments. For large-dimple specimens, a higher dimple density was selected in order to generate higher load-carrying capacity. The choice of dimple depth depends on both dimple geometry and operating conditions. Etsion et al. [2] suggested that the

optimal depth over diameter ratio is less than 5%. Yu and Sadeghi [18] reported that an optimal depth over film thickness ratio is 3 for grooves under hydrodynamic lubrication. Based on the consideration of dimple diameter and film thickness, a maximum dimple depth around 30 μm was chosen. This value may vary slightly during the manufacturing of different dimples.

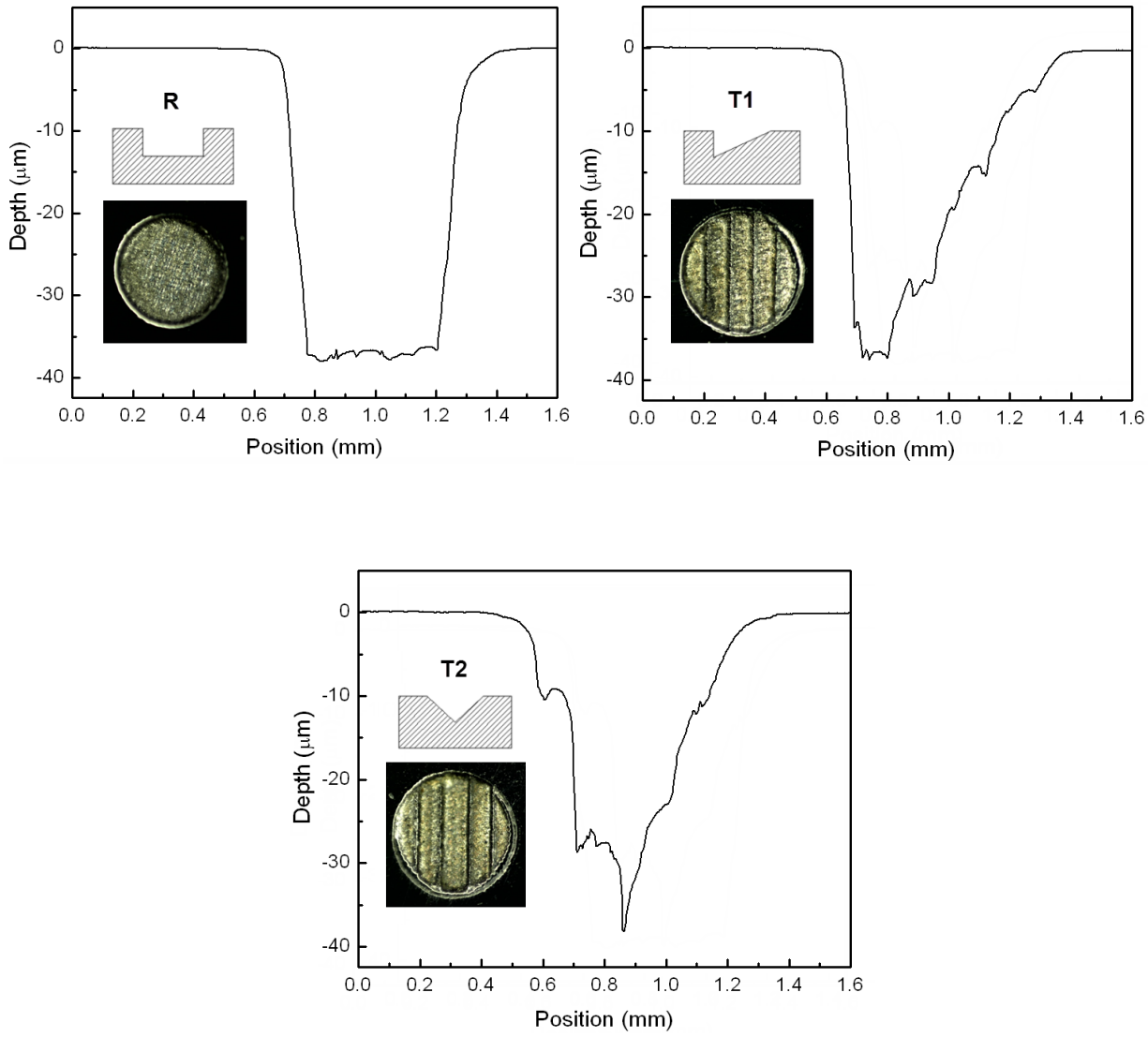

Figure 3-6 Small dimple profiles of R, T1 and T2

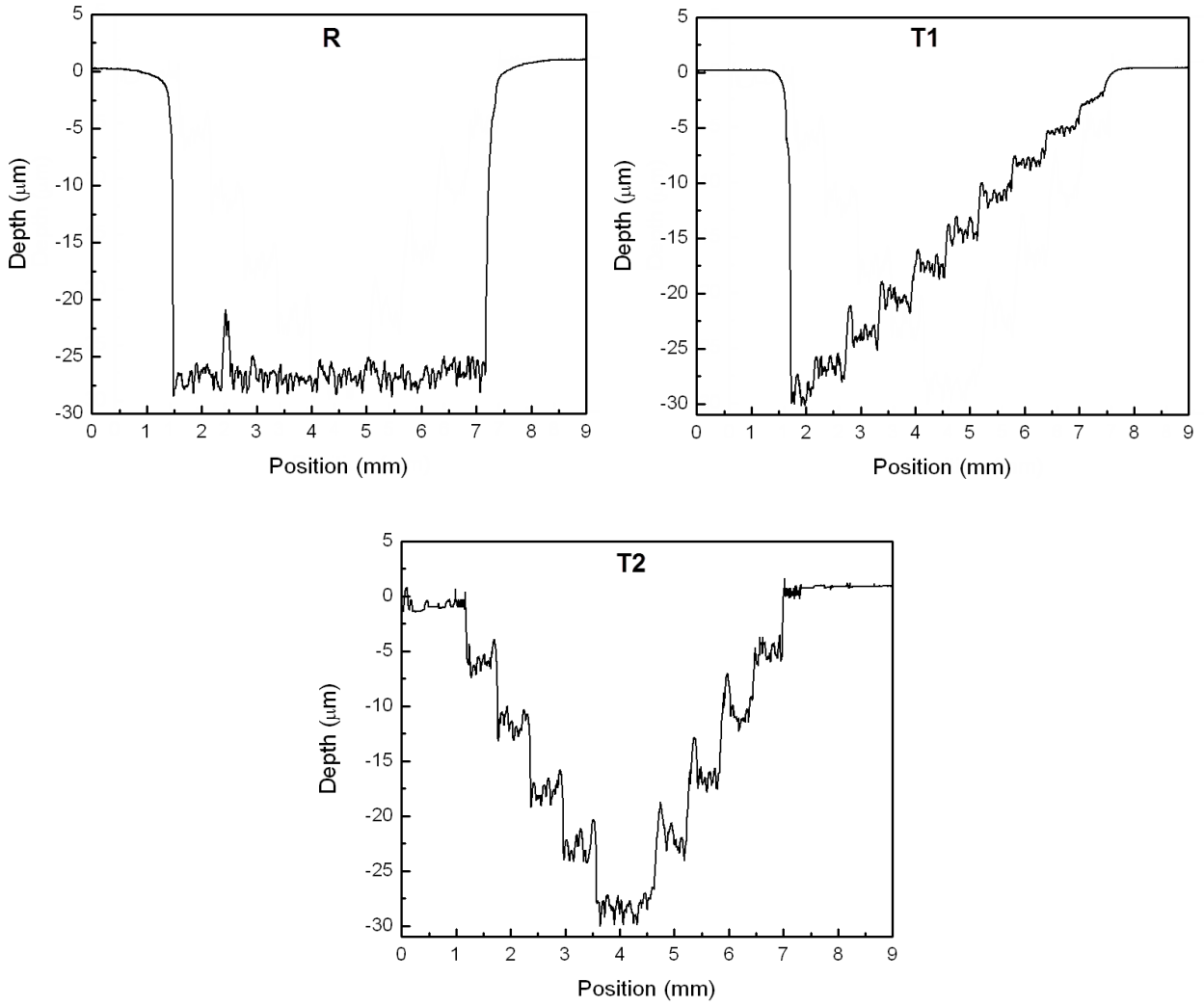

Figure 3-7 Large dimple profiles of R, T1 and T2

3.3.3 Test Procedure

To measure the load-carrying capacity, the gap between the upper disk and lower specimen was kept constant and normal force — i.e., the load-carrying capacity — generated by the fluid film between the disk and specimen was recorded. The frictional torque between the two surfaces was measured at the same time. Following the procedure outlined in reference [17], a small amount of wax was used to ensure parallelism between the specimen and the disk. Briefly, the Peltier plate's temperature was increased to the wax melting point and the specimen was placed on the wax layer.

Then, the upper disk's position was adjusted downward with the application of the load on the specimen. By decreasing the temperature of the Peltier plate, the wax was solidified and the specimen was fixed in alignment with the upper disk.

The experimental procedure involved two test sequences. For the tests involving small-dimple specimens, since the generated normal force is limited, the gap was fixed at a small value and the rotational speed is increased in a stepwise manner. In the experiments with large-dimple specimens, the rotational speed was kept constant and the gap was increased stepwise. Figure 3-8 shows the history of load-carrying capacity with the two test sequences. The bulk temperature of lubricant was maintained at 25°C throughout the experiments by using the Peltier plate. SAE 30 oil was used in the tests, which has a dynamic viscosity of 0.38 Pa·s at room temperature (25°C). The test period of each condition is 3 minutes, and the reported values correspond to stable data averaged over the last minute. Since the test time is short and there is a two-minute rest period for cooling between each test, the temperature rise of fluid film is neglected and the average lubricant film temperature is considered as 25 °C.

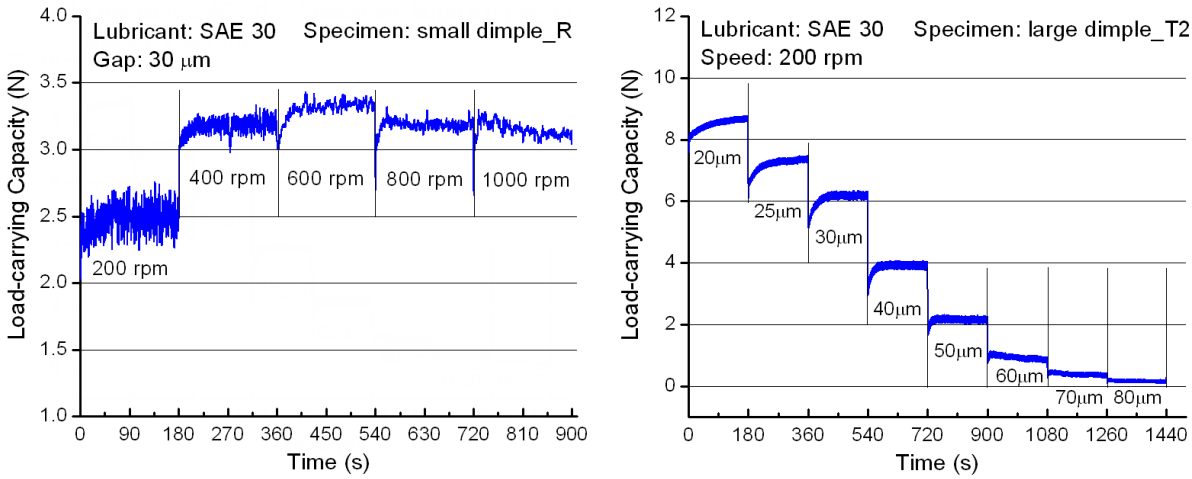

(a) (b)

Figure 3-8 Variation of load-carrying capacity during different tests (a) results with increasing speed (small dimple); (b) results with increasing gap (large dimple)

3.3.4 Results of Small-dimple Specimen

Figure 3-9 shows the load-carrying capacity test results of small-dimple specimens as a function of speed. As can be seen, under the operating conditions tested, the LCC produced by dimples with gaps of 20 μm and 30 μm are very limited, only about 3 N. For all the specimens, the LCC variation shows the same trend: it first increases to a maximum level and then drops as the rotational speed increases. This behavior can be explained by considering two competing factors. With the increasing speed, the hydrodynamic effect is increased, which helps generate LCC. On the other hand, as the speed increases the cavitation area and the effect of centrifugal force increase, which tend to reduce the LCC. These factors dominate the behavior at high speed in textured surfaces. The effects of speed on the cavitation area and centrifugal force are discussed in reference [18-20], to which interested readers can refer for further detail.

Examination of Figure 3-9 shows that for small-dimple specimens the difference between different dimple profiles is not obvious. Also, the variation in the measurement results of LCC for each specimen is relatively large. One accepted mechanism associated with LCC generation of dimples is that cavitation occurs in the divergent region of a dimple, which leads to asymmetric pressure distribution and a net force to support load. However, cavitation in small dimples can be non-uniform and unsteady, as reported in references [6, 20]. This can result in fluctuation in the dimple's LCC. Figure 3-10 shows that the frictional torque for all specimens increases monotonically as a function of speed. Comparison of the torque results reveals that under the conditions tested the dimple's internal structure has minor effect on the friction torque of specimens operating at the same film thickness. It should be noted that under current test conditions the LCC generated is small and the effect of dimple's internal structure is not appreciable. However,

this does not mean that the effect of internal structure is negligible for the small dimples. A possible reason for the small LCC is that the geometrical parameters of small dimples tested are not optimal.

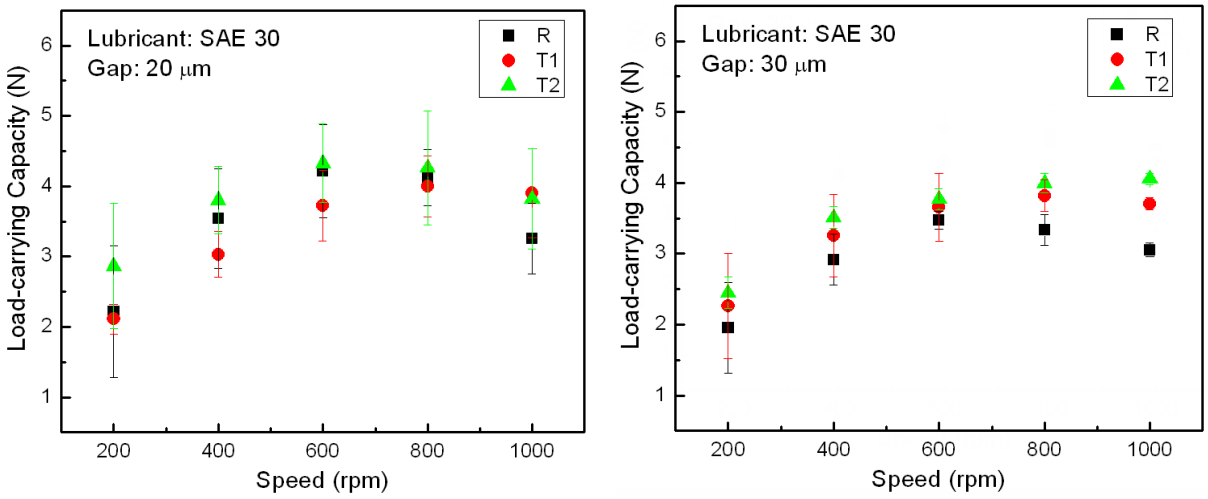

(a) (b)

Figure 3-9 Experiment results of load-carrying capacity for small-dimple specimens (a) gap of 20 μm; (b) gap of 30 μm

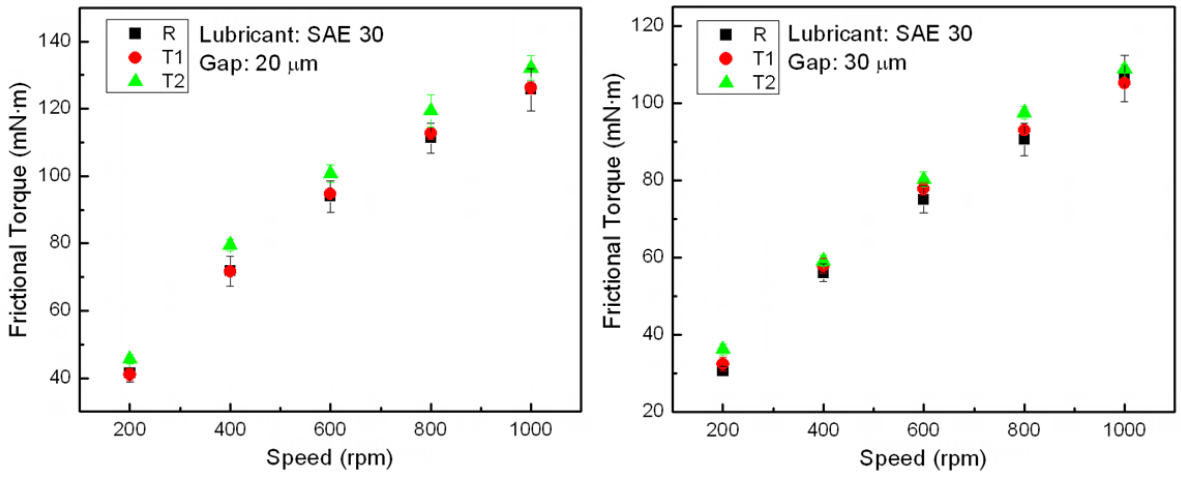

(a) (b)

Figure 3-10 Experiment results of frictional torque for small-dimple specimens (a) gap of 20 μm; (b) gap of 30 μm

3.3.5 Large-dimple Specimens

3.3.5.1 Effect of gap and rotational speed

Figure 3-11 presents the results of LCC for large-dimple specimens lubricated with SAE 30 oil. All the results in the figure show a persistent decrease in LCC with increasing gap, as expected.

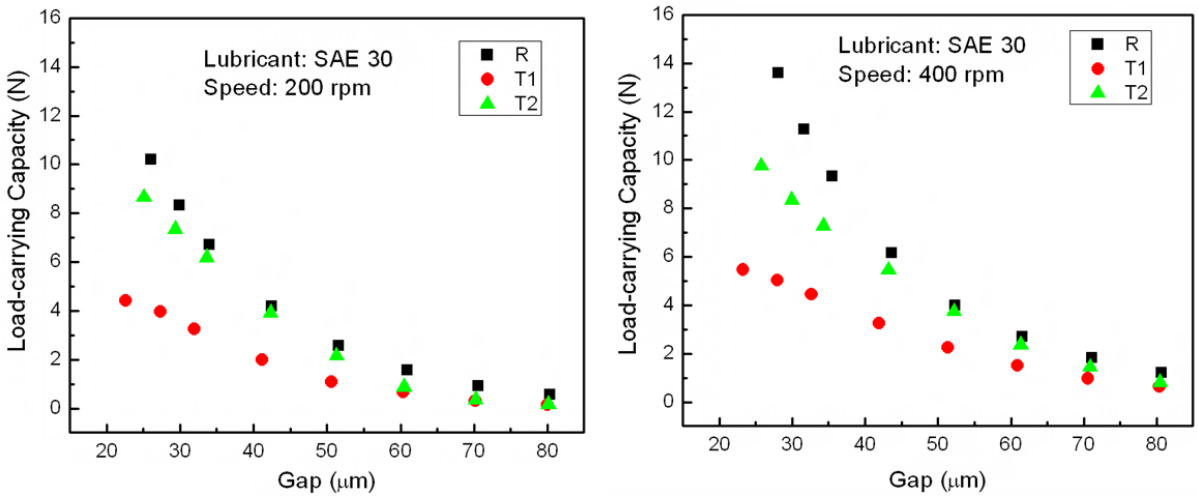

(a)

(b)

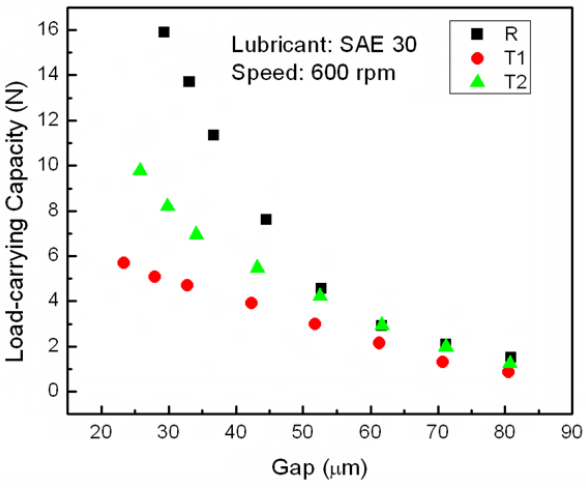

(c)

Figure 3-11 Experiment results of load-carrying capacity for large-dimple specimens under SAE 30 lubrication (a) speed of 200 rpm; (b) speed of 400 rpm; (c) speed of 600 rpm

Also, when dealing with large-dimple specimens, the results are stable and the difference between two consecutive test sequences is less than 5%. For each specimen with the same gap the LCC increases as the rotational speed is increased from 200 rpm to 600 rpm. This agrees with the hydrodynamic lubrication theory that the hydrodynamic pressure increases as the speed increases and diminishes as the film thickness increases. Comparison of the test results with specimens R, T1 and T2 show that the dimple's internal structural shape can have a significant influence on the LCC, especially at higher speed. It is shown that, under the conditions tested, the specimen R (cylindrical dimple) generates the highest LCC, while specimen T1 (dimple with profile of oblique triangle) has the lowest LCC.

3.3.5.2 Effect of Lubricant Viscosity

Figure 3-12 shows the experimental results with Chevron base oil (600R) (μ = 0.21 Pa·s at 25°C), which is less viscous than the SAE 30 (μ = 0.38 Pa·s at 25°C). Results show similar trend to those lubricated with SAE 30. The specimen R also offers the greatest LCC while specimen T1 produces the least under the tested conditions. Comparison of Figure 3-11 and Figure 3-12 demonstrates the effects of viscosity on the load carrying capacity: a lower-viscosity lubricant yields a lower LCC, as expected.

3.3.5.3 Effect of Lubricant Replenishment

In order to investigate the effects of lubricant replenishment, an upper disk with four circulation holes was constructed and used for the tests presented in this section (see Figure 3-13). The holes located close to the center of the upper disk ensure that lubricant flows into the gap and that the pressure within the inner cavity of lower specimen is maintained at the ambient pressure. Figure 3-14 presents the LCC test results using this upper disk with circulation holes. Referring to Figure

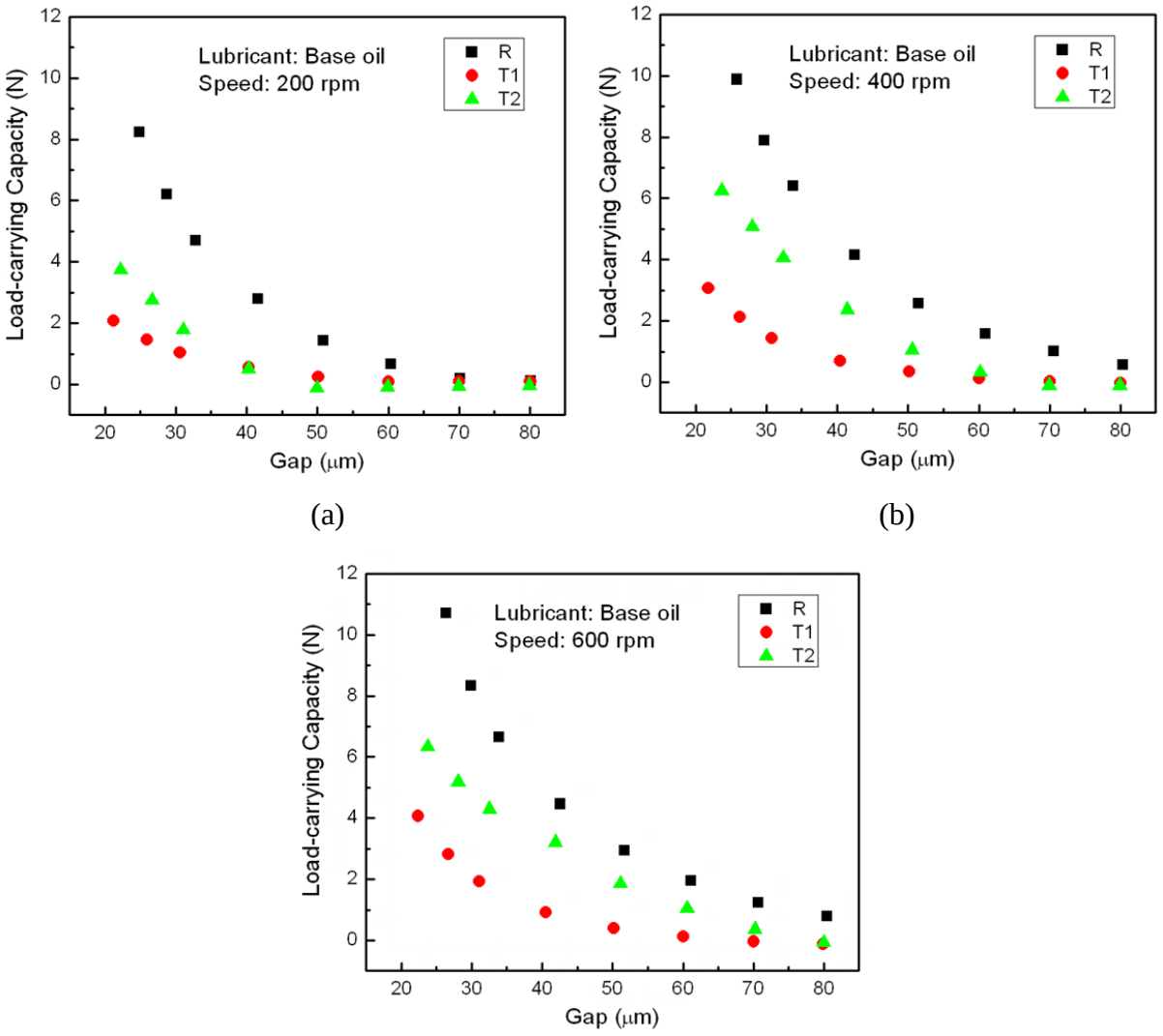

Figure 3-12 Experiment results of load-carrying capacity for large-dimple specimens with base oil (600R) lubrication (a) speed of 200 rpm; (b) speed of 400 rpm; (c) speed of 600 rpm

3-11, it can be seen that the results show similar behavior, with LCC decreasing monotonically with increasing gap. Under this test condition the specimen R still generates the maximum LCC while that from specimen T1 is minimum. Examination of Figure 3-11 and Figure 3-14 show that the circulation holes slightly reduce the LCC. This can be attributed to the effect of lubricant replenishment. As discussed in reference [21], the cavitation pressure can be affected by the replenishment of lubricant. In this experiment, the circulation holes provide more fresh oil into the

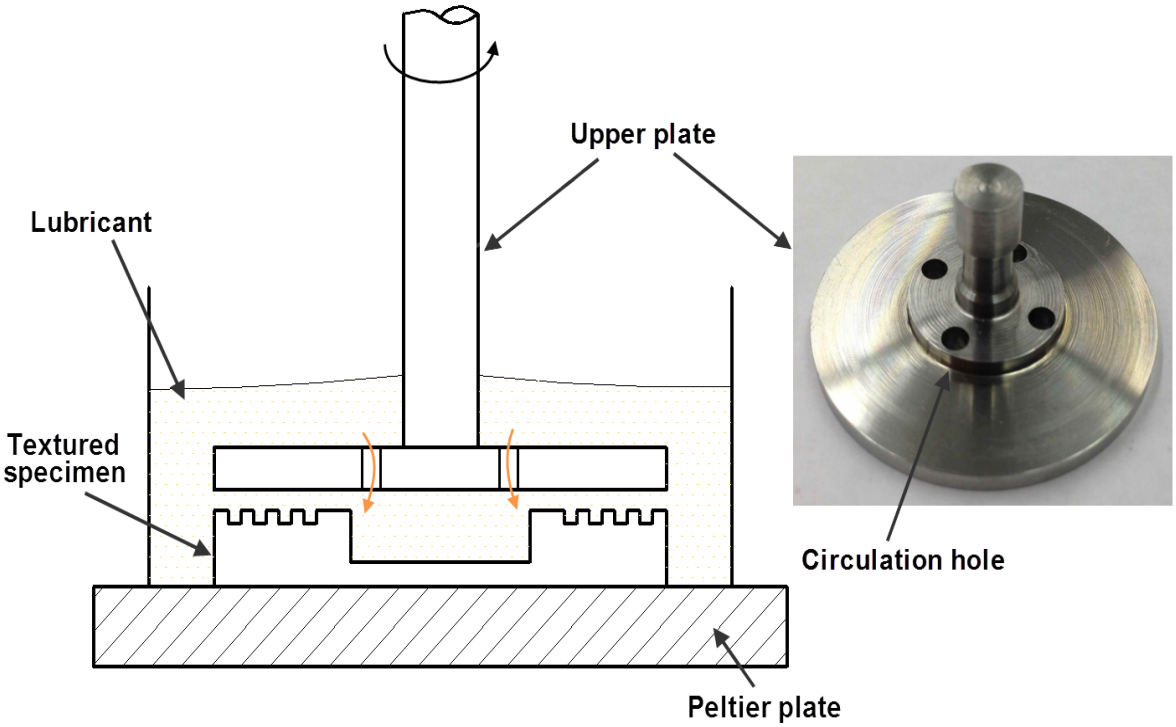

Figure 3-13 Test rig and upper disk with four circulation holes

gap that contains more air. This may result in a higher cavitation pressure with larger cavitation area, thus yielding a lower LCC within each dimple.

3.3.5.4 Results of Frictional Torque

Figure 3-15 demonstrates the effect of internal structural shape on the frictional torque subjected to a constant gap. The results indicate that the values of the frictional torque produced by the three specimens are very close. Only the results of 200 rpm are presented here; the other speeds show the same trend. The results reveal that under the conditions tested the internal structural shape of dimples has limited effect on the frictional torque. It can be observed that the gap values are not exactly the same in Figure 3-15, especially at the small-gap region (gap < 40 μm). This is due to the normal force (LCC) generated by the specimens, which works as an "opening force" and

increases the gap. Since the opening force for each specimen is different, the final gap thicknesses in the tests are slightly different. At the large-gap region, the generated normal force is small and hence the gaps for all specimens are uniform.

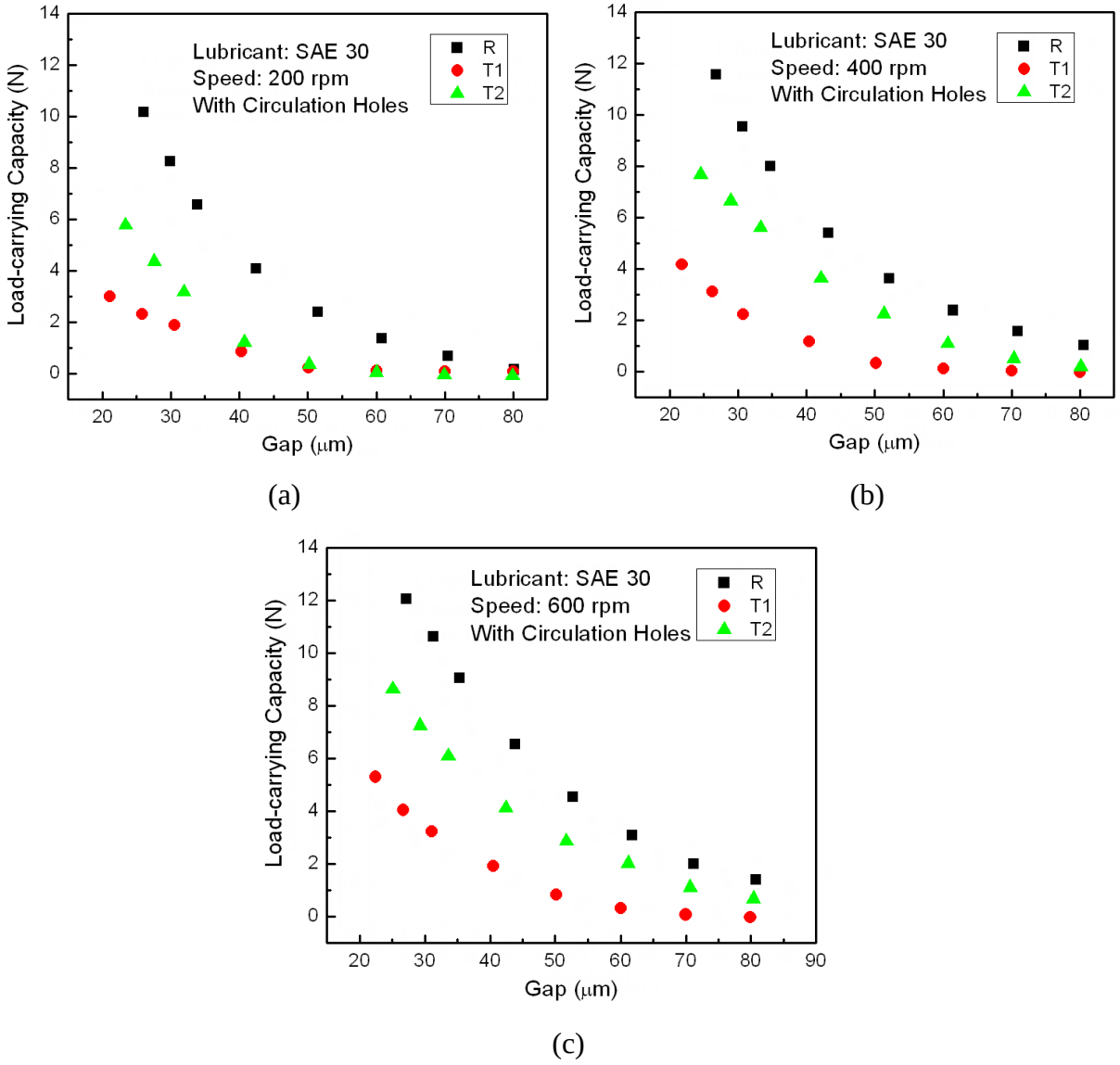

Figure 3-14 Experiment results of load-carrying capacity for large-dimple specimens with new upper disk (a) speed of 200 rpm; (b) speed of 400 rpm; (c) speed of 600 rpm

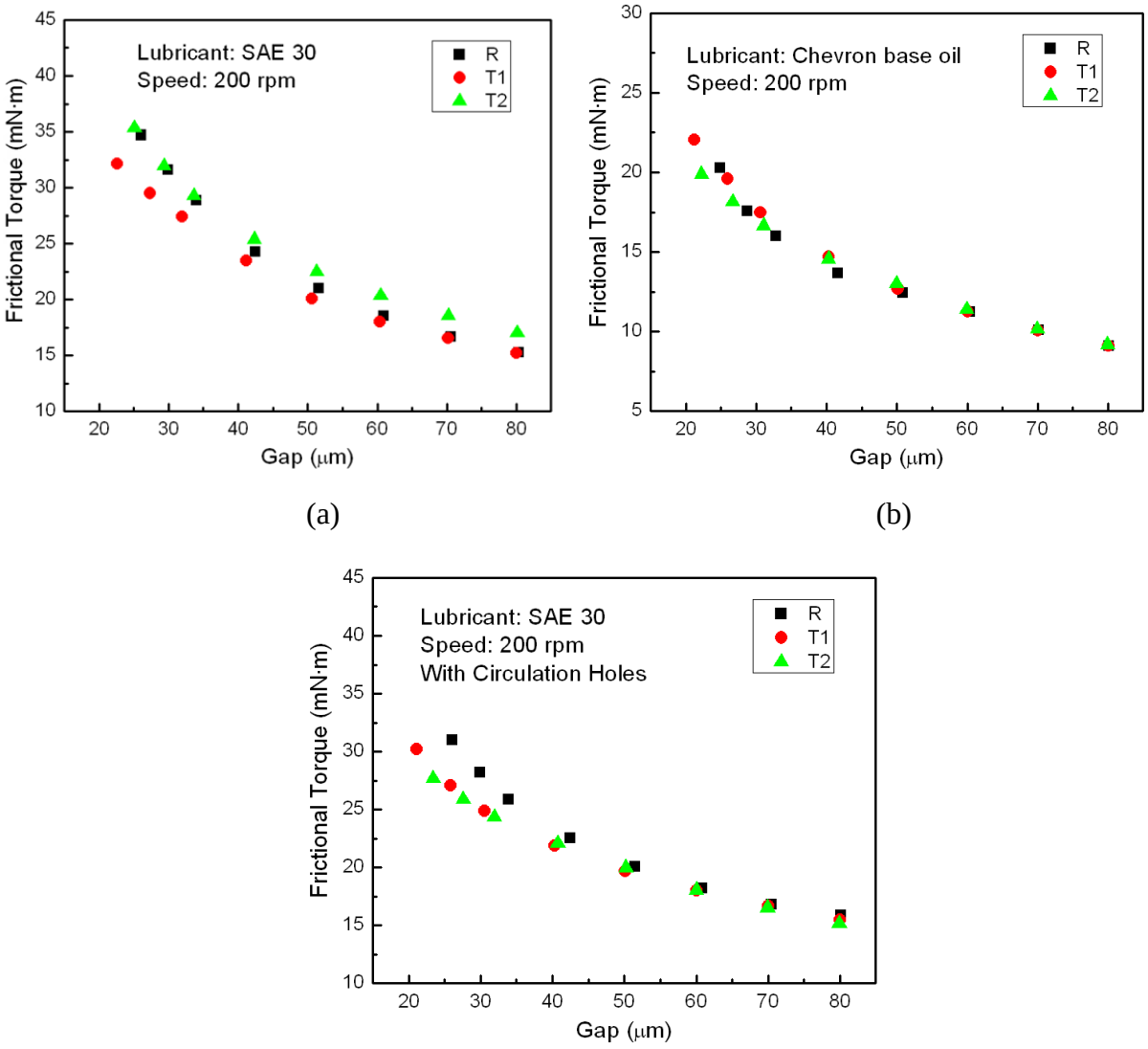

Figure 3-15 Experiment results of frictional torque for large-dimple specimens (a) SAE 30 (b) Chevron base oil (600R) (c) SAE 30 with circulation holes

3.4 Numerical Simulations

The performance of dimples with different profiles is also investigated by numerical simulations. Since one accepted LCC mechanism for surface textures is the unsymmetrical pressure distribution caused by cavitation, the numerical model must treat cavitation accurately. According to reference [6], Jakobsson-Floberg-Olsson (JFO) cavitation boundary conditions are the most realistic because

they can account for film rupture and reformation and ensure mass continuity. Hence, in this paper, a mass conservative algorithm in reference [6] was applied to implement JFO boundary conditions.

3.4.1 Governing Equations

We assume that the lubricant is Newtonian and incompressible and that the flow remains laminar and steady. To simplify the formulations, thermal and inertial effects are neglected. Under these conditions, the pressure distribution in the fluid film is governed by the Reynolds equation in cylindrical coordinates:

$$\frac{1}{r}\frac{\partial}{\partial r}\left(\rho r h^3 \frac{\partial p}{\partial r}\right)+\frac{1}{r}\frac{\partial}{\partial \theta}\left(\frac{\rho h^3}{r}\frac{\partial P}{\partial \theta}\right)=6\mu\omega\frac{\partial \rho h}{\partial \theta} \tag{1}$$

In order to deal with cavitation in the dimples, a modified Reynolds equation proposed by Elrod [22, 23] is used in this study, which is capable of describing both full-film and cavitation regions and distinguish the boundaries of cavitated zone automatically. This mass-conservative form of the Reynolds equation is

$$\frac{1}{r}\frac{\partial}{\partial r}\left(r\beta\, h^3 g\frac{\partial \varphi}{\partial r}\right)+\frac{1}{r}\frac{\partial}{\partial \theta}\left(\frac{\beta\, h^3 g}{r}\frac{\partial \varphi}{\partial \theta}\right)=6\mu\omega\frac{\partial(\varphi\, h)}{\partial \theta} \tag{2}$$

where β is the bulk modulus of the lubricant, g is the so-called switch function, and φ is the film content parameter ($\varphi = \rho/\rho_c$). The bulk modulus β satisfies the following equation:

$$\beta = \rho\frac{\partial P}{\partial \rho} \tag{3}$$

The switch function is defined as:

$$g=\begin{cases}0 & \varphi<1 \quad \text{full film region}\\ 1 & \varphi\geq 1 \quad \text{cavitation region}\end{cases}$$

It is used to distinguish the boundaries of cavitation region. To non-dimensionalize Eq. (2), the following dimensionless terms are defined:

$$\bar{r} = \frac{r}{r_i},\ \bar{h} = \frac{h}{h_0},\ \lambda = \frac{6\mu\omega}{\beta}\left(\frac{r_i}{h_0}\right)^2 \tag{4}$$

where r_i is inner radius and h_0 is minimum film thickness. Substituting Eq. (4) in Eq. (2) yields the dimensionless form of the modified Reynolds equation:

$$\frac{1}{\bar{r}}\frac{\partial}{\partial \bar{r}}\left(\bar{r}\bar{h}^3 g\frac{\partial \varphi}{\partial \bar{r}}\right)+\frac{1}{\bar{r}}\frac{\partial}{\partial \theta}\left(\frac{\bar{h}^3 g}{\bar{r}}\frac{\partial \varphi}{\partial \theta}\right)=\lambda\frac{\partial(\varphi\,\bar{h})}{\partial \theta} \tag{5}$$

By solving the governing equation for φ, the pressure distribution in the full-film region can be obtained with the following relationship:

$$p = p_c + \beta \ln \varphi \tag{6}$$

where p_c is the cavitation pressure of the lubricant. In the cavitation region, the pressure is constantly maintained at p_c. The non-dimensional pressure distribution is given by

$$\bar{p} = \frac{p}{p_a} \tag{7}$$

where p_a is ambient pressure.

3.4.2 Boundary Conditions

Since the specimen is axisymmetric, it is sufficient to analyze only one sector, as shown in Figure 3-16. Hence a model of one-dimple cell in cylindrical coordinates can be applied for analysis. The boundary conditions in the radial direction are

$$p = p_a \qquad \text{at} \quad r = r_i \text{ and } r = r_o \tag{8}$$

The cyclic boundary conditions in circumferential direction are

$$p(0, r) = p(\theta_0, r) \tag{9}$$

$$\frac{\partial p(0, r)}{\partial \theta} = \frac{\partial p(\theta_0, r)}{\partial \theta} \tag{10}$$

The corresponding boundary conditions for Eq. 5 are as follows:

$$\varphi = e^{\frac{P_a - P_c}{\beta}} \qquad \text{at } \bar{r} = 1 \text{and } \bar{r} = \frac{r_o}{r_i} \tag{11}$$

$$\varphi(0, \bar{r}) = \varphi(\theta_0, \bar{r}) \tag{12}$$

$$\frac{\partial \varphi(0, \bar{r})}{\partial \theta} = \frac{\partial \varphi(\theta_0, \bar{r})}{\partial \theta} \tag{13}$$

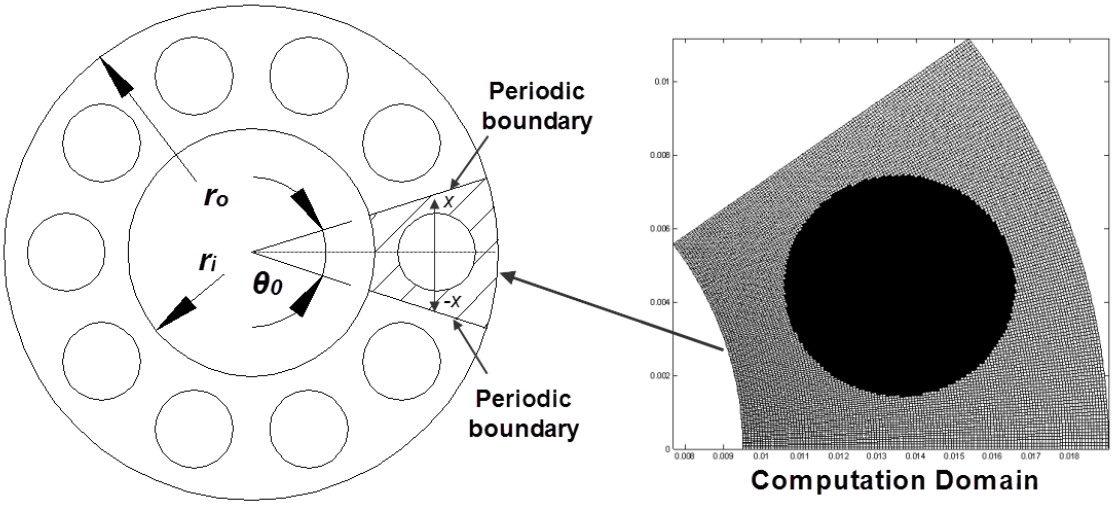

Figure 3-16 Computational domain

3.4.3 Geometric Model

The outer shapes of dimples in this study are identically circular. But the dimple's internal structural shapes are different and vary in the direction that is perpendicular to the vector from origin to the dimple center (*x* and *–x* direction in Figure 3-16). The dimensionless film thickness of dimples with different internal structure shapes can be described by mathematical equations as follows:

$$\bar{d} = \frac{\sqrt{r^2 + r_c^2 - 2rr_c\cos(\theta - \theta_c)}}{r_i} \tag{14a}$$

$$\bar{h} = 1 \qquad \text{when } \bar{d} \geq \frac{r_d}{r_i} \tag{14b}$$

$$\bar{h} = \begin{cases} 1 + \dfrac{h_d}{h_0} & \text{R} \\ 1 + \dfrac{h_d}{h_0}\left(1 - \dfrac{c_d + r_d}{2r_d}\right) & \text{T1} \\ 1 + \dfrac{h_d}{h_0}\left(1 - \left|\dfrac{c_d}{r_d}\right|\right) & \text{T2} \end{cases} \qquad \text{when } \bar{d} < \frac{r_d}{r_i} \tag{14c}$$

$$c_d = \frac{r\sin\theta - \tan\theta_c \cdot r\cos\theta}{\sqrt{\tan^2\theta_c + 1}} \tag{14d}$$

where r_d is the dimple radius, c_d is the distance to the dimple center, the r_c and θ_c are cylindrical coordinates of dimple center, and h_d and h_0 are maximum dimple depth and minimum film thickness respectively. Figure 3-17 illustrates the lubricant film profiles of different dimples generated according to the above equations.

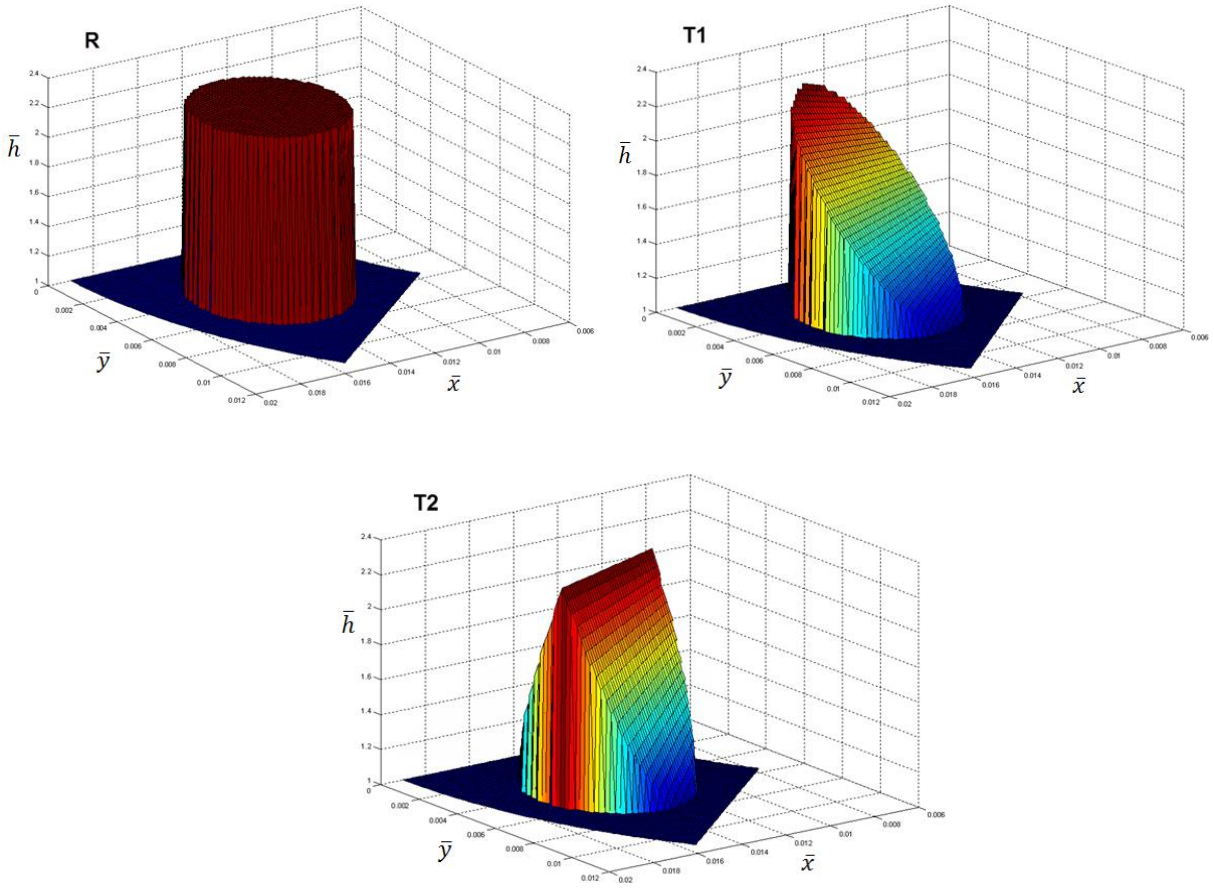

Figure 3-17 Lubricant film profiles for R, T1 and T2 dimples

3.4.4 Solution and Performance Parameters

In order to enhance the computational efficiency, an improved Elrod's algorithm proposed by Vijayaraghavan and Keith [24, 25] and a multi-grid method introduced in reference [6] was employed to solve the governing equation. Due to the multi-grid method and periodic boundary conditions, the number of mesh nodes in each direction needs to be 2N+1, where N is a positive integer. Based on the accuracy and computing time, a grid mesh of 65×65 was used for the simulations. The computation is considered to be convergent when the sum of fractional changes in the film content between two successive iterations falls below the error tolerance.

$$\sum_{i=1}^{i\max}\sum_{j=1}^{j\max}\left|\frac{\varphi_{i,j}^{new}-\varphi_{i,j}^{old}}{\varphi_{i,j}^{new}}\right|<\varepsilon \tag{15}$$

where ε is the error tolerance.

Once the convergence is reached, the pressure distribution is determined according to the results of film content parameter (φ). The non-dimensional load carrying capacity of a single dimple is obtained by integrating the pressure over the entire domain.

$$\overline{W}=\iint_{\Omega}\overline{p}\bar{r}d\bar{r}d\theta \tag{16}$$

The dimensionless frictional torque is calculated by

$$\overline{T}=\iint_{\Omega}\overline{\tau}\bar{r}^{2}d\bar{r}d\theta \tag{17}$$

where the non-dimensional shear stress is given by

$$\bar{\tau}=\bar{\omega}\frac{\bar{r}}{\bar{h}}-\frac{3p_a}{\lambda\beta}\frac{\bar{h}}{\bar{r}}\frac{\partial\bar{p}}{\partial\theta} \qquad \text{in full-film region} \tag{18a}$$

$$\bar{\tau}=\varphi\bar{\omega}\frac{\bar{r}}{\bar{h}} \qquad \text{in cavitation region} \tag{18b}$$

3.4.5 Performance Study

Table 3-2 shows the basic input parameters used in the simulations. The rotational speed ranges from 10 to 20480 rpm and the film thickness is varied from 10 to 80 μm, which represents different working conditions for the parallel thrust bearing. Figure 3-18 illustrates a typical pressure distribution of a dimpled sector and the corresponding cavitation region. It shows that the lubricant film cavitates in the diverging area while the highest pressure occurs around the rim of dimple in the converging section.

Table 3-2 The input parameters of the simulation

Parameter	Value
Inner radius r_i (mm)	9.5
Inner radius r_o (mm)	19
Dimple radius r_d (mm)	3
Maximum dimple depth h_d (μm)	25
Film thickness h_0 range (μm)	10-80
Viscosity μ (Pa.s)	0.38
Cavitation pressure p_c (Pa)	0.9×10^5, 0.3×10^5
Ambient pressure p_a (Pa)	1×10^5 Pa
Bulk modulus β (Pa)	1.62×10^9 Pa
Error tolerance ε	1×10^{-6}
Rotational speed range (rpm)	10-20480

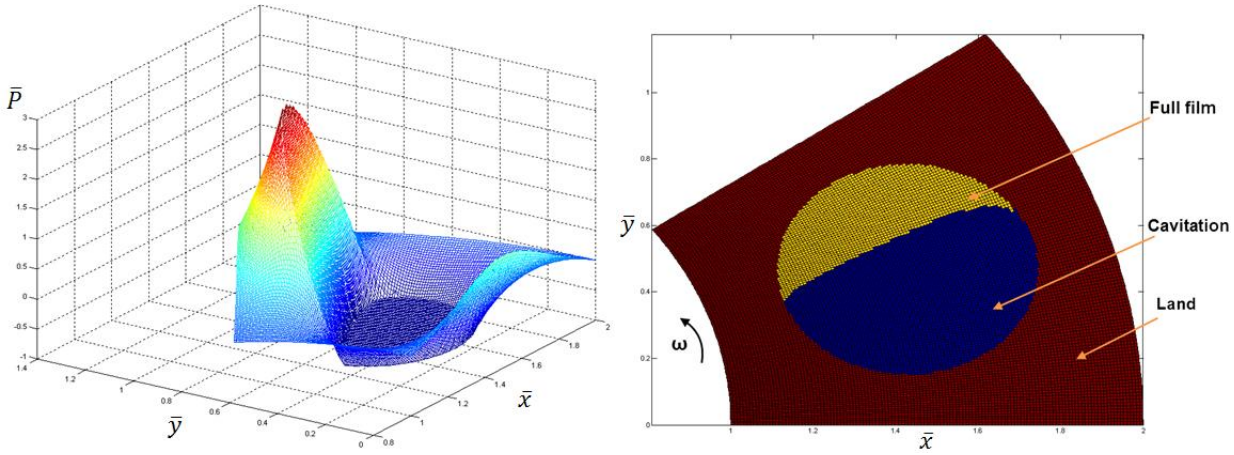

(a) (b)

Figure 3-18 Simulation results of a dimpled sector, (a) dimensionless pressure profile and (b) cavitation region (cylindrical dimple, h_0 = 30 μm, p_c = 30 kPa and speed = 400 rpm)

3.4.5.1 Comparison with Experimental Results

Before presenting the results of a parametric study on the effect of dimple internal structure, a comparison between experimental and simulation results is performed to validate the simulation methodology. The experimental results are from the LCC tests using the upper disk with circulation holes under speed of 600 rpm with SAE 30. Cavitation pressure is assumed to be 30 kPa. Simulation results are dimensionalized, and compared with measurements as shown in Figure 3-19. Good agreements can be observed between the numerical and experimental data in the small-gap region (gap < 40 μm) of each test. But as the gap increases, they exhibit similar trends but the quantitative agreement is less satisfactory. As discussed in Ref. [21], this discrepancy can be attributed to the varied cavitation pressure. These differences notwithstanding, the dimensional simulation results indicate that the numerical model is generally capable of predicting the behavior of dimples with different profiles under hydrodynamic lubrication.

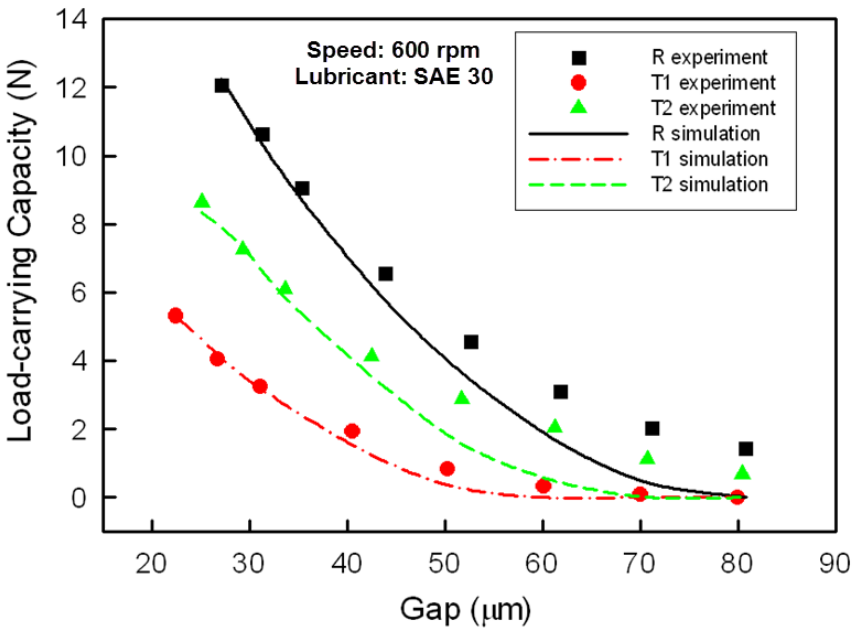

Figure 3-19 Comparison of simulation and experiment results for different dimples with holed upper disk at 600 rpm

3.4.5.2 Effect of λ

The characteristic number λ is a non-dimensional parameter defined in Eq. (5). It is proportional to the lubricant viscosity μ, angular velocity ω and the inverse of the bulk modulus β. Figure 3-20 shows the effect of increasing λ on the LCC for different dimples. The film thickness h_0 is maintained at 20 μm in the simulations. According to Ref. [21], the cavitation pressure can significantly affect the simulation results using mass conservative algorithm, and that the value of cavitation pressure under steady-state lubrication can vary from 30 kPa to 90 kPa depending on the operating conditions. Hence, two cavitation pressures were used in the simulations to consider the effects of cavitation pressure. The results are shown in Figure 3-20.

The present simulation results further confirm the significant influence of λ on the LCC. For the cavitation pressure of 90 kPa, the LCC increases to a maximum value and then gradually decreases as λ is increased. The curves for cavitation pressure of 30 kPa show the same trend, but at appreciably higher LCC. The results indicate that there exists an optimum λ that produces the maximum LCC. If the value of λ is higher than the optimum value, the LCC begins to drop. For a given geometry and lubricant, an increase of rotational speed corresponds to an increase in λ. Consequently, the simulation results suggest that the LCC will drop with an increasing rotational speed beyond a certain value. This phenomenon can also be observed in Figure 3-9, which shows the test results with increasing speed.

Figure 3-20 also shows the difference in the LCC for dimples with different internal structural shapes. The results shows that cylindrical dimples generate significantly more LCC than dimples with triangular cross-sectional shapes. This agrees with the experimental results.

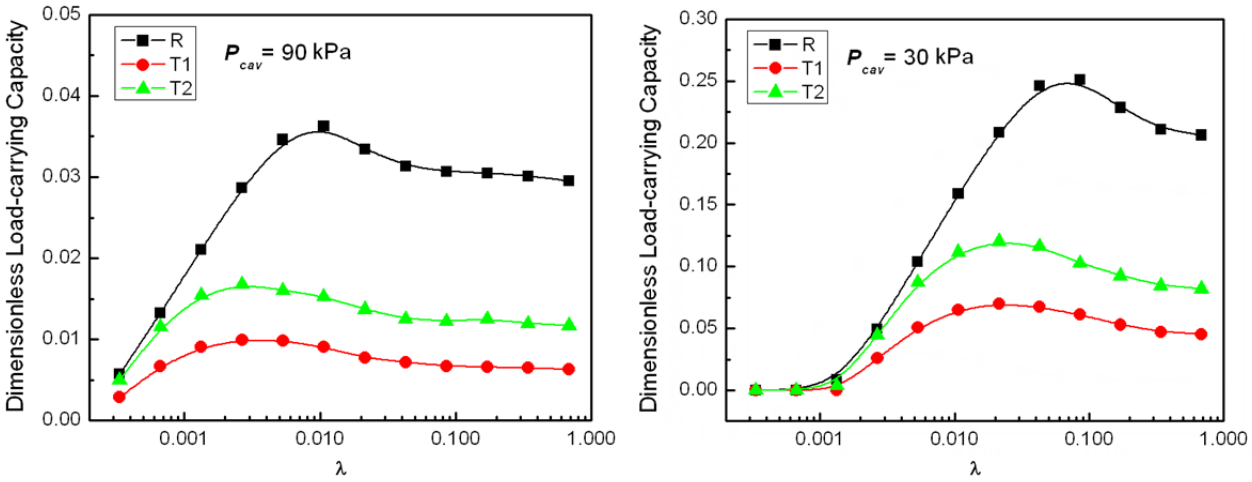

Figure 3-20 Effect of λ on the load-carrying capacity for different dimple profiles

The effect of cavitation pressure on the LCC can be seen by comparing the curves of different cavitation pressures. For the results under cavitation pressure of 30 kPa, there exists a critical value of λ below which the dimples cannot produce any LCC. Under the conditions simulated, this value is around 0.001. When λ is large (higher than the critical value), the LCC generated under cavitation pressure of 30 kPa is much larger than that under 90 kPa. Also, the optimum value of λ shifts to a larger number as the cavitation pressure is reduced from 90 kPa to 30 kPa. Regardless of the cavitation pressure, however, the cylindrical dimple produces the highest LCC.

Figure 3-21 shows the simulation results of the frictional torque with the same input parameters. It demonstrates that the frictional torque increases monotonically with increasing λ. The dimple internal structure and cavitation pressure have little influence on the frictional torque. This agrees with the experiemtal results of frictional torque since the results of specimen R,T1 and T2 are very close.

These results suggest that even though the dimple internal structure can influence the LCC singnificanly its effect on the frictional torque is minor. The reason is thought to be the dominant influence of Couette term on the shear stress (first term in Eq. 18). When the pressure gradient

term is neligible and speed is constant, the shear stress only depends on the local film thickness. Since the average local film thicknesses of different specimens are close, the difference between the magnitudes of the frictional torque is not significant. It should be noted that both experiments and simulations were conducted with a constant film thickness in this case. However, in a typical application, the load is usually maintained, so that the film thickness will vary depending on the lubrication effectiveness of dimple geometry. As a result, different dimple profiles can affect the frictional torques.

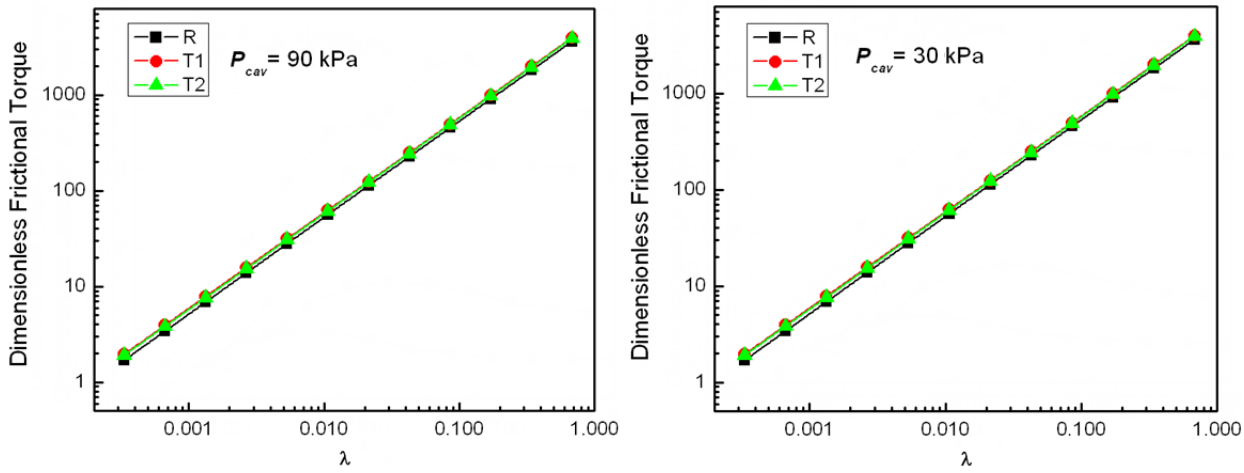

Figure 3-21 Effect of λ on the frictional torque for different dimple profiles

3.4.5.3 Effect of Film Thickness

Figure 3-22 presents a parametric study on the effects of film thickness. In the simulations, the film thickness is varied from 10 to 80 μm, while the rotational speed is kept at 600 rpm. Prediction results are shown for cavitation pressures of 90 kPa and 30 kPa. It demonstrates that the LCC decreases as the film thickness increases. Its value approaches zero when the film thickness is greater than a certain value. Comparison of results with different dimple profiles shows that the LCC of cylindrical dimple is maximum while that of the T1 dimple is the least. These results show the similar trends with the test results, as shown in Figures 3-11, 3-12 and 3-14. For the results

with cavitation pressure of 30 kPa, beyond a certain gap the LCC becomes nil. When film thickness is small (less than 50 μm), the LCC generated with cavitation pressure of 30 kPa is consistantly greater than that with 90 kPa.

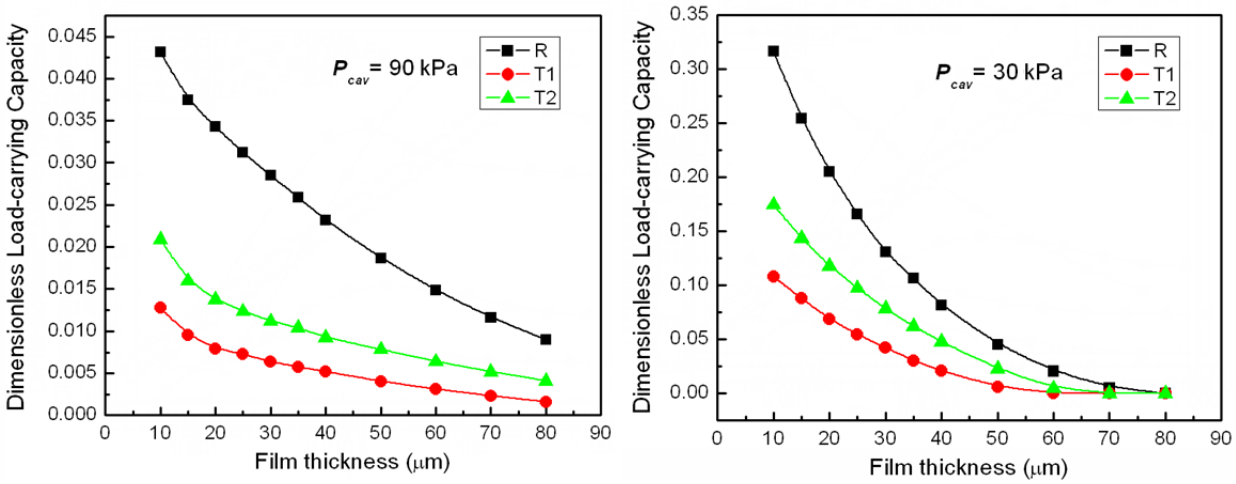

Figure 3-22 Effect of film thickness on the load-carrying capacity for different dimple profiles

3.4.5.4 Comparison of Pressure Distributions

Experimental and simulation results show that the dimple internal structure has a significant influence on the LCC. With the geometrical parameters used in this study, the cylindrical dimple always produces more LCC than dimples with triangular profiles under different operating conditions. To explain the influence of dimple's internal structural shape on hydrodynamic lubrication, the pressure distributions of different dimples are compared in Figure 3-23. In the simulation, the film thickness is 30 μm and rotational speed is maintained at 600 rpm. The results pertain to the pressure profiles along the centerline ($\bar{r}$ =1.5) of the sector for dimple R, T1 and T2. As can be seen in the figure of 90 kPa, the cylindrical dimple gives the highest peak pressure and overall pressure, while the pressure results and cavitation region of dimple T1 is the smallest. The simulation results with cavitation pressure of 30 kPa show the same trend. These results indicate that the converging wedge shape in the dimple T1 and T2 can reduce the cavitation region but is

not optimal for pressure build-up. The converging step shape in the profile of cylindrical dimple is more efficient for generating positive pressure than the wedge shape. As a result, even though the cavitation area of cylindrical dimple is slightly larger, its average pressure and hence LCC is the higher. In addition, as the internal structure of dimple changes the average dimple depth and dimple volume varies, which may also contribute to the difference of LCC. Further research can be carried out to investigate the effect of dimple's internal structural shape when the average dimple depth or dimple volume is uniform.

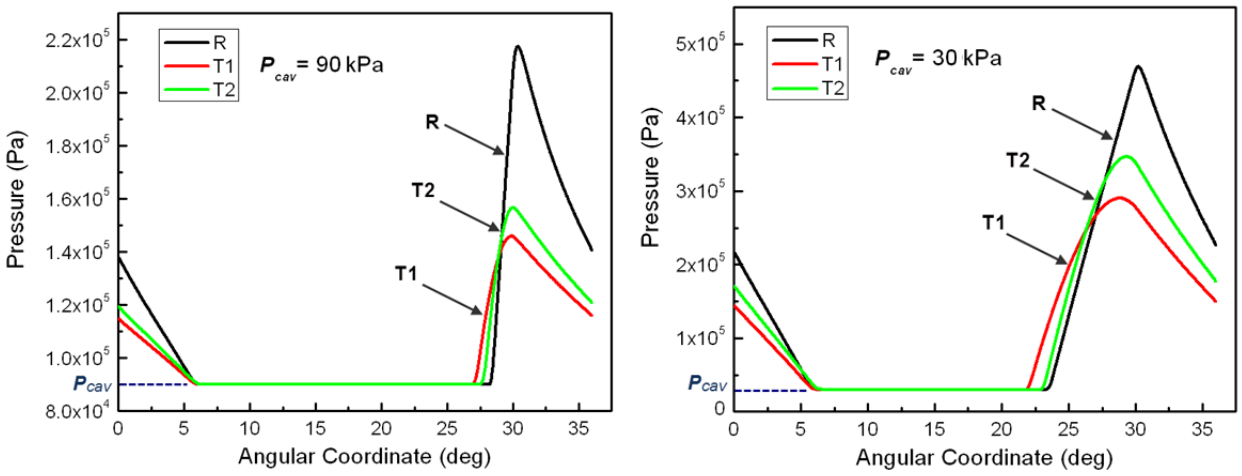

Figure 3-23 Pressure distributions for different dimple profiles

3.5 Conclusions

In this research, the effect of dimple internal structural shape on hydrodynamic lubrication was investigated both experimentally and numerically. An approach to fabricate dimples with different profiles was developed using a laser marking machine. Three dimples internal structural shapes were made for comparison: rectangle (R), oblique triangle (T1) and isosceles triangle (T2). Two sizes of dimples were fabricated on the thrust bearing-like specimens. The LCC was measured under fully-flooded lubrication with a torsional rheometer equipped with tribology accessories. The results of small-dimple specimens show that the LCC produced by small dimples is limited.

The effect of dimple profile on the LCC is not obvious for small-dimple specimens under current test conditions. However, the LCC of large-dimple specimens is stable and repeatable. Their experimental results show that the dimple internal structure has a profound influence on the LCC but its effect on frictional torque was not appreciable. A comparison of dimples' performances reveals that the cylindrical dimple is the best for LCC with geometrical dimensions used in this research.

The Reynolds equation with a mass conservative algorithm was treated numerically to predict the performances of dimples under different operating conditions. The simulation results show that there exists an optimum λ that produces the maximum LCC of dimples. When λ is higher than the optimum value, the LCC begins to drop as λ increases. The cylindrical dimple always generates more LCC than dimples with triangular profiles under different working conditions. A possible reason is that the step shape in the profile of cylindrical dimple is more efficient for building up pressure than the wedge shape.

3.6 References

[1] Etsion, I., and Burstein, L., 1996, "A model for mechanical seals with regular micro surface structure," Tribol. Trans., 39, pp. 677–683.

[2] Etsion, I., and Kligerman, Y., 1999, "Analytical and experimental investigation of laser-textured mechanical seal faces," Tribol. Trans., 42(3), pp. 511–516.

[3] Etsion I, Halperin G, Brizmer V, Kligerman Y., 2004, "Experimental investigation of laser surface textured parallel thrust bearings," Tribol. Lett., 17(2), pp. 295–300.

[4] Wang X., Kato K., Adachi K., Aizawa K., 2003, " Loads carrying capacity map for the surface texture design of SiC thrust bearing sliding in water," Tribol. Int., 36, pp. 189–97.

[5] Wang X., Adachi K., Otsuka K., Kato K., 2006, "Optimization of the surface texture for silicon carbide sliding in water," Appl. Surf. Sci., 253(3), pp. 1282–6.

[6] Qiu, Y. and Khonsari, M. M., 2009, "On the prediction of cavitation in dimples using a mass-conservative algorithm," ASME J. Tribol., 131, pp. 041702:1-11.

[7] Qiu, Y., and Khonsari M.M., 2011, "Performance analysis of full-film textured surfaces with consideration of roughness effects", ASME J. Tribol., 133, pp. 021704:1-10.

[8] Qiu, Y., and Khonsari M.M., 2011, "Experimental investigation of tribological performance of laser textured stainless steel rings", Tribol. Int., Vol. 44, pp. 635-644.

[9] Nanbu, T., Ren, N., Yasuda, Y., Zhu, D., Wang, Q.J., 2008, "Microtextures in concentrated conformal-contact lubrication: Effects of texture bottom shape and surface relative motion," Tribol. Lett., 29, pp. 241–252

[10] Galda L., Pawlus P., Sep J., 2009, "Dimples shape and distribution effect on characteristics of Stribeck curve", Tribol. Int., 42, pp.1505–1512.

[11] Yu, H., Wang, X., Zhou, F., 2010, "Geometric shape effects of surface texture on the generation of hydrodynamic pressure between conformal contacting surfaces", Tribol. Lett., 37, pp.123-130.

[12] Yuan, S., Huang, W., Wang, X., 2011, "Orientation effects of micro-grooves on sliding surfaces", Tribol. Int., 44, pp. 1047–1054.

[13] Zhu, D., Nanbu, N., Ren, N., Yasuda, Y., Wang, Q., 2010, "Model-based virtual surface texturing for concentrated conformal-contact lubrication", Proc. Inst. Mech. Eng. Part J: J. Eng. Tribol., 224, pp. 685–696.

[14] Dobrica, M.B., Fillon, M., Pascovici, M.D., Cicone,T., 2010, "Optimizing surface texture for hydrodynamic lubricated contacts using a mass-conserving numerical approach", Proc. Inst. Mech. Eng. Part J: J. Eng. Tribol., 224, pp. 737–750.

[15] Wang X., Yu H., Huang W., 2010, "Surface texture design for different circumstances", Proceedings of the 1st international Brazilian conference on tribology, Rio de Janeiro, Brazil, pp. 97–107.

[16] Huang, W., Jiang, L., Zhou, C., Wang, X., 2012, "The lubricant retaining effect of micro-dimples on the sliding surface of PDMS", Tribol. Int., 52, pp. 87-93.

[17] Kavehpour, H., and Mckinley G., 2004, "Tribo-rheometry: from gap-dependent rheology to tribology", Tribol. Lett, 17, pp.327-335.

[18] Yu, T.H., and Sadeghi, F., 2001, "Groove effects on thrust washer lubrication," ASME J. Tribol., 123, pp. 295-304.

[19] Cross, A. T., Sadeghi, F., Cao, L. J., Rateick, R. G. and Rowan, S., 2012, "Flow visualization in a pocketed thrust washer", Tribol. Trans., 55, pp. 571-581.

[20] Zhang, J. Y. and Meng, Y. G., 2012, "Direct observation of cavitation phenomenon and hydrodynamic lubrication analysis of textured surfaces," Tribol. Lett., 46, pp.147-158.

[21] Shen, C. and Khonsari, M. M., 2013, "On the magnitude of cavitation pressure of steady-state lubrication," Tribol. Lett., 51, pp.153-160.

[22] Elrod, H. G. and Adams, M., 1974, "A computer program for cavitation," 1st Leeds-Lyon Symposium on Cavitation and Related Phenomena in Lubrication, I.M.E., Mechanical Engineering Publication, New York, 103, pp. 37-41.

[23] Elrod, H. G., 1981, "A cavitation algorithm," ASME J. Lubr. Technol., 103(3), pp. 350-354.

[24] Vijayaraghavan, D. and Keith, T. G., 1990a, "An efficient, robust and time accurate numerical procedure applied to a cavitation algorithm," ASME J. Tribol., 112, pp.44-51.

[25] Vijayaraghavan, D. and Keith, T. G., 1990b, "Grid transformation and adaption techniques applied to the analysis of cavitated journal bearings," ASME J. Tribol., 112, pp.52-59

CHAPTER 4 NUMERICAL OPTIMIZATION OF TEXTURE SHAPE FOR PARALLEL SURFACES UNDER UNIDIRECTIONAL AND BIDIRECTIONAL SLIDING [3]

4.1 Nomenclature

g Switch Function

h Local film thickness (m)

h_0 Minimum film thickness (m)

h_g Texture depth (m)

$\bar{h}$ Dimensionless local film thickness, h/h_0

L Unit cell length (m)

p Local Pressure (Pa)

p_0 Ambient pressure (Pa)

p_c Cavitation Pressure (Pa)

$\bar{p}$ Dimensionless pressure, p/p_0

U Sliding speed (m/s)

$\overline{W}$ Dimensionless load-carrying capacity

β Bulk modulus of the lubricant (Pa)

φ Film content parameter

[3] This chapter previously appeared as Shen C., Khonsari M. M., "Texture shape optimization for parallel surfaces under unidirectional and bidirectional sliding", Tribology International, 82 (2015), pp. 1-11. It is reprinted by permission of Elsevier.

μ Lubricant viscosity (Pa.s)

λ Characteristic number, $6\mu LU/\beta h_0^2$

ρ Local fluid density (kg/m^3)

4.2 Introduction

The study of enhancement of tribological performance via surface texturing has received an explosion of interest in recent years. The benefits of applying surface texturing include: increasing load-carrying capacity [1], reducing friction force and wear [2-3], expanding the range of hydrodynamic lubrication [4], and improving seizure resistance [5]. In order to maximize the effect of surface texturing, many theoretical and experimental studies have been carried out to optimize the geometrical parameters of textures by varying dimple size, depth and area density [6-15]. One of the often cited literatures on the subject is the work of Etsion et al. [6] who investigated the effects of geometric parameters on the performance of spherical shape dimples. They found that the ratio of the dimple's depth over the diameter is the most important design parameter and that there exists an optimum value of this parameter which maximize the average pressure. Wang et al. [1] experimentally investigated the performance of dimpled SiC thrust bearings under water lubrication and reported the optimum values of diameter, depth and area ratio of the dimples that maximize the load-carrying capacity (LCC). These studies mainly focus on the performance of circular dimples.

Since the dimple's shape, itself, is another important factor for the design of surface textures, a few studies have compared the tribological performances of different texture shapes and investigated the shape and orientation effect both experimentally and numerically. Wang and Hsu [16] investigated the effects of texture shape and orientation on the frictional behavior using a pin-

on-disk tribometer. They compared textures with three shapes (circular, elliptical and triangular) and two orientations (parallel and perpendicular to the sliding direction). Their test results showed that texture shape and orientation have an influence on the friction and that the elliptical dimples with major axis placed perpendicular to the sliding direction exhibited the highest friction reduction. Later, Yu et al. [10] developed a numerical model on a single dimple to computationally simulate the results of their experiments. They compared the average pressures of different textures and reported that the elliptical dimple with major axis perpendicular to the sliding direction generates the highest average pressure, which agrees with the previous experimental results.

Lu and Khonsari [17] compared the effects of circular and elliptical dimples on the Stribeck curve of journal bearing. They found that the bushing with elliptical dimples has a lower friction coefficient under mixed lubrication. Galda et al. [9] studied the dimple shape and distribution effect on the characteristics of Stribeck curve with a block-on-ring test rig. Ring specimens with dimples of spherical, long-drop and short-drop shapes were tested. Their results demonstrated that dimples of spherical and long-drop shapes perform better than the short-drop shape in terms of friction coefficient. In a recent paper, Qiu et al. [18] optimized the geometries and densities of six different texture shapes in terms of LCC under air lubrication. Then, the performance of each dimple shape with optimal geometry was compared. They concluded that ellipsoidal dimple provides the maximum LCC.

The abovementioned works show that, indeed, the tribological performance of textured surfaces is sensitive to the shape of the texture. And some dimple shapes, like ellipse or long-drop shape, perform better than others in terms of lowering the friction coefficient or increasing the LCC. However, most of these studies have concentrated on ordinary geometric shapes, and the global-optimum texture shapes for parallel flat surfaces are still unclear.

The aim of the present study is to identify optimal texture shapes for parallel flat surfaces with a mathematical optimization method. The sequential quadratic programming (SQP) method is used as the optimization algorithm in this work due to its superior performance. Starting from an arbitrary texture shape, the optimum texture geometries for both unidirectional and bidirectional sliding are obtained by an optimization process which changes design variables of texture shape to maximize the LCC. Furthermore, the performances of optimum texture shapes are compared with those of ordinary shapes under different operating conditions.

4.3 Problem Formulation

4.3.1 Computational Domain and Design Variables

Figure 4-1(a) shows the distribution of patterns on a typical textured surface. The micro-dimples are uniformly distributed on the surface with a constant depth h_g. For theoretical study, usually, a square unit cell containing one texture pattern is considered as the computational domain and periodic boundary conditions is applied in the sliding direction (X) to account for the interaction between textures. Assuming that the interactions in the other direction (Y) are negligible, the boundaries in this direction are kept at ambient pressure. The textured surface is stationary and the runner surface moves with a velocity U along the X-axis. The objective is to maximize the LCC of textured surface by determining the optimum texture shape within a unit cell.

As shown in Figure 4-1(b), a series of horizontal lines evenly divide an arbitrary texture geometry in the Y direction. With the lengths and center locations of these lines known, the texture shape can be formed by connecting the adjacent horizontal lines. Therefore, the design variables for the texture shape are simply the lengths (L_1, L_2, ..., Ln) and corresponding center locations (X_1, X_2, ..., Xn) of the horizontal lines. The texture depth (h_g) is assumed to be constant and its value is also optimized as a design variable.

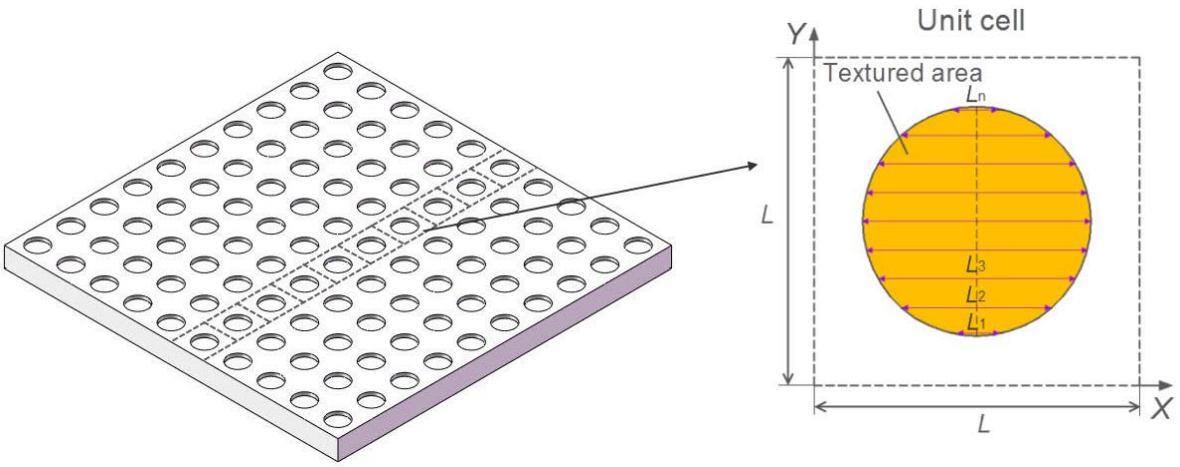

(a)

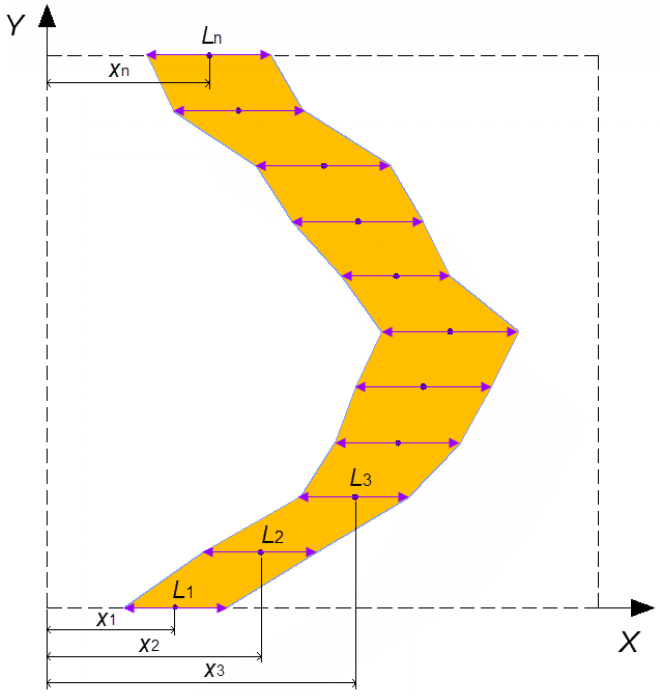

(b)

Figure 4-1 Geometrical model for texture shape optimization: (a) a typical unit cell; (b) design variables for an arbitrary texture shape

In this study, the unit cell is divided to six sections, which results in 15 design variables. The LCC of an arbitrary texture shape can be calculated by solving the Reynolds equation to determine the hydrodynamic pressure and integrating the result to obtain the total load. Then the optimization algorithm adjusts the values of these design variables to find the texture shape with maximum

LCC. This method is similar to the one used in Ref. [19], which optimized the groove shapes for flat thrust bearings.

4.3.2 Governing Equation and Objective Function

The Reynolds equation is employed to analyze the pressure distribution $p(x, y)$ within the unit cell. Assuming the lubricant is Newtonian and incompressible, the steady-state Reynolds equation [20] can be expressed as

$$\frac{\partial}{\partial x}\left(h^3 \frac{\partial p}{\partial x}\right)+\frac{\partial}{\partial y}\left(h^3 \frac{\partial p}{\partial y}\right)=6\mu U \frac{\partial h}{\partial x} \tag{1}$$

where h is the local film thickness and μ is fluid viscosity.

To non-dimensionalize Eq. (1), the following dimensionless terms are defined:

$$\bar{x}=\frac{x}{L},\ \bar{y}=\frac{y}{L},\ \bar{h}=\frac{h}{h_0},\ \bar{p}=\frac{p}{p_0},\ \Lambda=\frac{6\mu UL}{p_0 h_0^2} \tag{2}$$

where L is the length of the square cell, h_0 is the minimum film thickness and p_0 is the ambient pressure. Substituting Eq. (2) in Eq. (1) yields the dimensionless form of the Reynolds equation:

$$\frac{\partial}{\partial \bar{x}}\left(\bar{h}^3 \frac{\partial \bar{p}}{\partial \bar{x}}\right)+\frac{\partial}{\partial \bar{y}}\left(\bar{h}^3 \frac{\partial \bar{p}}{\partial \bar{y}}\right)=\Lambda \frac{\partial \bar{h}}{\partial \bar{x}} \tag{3}$$

The finite difference formulation was applied to discretize Eq. (3), which leads to a set of linear algebraic equations. These equations were then solved by a fast direct solver based on LU decomposition [21]. Once Eq. (3) is solved based on the given film profile and boundary conditions, the pressure distribution is determined. The negative pressure in the solution is set to zero to account for cavitation, which is equivalent to the half-Sommerfeld boundary condition.

The non-dimensional LCC is used as the objective function in the optimization, and its value can be obtained by integrating the dimensionless pressure over the entire domain:

$$\overline{W} = \int_0^1 \int_0^1 \bar{p} d\bar{x} d\bar{y} \tag{4}$$

The optimization problem can now be stated in dimensionless form as follows: Find $\overline{X}_1$, $\overline{L}_1$,..., $\overline{X}_n$, $\overline{L}_n$, $\overline{h}_g$ that maximize the objective function $\overline{W}$ subject to the constraint that the entire texture shape is within the domain.

4.4 Solution Method

Since the optimization problem in this study is nonlinear and constrained, the sequential quadratic programming (SQP) method is applied to determine the optimum texture shape. This method is considered to be more efficient and accurate than other nonlinear programming methods when solving problems of small to medium size [22]. The basic idea of SQP method is as follows: it begins with an initial guess of the design variables and evaluates the objective function at the starting point. Next, it solves the quadratic programming sub-problems to obtain the search direction and construct a better estimate. This process is iterated until the algorithm converges to an optimal solution. A number of optimization software packages are available that use this approach. In this work, the Matlab Optimization Toolbox is used to implement the SQP method.

When solving the Reynolds equation, the half-Sommerfeld cavitation boundary condition is applied in this study. However, Qiu and Khonsari [23] pointed out that the Jakobsson-Floberg-Olsson (JFO) boundary condition which ensures mass conservation is more realistic for predicting cavitation in surface textures. The reason half-Sommerfeld boundary condition was implemented in the simulation is that the implementation of the JFO boundary condition makes the computation

sensitive, especially when the texture shape is very irregular. This can cause divergence and thus interrupt the optimization process. Therefore, due to the robustness and simplicity of implementation, the half-Sommerfeld boundary condition was used for solving Reynolds equation in this work. The influence of half- Sommerfeld boundary condition is discussed in Section 4.8.

4.5 Benchmark Problem

The optimization problem of a two-dimensional slider bearing taken from Rhode and McAllister [24] serves as a benchmark problem to validate the present optimization method. In their study, Rhode and McAllister presented an optimization algorithm of two dimensional film profile using successive approximations. Then the optimum film thickness distribution of a square slider bearing was obtained with both finite difference method and finite element method. Figure 4-2 shows the schematic of a slider bearing, which has a square shape with side length of L and constant step depth h_g. In this case, the objective is to find the optimal pocket shape and step depth for maximizing the load-carrying capacity of the slider bearing.

The design variables and optimization method in Section 4.2 are applied to this problem. The only difference is that the pressures at all the boundaries of the domain are considered to be at the ambient pressure. The non-dimensional groups in Eq. (2) are also used for this example. Table 4-1 lists the basic parameters of the slider bearing. Their values do not affect the dimensionless results.

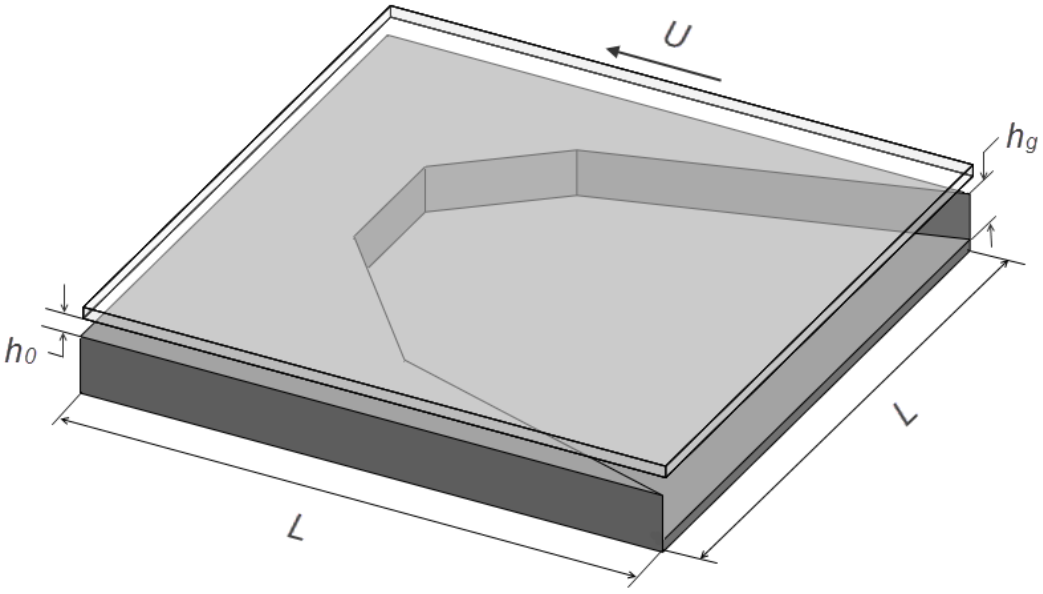

Figure 4-2 Schematic of a two-dimensional slider bearing

Table 4-1 Bearing geometry and lubricant parameters

Parameter	Value
Minimum film thickness, h_0	10 μm
Lubricant viscosity, μ	0.038 Pa·s
Sliding velocity, U	1 m/s
Bearing length, L	50 mm

Figure 4-3 (a) shows the optimum shape of slider bearing obtained with the optimization procedure described in Section 4.2. The details of the geometry are given in Table 4-3. It can be seen that the optimum shape is very similar to the result of Rhode and McAllister [24]. Especially, the maximum

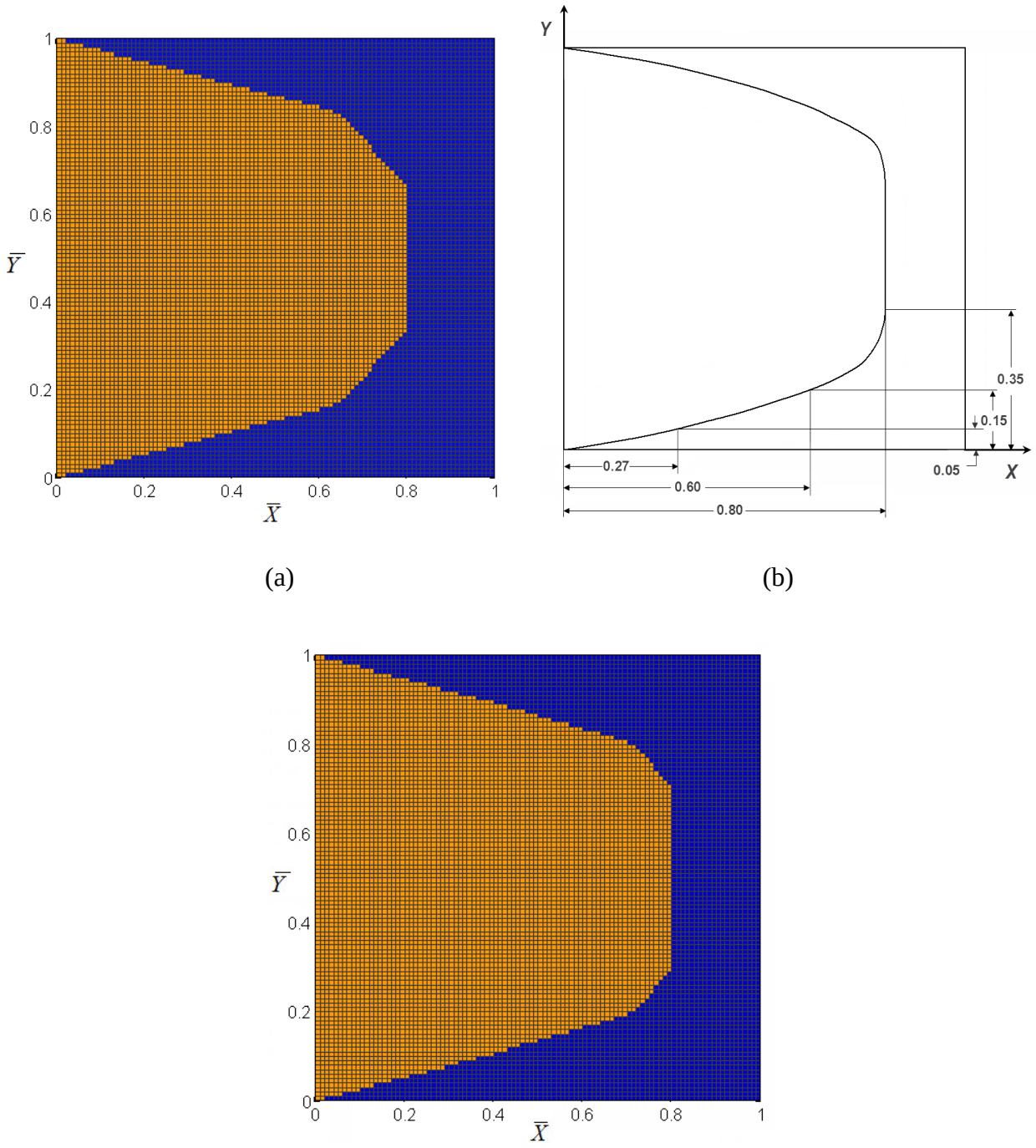

(a) (b)

(c)

Figure 4-3 Optimum shape of slider bearing (the yellow region is pocket and the blue region is land): (a) result obtained with six sections; (b) result from Rhode and McAllister [24] (c) result obtained with ten sections

lengths and depths of the pocket are the same. Some discrepancy between the two optimum shapes is mainly due to that the current method uses a finite number of sections to define the geometry of the pocket. Generally, the more divisions there are, the smoother the optimum shape will be. Figure 4-3 (c) shows the optimum shape obtained with ten sections. As can be seen, it is closer to the result of Rhode and McAllister. However, the number of design variables and hence the computational time increases substantially with the number of the divisions. For example, when the number of divisions is increased from 6 to10, the number of variables increases from 15 to 23 and the computational time increases by more than two fold. Based on the computing time and shape accuracy, the shape optimization were conducted with six sections in this study. In summary, the above results show that the present method is capable of finding the optimum geometry for the hydrodynamic lubrication problem.

4.6 Optimum Texture Shapes for Unidirectional Sliding

In this section, optimum texture shapes of unidirectional sliding are obtained for four area ratios. The area ratio (AR) is a critical geometrical parameter in surface texturing, defined as the ratio of the textured area to the total surface area. Wang et al. [25] reviewed published works on the effect of dimple area ratio on the tribological performance and concluded that for metals under oil lubrication the area ratio in the range of 5-13% is preferable for friction reduction while the ratio above 20% usually leads to an increase in friction. For materials with a low Young's modulus, like ultra-high molecular weight polyethylene (UHMPWE), a higher dimple area ratio (30%) still has the effect of friction reduction. Therefore, in this work the texture shape optimization is first carried out without any constraint on area ratio. Then, the optimum shapes are obtained for three area ratios (10%, 20% and 30%). The unit cell length L is 10 mm. Other parameters are the same as those in Table 4-1. The textured surface is stationary while the runner surface is moving along the

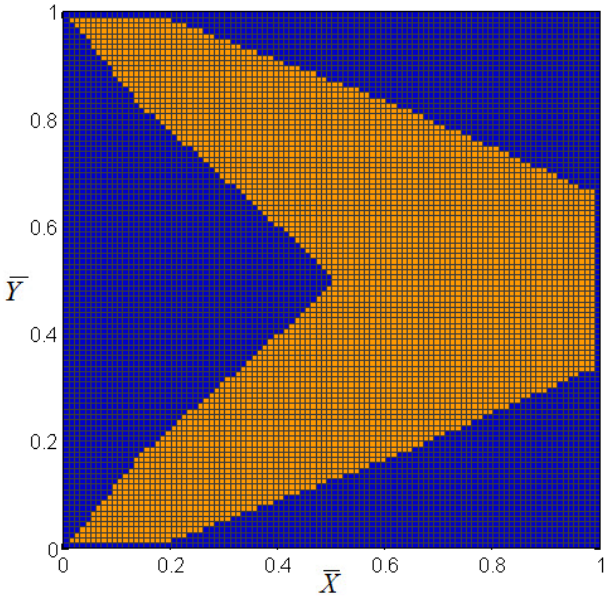

(a) No constraint of AR, $\overline{W}$ = 38.26, AR = 49%

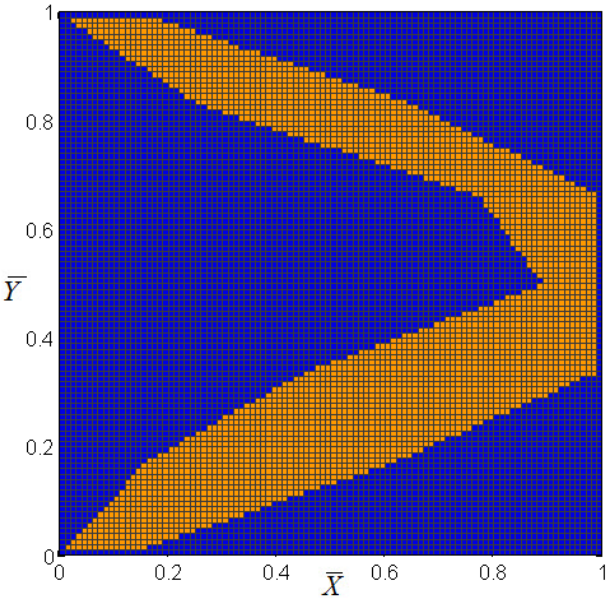

(b) AR = 30%, $\overline{W}$ = 36.12

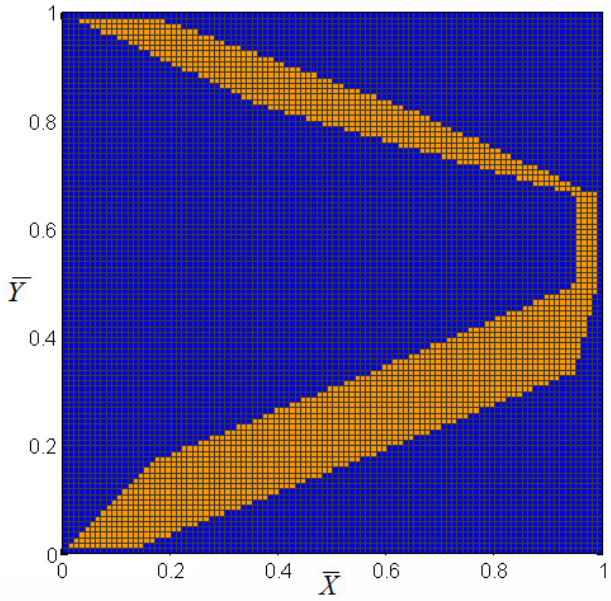

(c) AR = 20%, $\overline{W}$ = 32.96

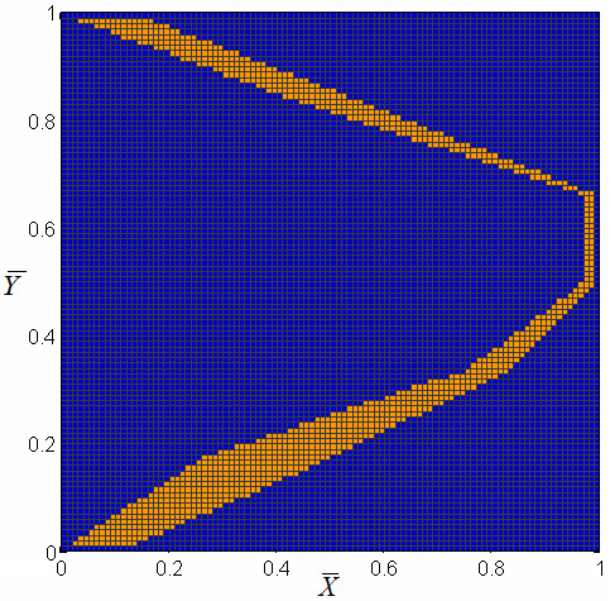

(d) AR = 10%, $\overline{W}$ = 25.74

Figure 4-4 Optimum texture shapes for unidirectional sliding

X-axis from left to right. Since the simulation does not involve nonlinear phenomena, such as surface deformation, large cavitation area and coupled thermal effects, the optimum texture shapes

are not affected by the operating conditions (speed, viscosity and minimum film thickness) and the size of the unit cell.

Figure 4-4 shows the optimum texture shapes for unidirectional sliding with no constraint of AR and constant ARs. The values of all design variables are listed in Table 4-2. As can be seen, the optimum texture geometries have very similar chevron-shapes with flat fronts. But the groove widths of the shapes decrease as the AR decreases. It should be mentioned that these optimum texture shapes are directional. In order to achieve the maximum LCC, the chevron front needs to be aligned parallel to and pointing in the sliding direction.

Table 4-2 Dimensionless design variables for slider bearing and directional textures

$\overline{X}_1$	$\overline{L}_1$	$\overline{X}_2$	$\overline{L}_2$	$\overline{X}_3$	$\overline{L}_3$	$\overline{X}_4$	$\overline{L}_4$	$\overline{X}_5$	$\overline{L}_5$	$\overline{X}_6$	$\overline{L}_6$	$\overline{X}_7$	$\overline{L}_7$	$\overline{h}_g$
Slider bearing														
0.00	0.00	0.32	0.64	0.40	0.80	0.40	0.80	0.40	0.80	0.32	0.64	0.00	0.00	1.21
Texture (No constraint of area ratio)														
0.10	0.18	0.38	0.48	0.66	0.66	0.75	0.48	0.66	0.66	0.38	0.48	0.10	0.18	1.63
Texture (Area ratio = 30%)														
0.08	0.14	0.39	0.46	0.72	0.54	0.94	0.10	0.88	0.22	0.46	0.40	0.09	0.16	1.86
Texture (Area ratio = 20%)														
0.07	0.12	0.36	0.38	0.76	0.38	0.97	0.04	0.97	0.04	0.50	0.26	0.10	0.16	2.06
Texture (Area ratio = 10%)														
0.07	0.12	0.38	0.24	0.79	0.08	0.98	0.02	0.98	0.02	0.52	0.12	0.09	0.14	2.46

Careful comparison of LCCs of texture shapes shown in Figure 4-4 reveals that there is an optimum value for AR which maximizes the LCC under the unidirectional sliding motion. The result of optimization without constraint on AR shows that the highest LCC occurs at the AR of 49%. Then the LCC of optimum texture shape decreases as the AR decreases. But the variation of the LCC is not very sensitive to the decrease of AR. For example, as the AR is decreased from 30% to 20%,

the LCC only reduces by around 9%. Also, it needs to be mentioned that the optimum AR obtained here is merely based on the LCC of textures under hydrodynamic lubrication. However, in actual applications, to allow for the reduction of the contact area and stress concentration caused by surface texturing, the area ratio is recommended to be less than 20% [25].

4.7 Optimum Texture Shapes for Bidirectional Sliding

In this section, shape optimization is conducted for surface textures under bidirectional sliding. To simplify the analysis, the transient phenomena in bidirectional sliding are not considered, and the sliding speed is maintained constant. The objective of this work is to find the optimum shapes of surface textures which generates the maximum LCC under hydrodynamic lubrication when bidirectional sliding takes place. Since the two sliding directions are opposite to each other, the texture shapes need to be symmetric about the centerline of the unit cell so as to obtain consistent LCC in the two directions. The design variables for the symmetric texture shape are only the lengths of the horizontal lines (L_1, L_2, ..., Ln) as their centers are always on the centerline of the unit cell. Figure 4-5 shows a schematic diagram of a symmetric texture for bidirectional sliding. In this study, the unit cell is divided to ten sections, which results in 12 design variables including the depth of the texture. All the input parameters are the same as those used in Section 4.5. The optimum shapes are obtained for four cases: no restriction of AR and ARs of 10%, 20% and 30%. In order to avoid the abrupt change of shape and sharp corners, a constraint that requires the angle between two successive sides of the texture to be greater than 90 degrees is imposed in the optimization process.

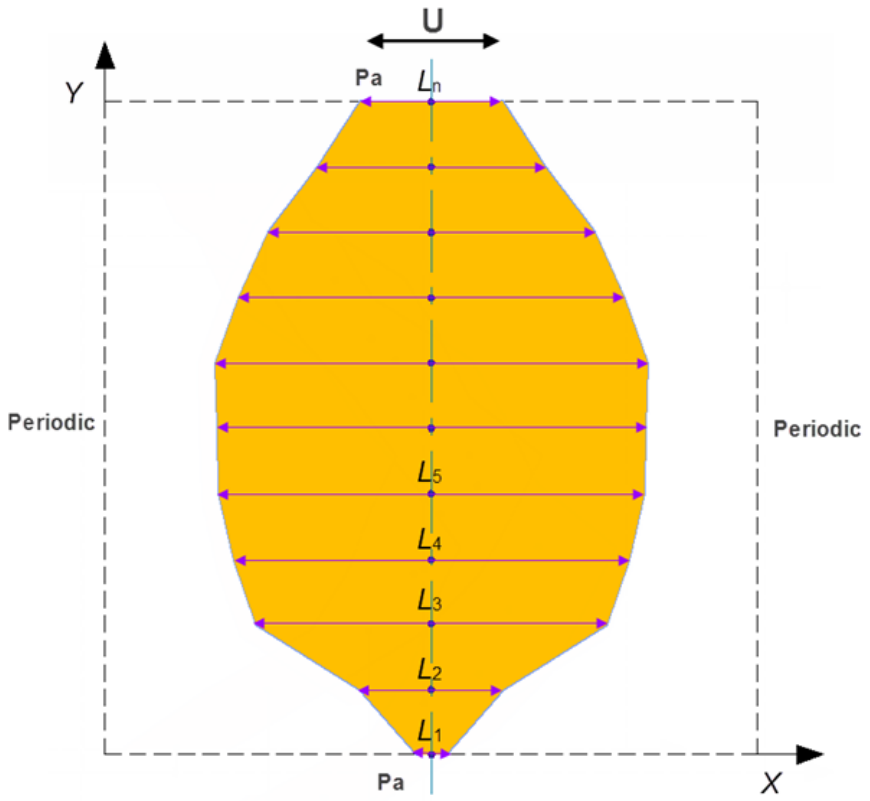

Figure 4-5 Design variables for a symmetric texture shape under bidirectional sliding

Figure 4-6 shows the profiles of optimized symmetric textures for bidirectional sliding. The details of all design variables are given in Table 4-3. It can be seen that the optimum texture shape changes with the value of AR. But all the optimum shapes consist of pairs of trapezoids that are symmetric to each other with respect to the centerline of the unit cell. This is understandable since a previous study shows that the optimum pocket shape of slider bearing is close to trapezoid [24]. It can be expected that the optimum symmetric shape is composed of pairs of the trapezoid-like shapes which are symmetric with respect to the centerline. So, when sliding in either direction of bidirectional motion, one half of the unit cell works as a pocketed slider bearing. Hence the trapezoid-like shape can help generate the maximum LCC.

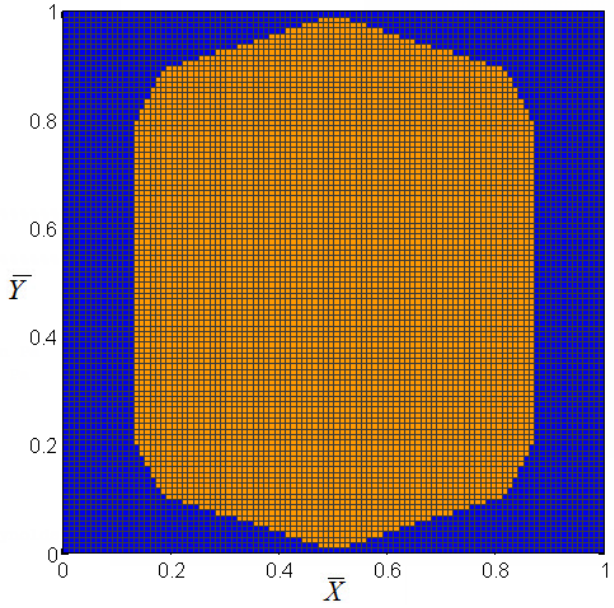

(a) No constraint of AR, $\overline{W}$ = 15.40, AR = 63.5%

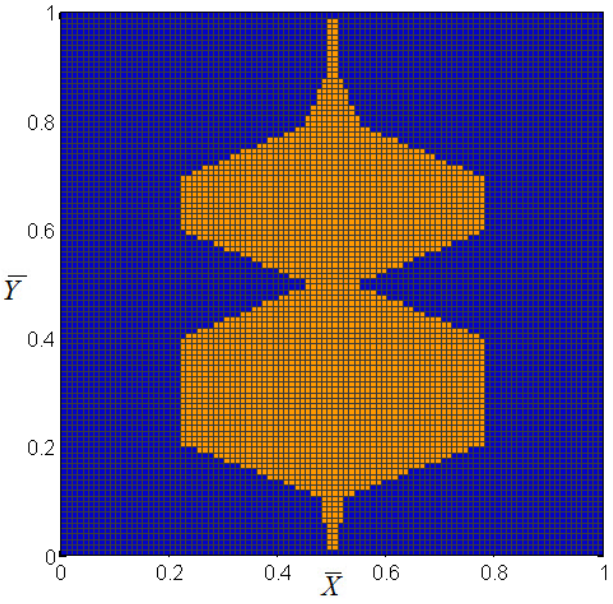

(b) AR = 30%, $\overline{W}$ = 10.94

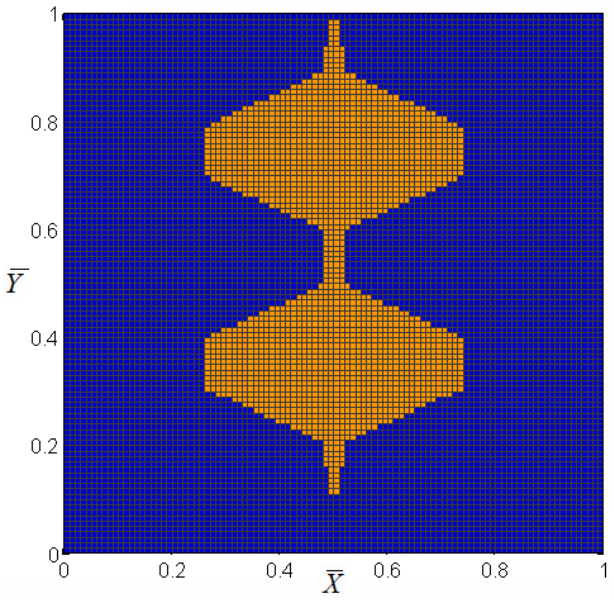

(c) AR = 20%, $\overline{W}$ = 8.62

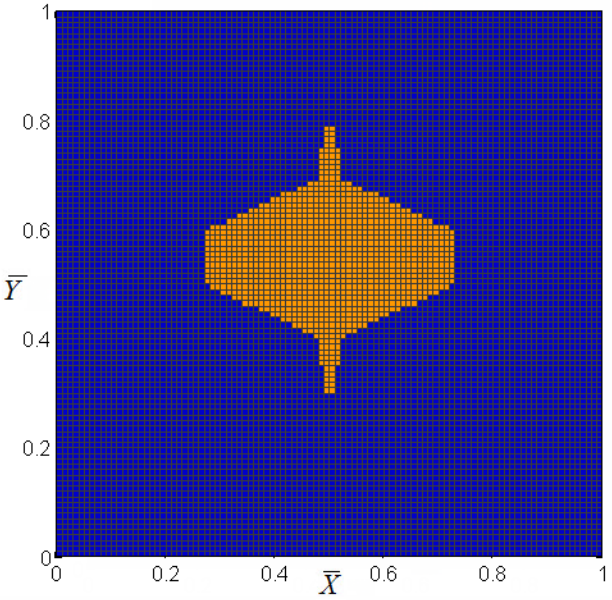

(d) AR = 10%, $\overline{W}$ = 4.98

Figure 4-6 Optimum texture shapes for bidirectional sliding

An investigation of LCCs of symmetric texture shapes in Figure 4-6 shows that the value of AR has a significant influence on the LCC and there is an optimum value of AR for the maximum LCC. In the case of symmetric texture shape, the highest LCC occurs at the AR of 63.5%. The

LCC of optimum texture shape also decreases with decreasing AR, and its value is sensitive to the variation of AR. For example, as the AR is decreased from 30% to 20%, the LCC is reduced by 21%.

Table 4-3 Dimensionless design variables for symmetric textures with different area ratios

AR	$\bar{L}_1$	$\bar{L}_2$	$\bar{L}_3$	$\bar{L}_4$	$\bar{L}_5$	$\bar{L}_6$	$\bar{L}_7$	$\bar{L}_8$	$\bar{L}_9$	$\bar{L}_{10}$	$\bar{L}_{11}$	$\bar{h}_g$
-	0.02	0.64	0.74	0.74	0.74	0.74	0.74	0.74	0.74	0.64	0.02	1.00
30%	0.02	0.04	0.56	0.56	0.56	0.08	0.56	0.56	0.10	0.02	0.02	0.84
20%	0.00	0.02	0.04	0.47	0.47	0.04	0.04	0.47	0.47	0.04	0.02	0.83
10%	0.00	0.00	0.00	0.02	0.04	0.46	0.46	0.04	0.02	0.00	0.00	0.85

4.8 Comparison with Regular Texture Shapes

In this section, the performances of optimum texture shapes obtained in previous sections are compared with those of regular shapes that are ordinarily used in surface texturing. Five regular texture shapes are considered in this study. Their shapes, equations of AR and the maximum possible values of AR are listed in Table 4-4. Since JFO boundary condition is more realistic for cavitation in surface texture, a mass-conservative algorithm is used to predict of the LCCs of different texture shapes. The influence of using half-Sommerfeld boundary condition in the shape optimization is also discussed.

Elrod's mass conservative form of the Reynolds equation [26] is used to predict the pressure distribution in the lubricant film. In dimensionless form, this equation can be written as

$$\frac{\partial}{\partial \bar{x}}\left(\frac{\bar{h}^3 g \partial \varphi}{\partial \bar{x}}\right)+\frac{\partial}{\partial \bar{y}}\left(\frac{\bar{h}^3 g \partial \varphi}{\partial \bar{y}}\right)=\lambda \frac{\partial \varphi \bar{h}}{\partial \bar{x}} \tag{5}$$

where g is the switch function that distinguishes the boundaries of cavitation region and φ is the film content parameter ($\varphi = \rho/\rho_c$).

Table 4-4 Regular symmetric texture geometries

No.	Texture Geometry	Description	Area Ratio (AR)	Maximum AR
1	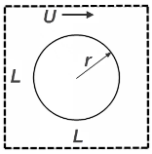	Circle	$\frac{\pi r^2}{L^2}$	78.5%
2	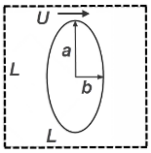	Ellipse (a = 2b)	$\frac{\pi ab}{L^2}$	39.3%
3	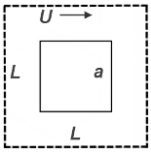	Square	$\frac{\pi a^2}{L^2}$	100%
4		Hexagon	$\frac{3\sqrt{3}a^2}{2L^2}$	65%
5	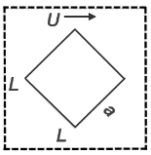	Diamond	$\frac{\pi a^2}{L^2}$	50%

The non-dimensional terms are defined the same as those in Eq. (2). The characteristic number λ describes the operating conditions and is defined as:

$$\lambda = \frac{6\mu L U}{\beta\, h_0^2} \tag{6}$$

The governing equation is then discretized using the finite difference method and solved by a multi-grid method. Once the pressure distribution is determined, the LCC of a single texture can be calculated by integrating the pressure over the entire domain. The details of the solution method are given in Ref. [23]. Table 4-5 shows the basic input parameters used in the comparison.

Table 4-5 The input parameters for the simulation

Parameter	Value
Unit cell length L (mm)	5
Texture depth h_g (μm)	10
Minimum film thickness h_0 (μm)	4
Area ratio of texture	30%, 20%, 10%
Viscosity μ (Pa.s)	0.038
Cavitation pressure p_c (Pa)	0.9×10^5, 0.3×10^5
Ambient pressure p_0 (Pa)	1×10^5 Pa
Bulk modulus β (Pa)	1.62×10^9 Pa
Sliding speed U (m/s)	0.01 – 5.12

The non-dimensional parameter λ represents the operating condition of the simultion. It is proportional to the lubricant viscosity μ, sliding velocity U, and the inverse of the bulk modulus β. Figure 4-7 shows the effect of texture shape on the dimensionlesss LCC under different values of λ. According to Ref. [27], the cavitation pressure can significantly affect the simulation results of the mass-conservative algorithm, and that the value of cavitation pressure under steady-state lubrication can vary from 30 kPa to 90 kPa depending on the operating conditions. Hence, two cavitation pressures were used in the simulations to consider the effect of cavitation pressure.

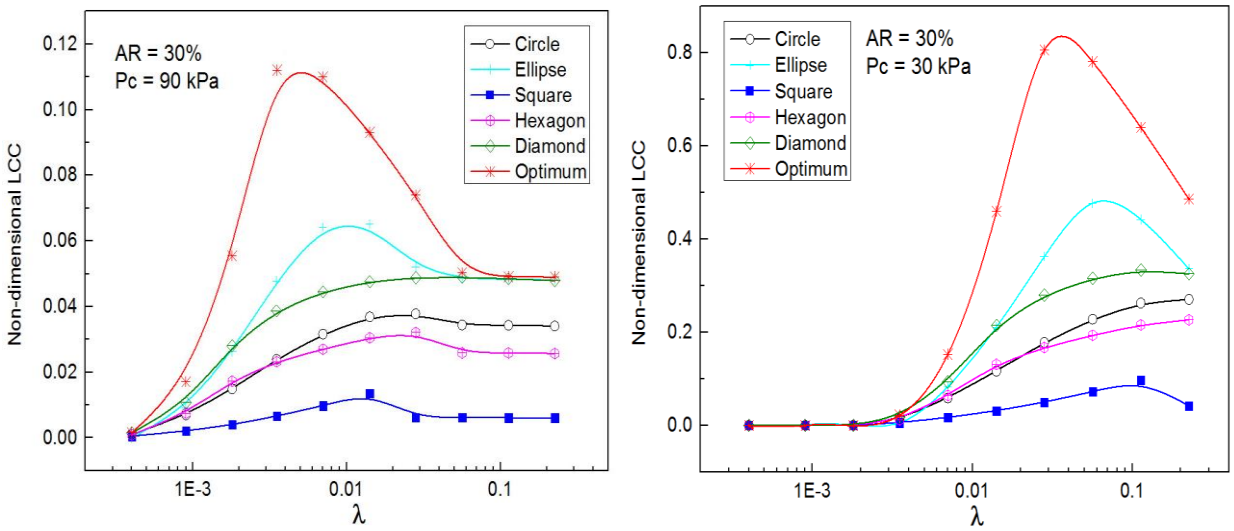

Figure 4-7 Comparison between optimum symmetric shape and regular shapes (AR=30%)

The simulation results of textures with AR of 30% are shown in Figure 4-7. For the cavitation pressure of 90 kPa, the LCCs increase to a maximum value and then gradually decrease as λ is increased. The LCCs under cavitation pressure of 30 kPa show similar trend, but are higher in magnitude. These results indicate that there exists an optimum λ for each texture shape that produces the maximum LCC. More significantly, Figure 4-7 show that the LCC of surface texture is greatly influenced by its shape. Compared with the elliptical dimple which performs the best among the regular shapes of textures, the optimum symmetric texture (see Figure 4-6 (b)) can almost double the LCC under certain operating conditions. And the LCC of the optimum texture shape is always greater than or equal to those of regular shapes regardless of the values of cavitation pressure and λ.

Since the LCCs of optimum directional shapes (see Figure 4-4) are much higher, their values are shown separately in Figure 4-10. Compared with the symmetric texture shapes, the LCC of the optimum directional shape shows a different trend. It increases monotonically with increasing λ and its value is tens of times higher than those of regular textures.

Figure 4-8 shows the dimensionless hydrodynamic pressure distributions generated by textures with AR of 30%. The flow direciton of the lubricant is from left to right in the figure. It can be seen that the lubricant film cavitates in the diverging area (left part of the texture) while the highest pressure occurs around the right rim of the texture. The LCC of a texture depends on the area of pressure build-up and the peak pressure of this region. Among all the symmetric shapes, the elliptical shape has the largest area of pressure build-up. But its maximum pressure in this region is relatively low compared to other shapes. On the other hand, the diamond shape generates the highest peak pressure but possesses a small pressure build-up region. When compared to regular shapes, the optimum symmetric shape has a good balance between the pressure build-up area and the peak pressure, which leads to a higher LCC.

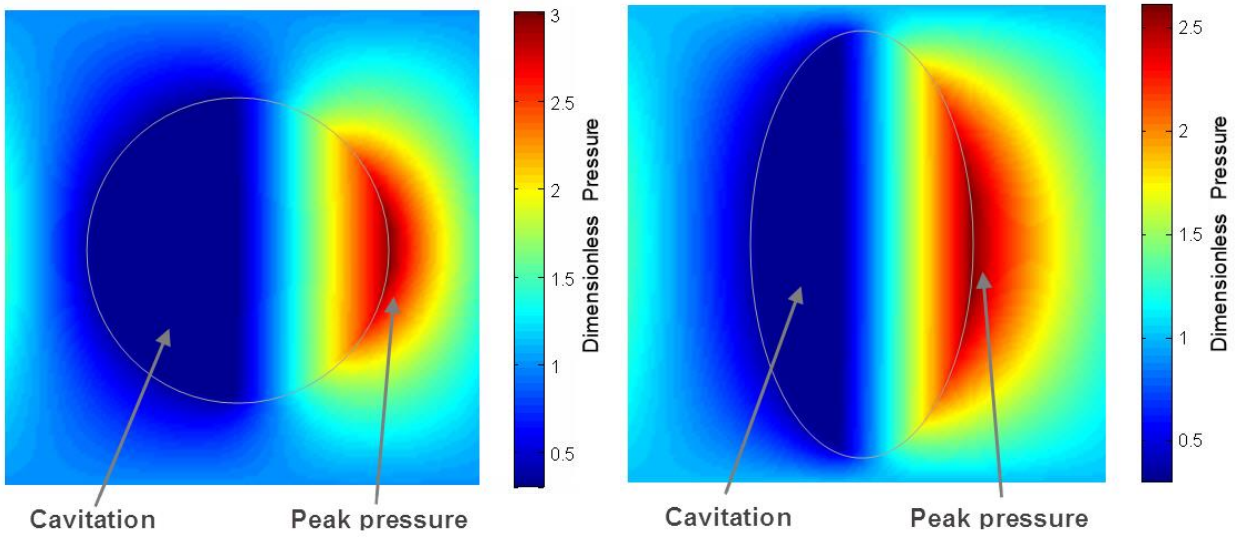

(a) Circle (b) Ellipse

Figure 4-8 Pressure distributions of different texture shapes (figure continued)

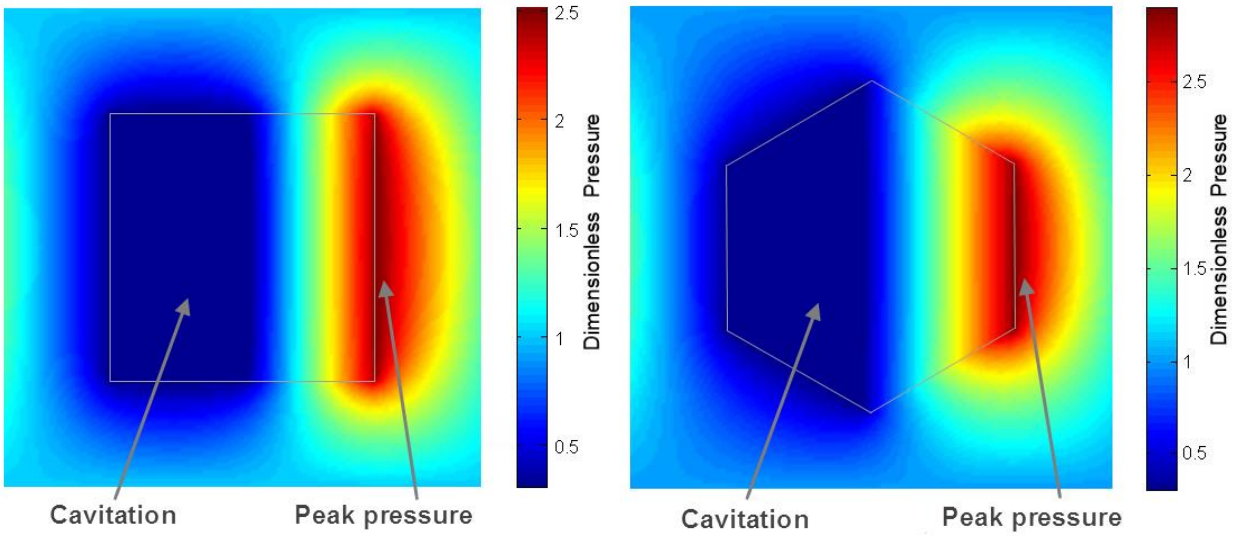

(c) Square (d) Hexagon

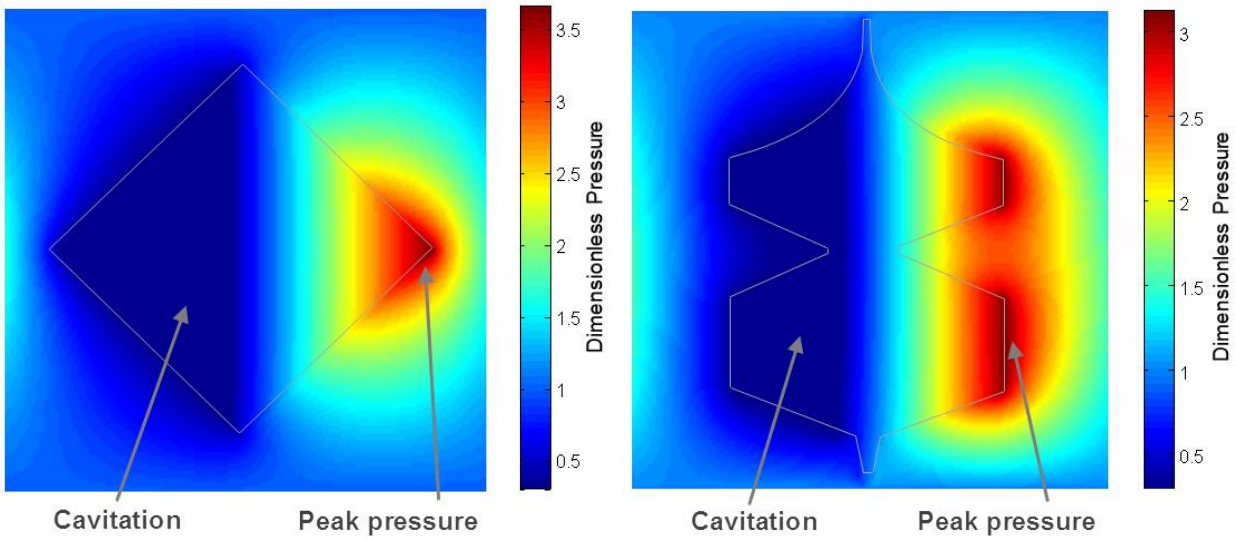

(e) Diamond (f) Optimum (symmetric)

Figure 4-8 Pressure distributions of different texture shapes (figure continued)

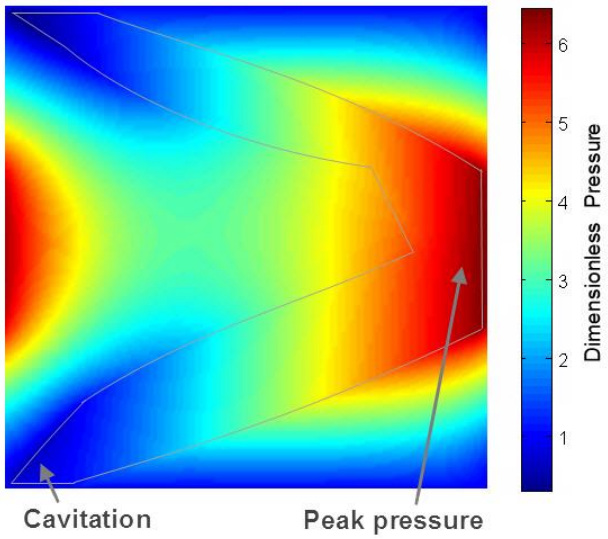

(g) Optimum (directional)

Figure 4-8 Pressure distributions of different texture shapes

The pressure distribution of the optimum directional texture shape is shown in Figure 4-8(g). As can be seen, its cavitation area is very limited while the peak pressure is at least twice more than those of regular textures. This explains the very high LCC of the optimum directional texture. But this type of texture shape can only be used for unidirectional sliding.

The simulation results for different texture shapes with ARs of 10% and 20% are shown in Figure 4-9. The trends of the LCC curves are the same as those present in Figure 4-7. However, the advantage of the optimum symmetric shape on the LCC diminishes as the AR is decreased from 30% to 10%. It can be seen that the optimum symmetric texture generates higher LCC than regular texture only when the value of λ is low (less than 0.02), and the enhancement of LCC decreases with decreasing AR. One reason for this effect is the difference between texture shapes becomes smaller as the texture area (area ratio) is decreased. Another reason is the usage of the half-Sommerfeld boundary condition in the optimization process. When the half-Sommerfeld boundary condition is applied to predict the pressure distribution, the lubricant film in half of the unit cell is

cavitated and the boundary between the cavitation and full-film region is in the middle of the cell. As a result, the cavitation ratio (the ratio of cavitation area in texture to total texture area) is always equal to 50% for half-Sommerfeld boundary condition. However, the cavitation ratio varies with λ using JFO boundary condition. When the value of λ is low, the cavitation ratio is approximately equal to or less than 50% (as shown in Figure 4-8, λ=0.009). As a result, the shape optimization results based on half-Sommerfeld boundary condition are still valid under JFO boundary condition in this case. However, as the value of λ increases, the caviation area increases. It can take up most of the area within a texture when λ is high. Under this condition, the optimum shapes obtained with half-Sommerfeld boundary condition does not generate the highest LCC anymore since the pressure distribution is affected by the large cavitation region.

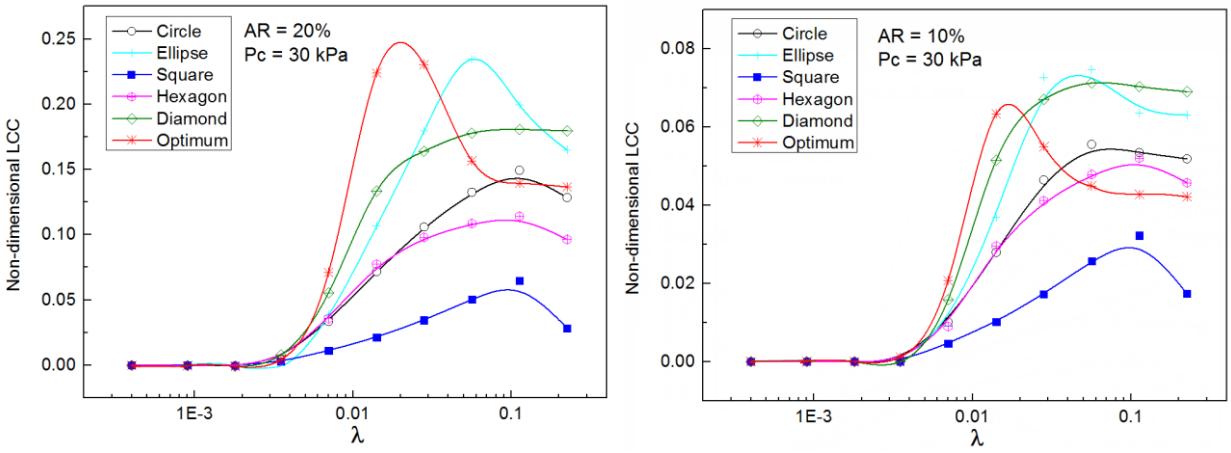

Figure 4-9 Comparison between optimum symmetric and regular shapes (AR=20% and 10%)

The phenomenon that cavitation region varies with operating conditions is observed experimentally by Cross et al. [28]. They found that the cavitation area within a circular pocket increases as the lubricant viscosity or sliding speed is increased. This agrees with simulation results of JFO boundary condition, which shows that the cavitation region increases with increasing λ. The results indicate that the optimum texture shape under JFO boudnary condition may change

with operating conditions for the cavtiation ratio changes with speed and viscosity. Futher study is needed for the texture shape optimization with JFO boundary condition. However, for the directional texture shapes, the influence of using the half-Sommerfeld boundary condition is very limited, because the cavitation region in these shapes is very small (as shown in Figure 4-8 (g)). As a result, the decrease of texture area has little impact on their LCCs. The optimum directional shapes at area ratios of 10% and 20% still perform much better than regular shapes under different operating conditions.

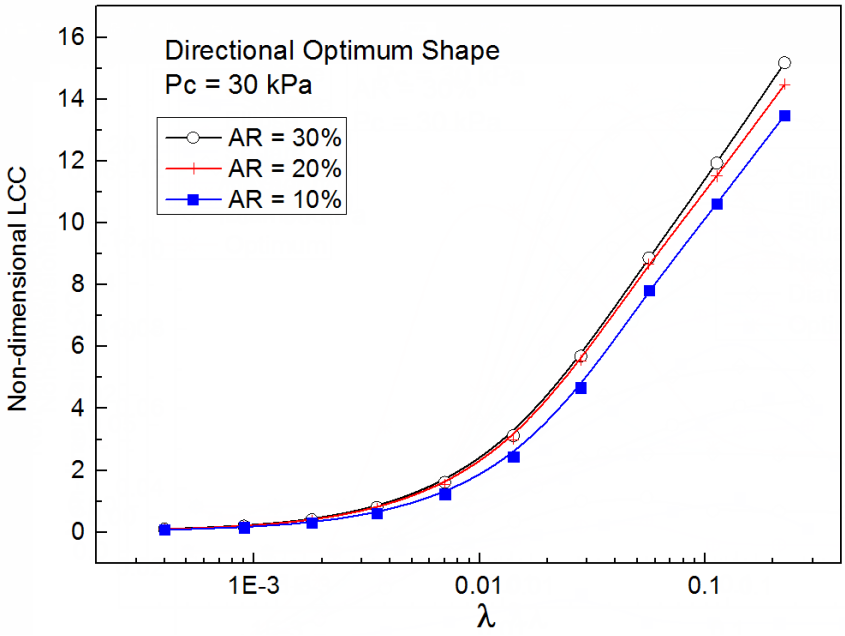

Figure 4-10 LCCs of optimum directional texture shapes

4.9 Conclusions

This study presents a numerical optimization approach based on the SQP algorithm for the texture shape optimization of parallel surfaces. In order to validate this method, a shape optimization problem of two dimensional slider bearing is first solved and compared with the published results. Then novel texture shapes that produce the maximum LCC for unidirectional and bidirectional sliding are proposed and analyzed. It is shown that the optimum directional textures for

unidirectional sliding have chevron-shapes with flat fronts while the optimum symmetric textures for bidirectional sliding is composed of pairs of the trapezoid-like shapes. Finally, the performances of optimum textures are compared with five regular texture shapes using a mass-conservative algorithm. Simulation results show that under different operating conditions and cavitation pressures, the proposed optimum symmetric shape always have greater LCC than the regular shapes at area ratio of 30%. However, the advantage of optimum symmetric shapes diminishes as the area ratio is decreased. One possible reason for that is the usage of half-Sommerfeld boundary condition in the numerical optimization. Since there is little cavitation area in optimum directional shape, the influence of using half-Sommerfeld boundary condition is very small in this case. The texture shape optimization with JFO boundary condition and with consideration of thermal effects needs further study and will be considered in the future works.

4.10 References

[1] Wang X., Kato K., Adachi K., Aizawa K., 2003, " Loads carrying capacity map for the surface texture design of SiC thrust bearing sliding in water," Tribol. Int., 36, pp. 189–97.

[2] Etsion, I., Kligerman Y., 1999, "Analytical and experimental investigation of laser-textured mechanical seal faces," Tribol. Trans., 42(3), pp. 511–516.

[3] Etsion I., Halperin G., Brizmer V., Kligerman Y., 2004, "Experimental investigation of laser surface textured parallel thrust bearings," Tribol. Lett., 17(2), pp. 295–300.

[4] Kovalchenko A., Ajayi O., Erdemir A., Fenske G., Etsion I., 2005, "The effect of laser surface texturing on transitions in lubrication regimes during unidirectional sliding contact," Tribol. Int., 38, pp. 219–225.

[5] Wang X., Kato K., 2003, "Improving the anti-seizure ability of SiC seal in water with RIE texturing," Tribol. Lett., 14, pp.275–280.

[6] Etsion, I., and Burstein, L., 1996, "A model for mechanical seals with regular micro surface structure," Tribol. Trans., 39, pp. 677–683.

[7] Wang X., Adachi K., Otsuka K., Kato K., 2006, "Optimization of the surface texture for silicon carbide sliding in water," Appl. Surf. Sci., 253(3), pp. 1282–6.

[8] Costa, H. L. and Hutchings, I. M., 2007, "Hydrodynamic Lubrication of Textured Steel Surfaces under Reciprocating Sliding Conditions," Tribol. Int., 40, pp. 1227-1238.

[9] Galda L., Pawlus P., Sep J., 2009, "Dimples shape and distribution effect on characteristics of Stribeck curve", Tribol. Int., 42, pp.1505–1512.

[10] Yu, H., Wang, X., Zhou, F., 2010, "Geometric shape effects of surface texture on the generation of hydrodynamic pressure between conformal contacting surfaces", Tribol. Lett., 37, pp.123-130.

[11] Yan D., Qu N., Li H., Wang X., 2010, Significance of dimple parameters on the friction of sliding surfaces investigated by orthogonal experiments. Tribol. Trans., 53, pp. 703-712.

[12] Yuan, S., Huang, W., Wang, X., 2011, "Orientation effects of micro-grooves on sliding surfaces", Tribol. Int., 44, pp. 1047–1054.

[13] Qiu, Y., Khonsari M.M., 2011, "Performance analysis of full-film textured surfaces with consideration of roughness effects", ASME J. Tribol., 133, pp. 021704:1-10.

[14] Qiu, Y., Khonsari M.M., 2011, "Experimental investigation of tribological performance of laser textured stainless steel rings", Tribol. Int., 44, pp. 635-644.

[15] Shen C., Khonsari M. M., 2013, "Effect of dimple's internal structure on hydrodynamic lubrication", Tribol. Lett., 52, pp. 415–430.

[16] Wang, X., S.M. Hsu, 2004, "An integrated surface technology for friction control: a new paradigm effects of geometric shapes on friction", in The 4th China International Symposium on Tribology. Xi'an.

[17] Lu, X., Khonsari, M.M., 2007, "An experimental investigation of dimple effect on the stribeck curve of journal bearings", Tribol. Lett., 27, pp. 169–176.

[18] Qiu, M., Delic A., Raeymaekers B., 2012, "The effect of texture shape on the load-carrying capacity of gas-lubricated parallel slider bearings", Tribol. Lett., 48, pp. 315–27.

[19] Fesanghary M., Khonsari M.M., 2013, "On the optimum groove shapes for load-carrying capacity enhancement in parallel flat surface bearings: theory and experiment", Tribol. Int., 67, pp. 254 – 262.

[20] Khonsari, M. M. and Booser, E. R., 2001, "Applied Tribology-Bearing Design and Lubrication," John Wiley & Sons, Inc., Sussex, UK.

[21] Thorson J., 1979, "Gaussian elimination on a banded matrix", Stanford University, (Stanford Exploration Project).

[22] Spellucci P., 1998, “An SQP method for general nonlinear programs using only equality constrained subproblems”, Mathematical Programming, 82 (3), pp. 413–48.

[23] Qiu, Y., Khonsari, M. M., 2009, “On the prediction of cavitation in dimples using a mass-conservative algorithm”, ASME J. Tribol., 131, pp. 041702:1-11.

[24] Rohde S.M., McAllister G.T., 1976, “On the optimization of fluid film Bearings”, Proc. R. Soc. London, 351, pp. 481–497.

[25] Wang, X., Wang, J., Zhang, B., Huang W., 2014, “Design principles for the area density of dimple patterns”, Proceedings of the Institution of Mechanical Engineers, Part J: Journal of Engineering Tribology, Published online.

[26] Elrod, H. G., 1981, “A cavitation algorithm,” ASME J. Lubr. Technol., 103(3), pp. 350-354.

[27] Shen, C. and Khonsari, M. M., 2013, “On the magnitude of cavitation pressure of steady-state lubrication,” Tribol. Lett., 51, pp.153-160.

[28] Cross, A. T., Sadeghi, F., Cao, L. J., Rateick, R. G. and Rowan, S., 2012, “Flow visualization in a pocketed thrust washer”, Tribol. Trans., 55, pp. 571-581.

CHAPTER 5 TEXTURE SHAPE OPTIMIZATION FOR SEAL-LIKE PARALLEL SURFACES: THEORY AND EXPERIMENT

5.1 Nomenclature

d_k Search direction of the optimization algorithm

h Local film thickness (m)

h_0 Minimum film thickness (m)

h_g Texture depth (m)

$\bar{h}$ Dimensionless local film thickness, h/h_0

p Local Pressure (Pa)

p_0 Ambient pressure (Pa)

$\bar{p}$ Dimensionless pressure, p/p_0

r Local coordinate in radial direction (m)

r_i Inner radius of the unit cell (m)

r_o Outer radius of the unit cell (m)

$\bar{r}$ Dimensionless radial coordinate, r/r_i

$\overline{W}$ Dimensionless load-carrying capacity

α_k Step length of the optimization algorithm

θ Angular coordinate (rad)

θ_0 Sector angle of a texture column (rad)

$\bar{\theta}$ Dimensionless angular coordinate

μ Lubricant viscosity (Pa.s)

λ Characteristic number, $6\mu\omega r_i^2 / p_0 h_0^2$

ω Angular velocity of the upper specimen (rad/s)

5.2 Introduction

By producing artificial micro-features (dimples, grooves or asperities) on the surface, surface texturing can work as an effective method to alter the properties of surfaces, such as wettability, adhesion and heat transfer [1, 2]. One of the most successful application areas of surface texturing is to enhance the tribological performance of sliding surfaces, especially under liquid lubrication [3]. A generally accepted mechanism for the friction reduction is that the micro textures generate additional hydrodynamic pressure to support the load, which works akin to tiny hydrodynamic bearings.

With the development of manufacturing technology, such as laser ablation, reactive ion etching and electrochemical micromachining, the micro textures can be fabricated with high accuracy and good controllability, which enables great flexibility in texture design. Over the last decade, a large number of theoretical and experimental studies have been devoted to the design of surface textures for friction reduction under liquid lubrication. Many important geometrical parameters have been identified and investigated, including depth-to-diameter ratio, area ratio and dimple size. An early work on this subject is reported by Etsion et al. [4] who investigated the design parameters of spherical shape dimples and found that the depth-to-diameter ratio has a significant influence on the fluid film pressure. Their results show that the optimal depth-to-diameter ratio, which generates the highest average pressure, should be less than 0.05 for seal parameters greater than 1. Wang et

al. [5] conducted a series of experiments to investigate the effects of dimple diameter, depth and area ratio on the performance of SiC thrust bearing under water lubrication. The best performance of the SiC bearing was obtained when using dimples with diameter of 350 μm, depth of 3.2 μm and area density of 5%. Yan et al. [6] experimentally evaluated the significance of dimple diameter, depth and area ratio to the frictional behavior. Their analysis suggests that dimple area ratio is the most important parameter. More references on this subject can be found in [7-12]. A review of these papers reveals that the primary focus of these studies is on the design parameters of circular dimples. The interested readers can refer to reference [13], which summarized the shapes, dimensions and fabrication methods of surface textures used in recent studies.

On the other hand, some researchers have used textures with shapes other than circular dimples to investigate the shape and orientation effect of surface textures. Lu and Khonsari [14] compared the frictional performance of journal bearings whose bushing inner surfaces were textured with circular and elliptical dimples. They found that the elliptical dimples offer a lower friction coefficient under the mixed lubrication. Galda et al. [15] investigated the Stribeck curves of specimens with spherical, long-drop and short-drop dimples using a block-on-ring test rig. Their results indicates that friction coefficients of spherical and long-drop dimples are lower than that of the short-drop dimple. Yu et al. [16] compared the average hydrodynamic pressures of textures with three shapes (circle, ellipse and triangle) and two orientations (parallel and perpendicular to the sliding direction). Their results show that the elliptical dimple with major axis perpendicular to the sliding direction generates the highest average pressure. The geometric parameters of non-circular textures, such as square dimple, radial groove, ellipsoidal dimples, were also optimized in several studies [17-20]. They found that the tribological performance of textured surface (either

load-carrying capacity or friction coefficient) can be greatly improved by using optimum geometry of the regular texture shapes.

The above studies show that the texture shape can have a major effect on the tribological performance of textured surface. Other than using some regular texture shapes, a mathematical optimization method was developed in a previous work [21] to find the global-optimum texture shapes under different constraints. The shape optimization results were obtained in Cartesian coordinates for linear sliding motion. The objective of this study is to apply the optimization method to surface textures under rotational motion and experimentally evaluate the performance of optimum texture shapes. For this purpose, the shape optimization algorithm is extended to a ring-shape geometry using the polar coordinates. The optimization results can be applied to mechanical components which have rotating parallel surfaces, such as mechanical seals and thrust washers. Then, specimens were prepared and laboratory tests were carried out to compare the performances of different types of surface textures and verify the results of the optimization.

5.3 Problem Formulation

5.3.1 Computational Domain and Design Variables

Figure 5-1 shows the geometrical model of the textured ring specimen, which is stationary during operation. An upper ring with smooth surface is rotating relative to it. The textures are uniformly distributed along the radial direction with a constant depth h_g, leading to an axisymmetric configuration. Hence, it is sufficient to evaluate the performance of the ring specimen by analyzing only one texture column. To further simplify the formulation, a single-cell model, as shown in Figure 5-1, is used in this study.

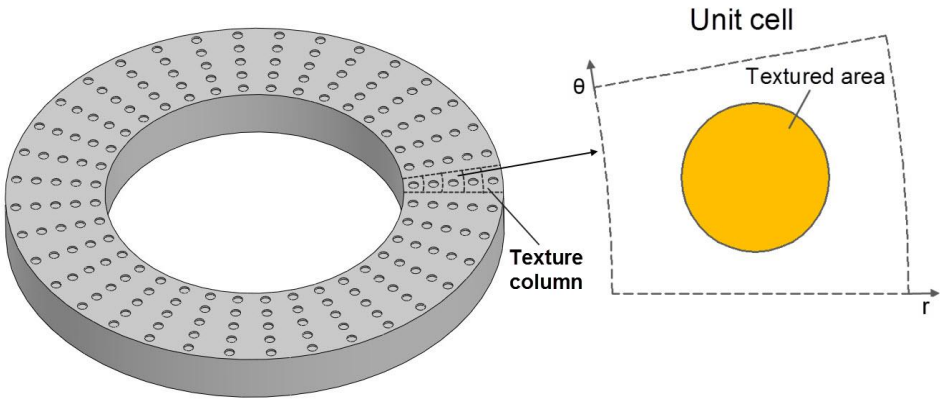

(a)

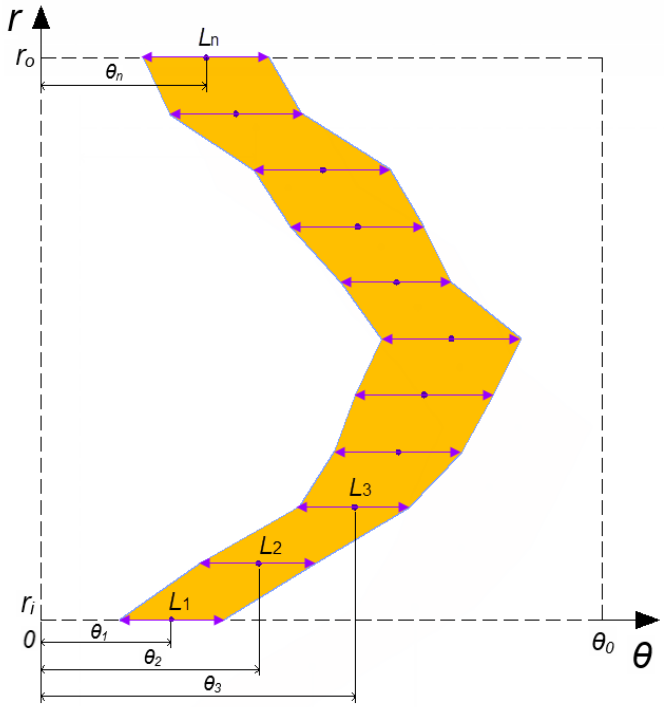

(b)

Figure 5-1 Geometrical model for texture shape optimization: (a) a typical unit cell for a ring specimen; (b) design variables for an arbitrary texture shape in polar coordinates

This model considers a fan-shape unit cell in the middle of texture column containing a single pattern as the computational domain. Periodic boundary conditions are applied in the rotating direction (θ) to account for the interaction between textures. Assuming that the interaction in the

radial direction (r) is negligible, the pressures on the inner and outer radius of the unit cell are maintained at ambient pressure. The textured surface is stationary and the runner surface moves with a rotational velocity ω in the counterclockwise direction. The objective of this work is to find the optimum texture shape within the unit cell which maximizes the load-carrying capacity (LCC) of the textured surface.

The texture geometry within the unit cell can be evenly divided in radial direction by imaginary lines with a constant radius. These lines are horizontal in polar coordinates, as shown in Figure 5-1(b). An arbitrary texture shape can be formed by connecting the adjacent horizontal lines with known lengths and center locations. Therefore, the design variables for a texture shape in polar coordinates are simply the lengths (L_1, L_2, ..., L_n) and corresponding center locations (θ_1, θ_2, ..., θ_n) of these horizontal lines. The constant texture depth (h_g) can also be optimized as a design variable. In this study, the fan-shape unit cell is divided to six sections in the radial direction, which results in 15 design variables. The number of sections is selected with the consideration of the computing time and shape accuracy. A previous study shows that the computing time increases by more than two fold if the number of sections is increased from six to ten, but the obtained optimal shapes are very similar [21]. Therefore, six sections are used in this study. The optimization algorithm then adjusts the values of these design variables to find the texture shape with maximum LCC. This method is similar to the one used in Refs. [21, 22].

5.3.2 Governing Equation and Solution Method

Assuming that the lubricant is Newtonian and incompressible and that the thermal and inertial effects are negligible, the hydrodynamic pressure distribution $p(\theta, r)$ within the unit cell can be predicted by the steady-state Reynolds equation. The non-dimensional Reynolds equation takes on the following form in polar coordinates:

$$\frac{1}{\bar{r}}\frac{\partial}{\partial \bar{r}}\left(\bar{r}\bar{h}^3\frac{\partial \bar{p}}{\partial \bar{r}}\right)+\frac{1}{\bar{r}}\frac{\partial}{\partial \bar{\theta}}\left(\frac{\bar{h}^3}{\bar{r}}\frac{\partial \bar{p}}{\partial \bar{\theta}}\right)=\lambda\frac{\partial \bar{h}}{\partial \bar{\theta}} \tag{1}$$

The dimensionless terms in Eq. (1) are defined as follows:

$$\bar{r}=\frac{r}{r_i},\ \bar{\theta}=\frac{\theta}{\theta_0},\ \bar{h}=\frac{h}{h_0},\ \bar{p}=\frac{p}{p_0},\ \lambda=\frac{6\mu\omega}{p_0}\left(\frac{r_i}{h_0}\right)^2 \tag{2}$$

where r_i is the inner radius of the unit cell, θ_0 is the sector angle of the unit cell, h_0 is the minimum film thickness and p_0 is the ambient pressure.

The Reynolds Equation Eq. (1) was discretized by the finite difference method and then solved by a fast direct solver based on LU decomposition [23]. Due to the robustness and simplicity of implementation, half-Sommerfeld cavitation boundary condition was applied in this study, which set the negative pressure in the solution to zero. More elaborate Jakobsson-Floberg-Olsson (JFO) boundary condition could be used in the simulation. However, its implementation to problems involving lubricant film with very irregular shape makes the computations sensitive and could lead to numerical instability. It should also be mentioned that the Reynolds boundary condition was not used in the current study since it greatly underestimate the cavitation area within a texture under hydrodynamic lubrication, according to the results of extensive simulations presented in [24]. The influence of half-Sommerfeld boundary condition was investigated by a parametric study. The results show that for optimum texture shapes the error caused by using this boundary condition is less than 5% compared to those with JFO boundary condition.

The non-dimensional LCC of a single texture is obtained by integrating the pressure over the unit cell.

$$\overline{W} = \int_0^1 \int_1^{\frac{r_o}{r_i}} \overline{p}\overline{r}d\overline{r}d\overline{\theta} \tag{3}$$

The optimization objective is to determine the design variables $\overline{\theta}_1$, $\overline{L}_1$, ..., $\overline{\theta}_n$, $\overline{L}_n$, $\overline{h}_g$ that maximize the LCC and subject to the constraint that the texture shape is within the unit cell.

The sequential quadratic programming (SQP) method is employed as the optimization algorithm to search the optimum texture shape. This method is considered to be one of the most efficient and accurate procedures for solving constrained nonlinear optimization problems of small to medium size [25]. It converts the nonlinear optimization problem into a sequence of quadratic optimization problems which are easier to solve. At each iteration of the optimization process, a quadratic approximation of the Lagrangian function for the optimization problem is minimized together with a linearization of the constraints to obtain the search direction d_k. Then, the step length (α_k) is calculated by performing a line search with respect to a merit function. A new iterate is given by

$$x_{k+1} = x_k + \alpha_k d_k \tag{4}$$

This optimization procedure is repeated until the convergence criterion is satisfied.

For the texture shape optimization, the algorithm begins with an initial guess of the design variables and evaluates the load-carrying capacity at the starting point. Then, it iterates to construct a better estimate until the algorithm converges to an optimal solution. In this study, the Matlab Optimization Toolbox is used to implement the SQP method. More details of the procedure are available in [21, 22].

5.4 Results of Optimum Texture Shapes

In this section, the optimum texture shapes are obtained for a single unit cell on the surface of a ring specimen. Table 5-1 shows the basic input parameters used in the optimization. The geometrical parameters are selected based on the dimensions of the textured seal ring used in the experimental phase of this research. The textured surface is stationary while the runner surface is rotating in the counterclockwise direction.

A unit cell around the mid-radius of the seal ring is considered as the computational domain for the shape optimization. Since the simulations do not involve nonlinear phenomena, such as surface deformation, coupled thermal effects and large cavitation area, the optimum shape in the horizontal plane is not affected by the operating conditions (rotational speed, viscosity and minimum film thickness).

Table 5-1 The input parameters of the simulation

Parameter	Value
Inner radius r_i (mm)	21.5
Outer radius r_o (mm)	22.5
Minimum film thickness h_0 (μm)	10
Sector angle θ_0 (°)	3
Viscosity μ (Pa.s)	0.38
Ambient pressure p_0 (Pa)	1×10^5
Area ratio of texture	30%, 20%, 10%
Rotational speed ω (rpm)	400

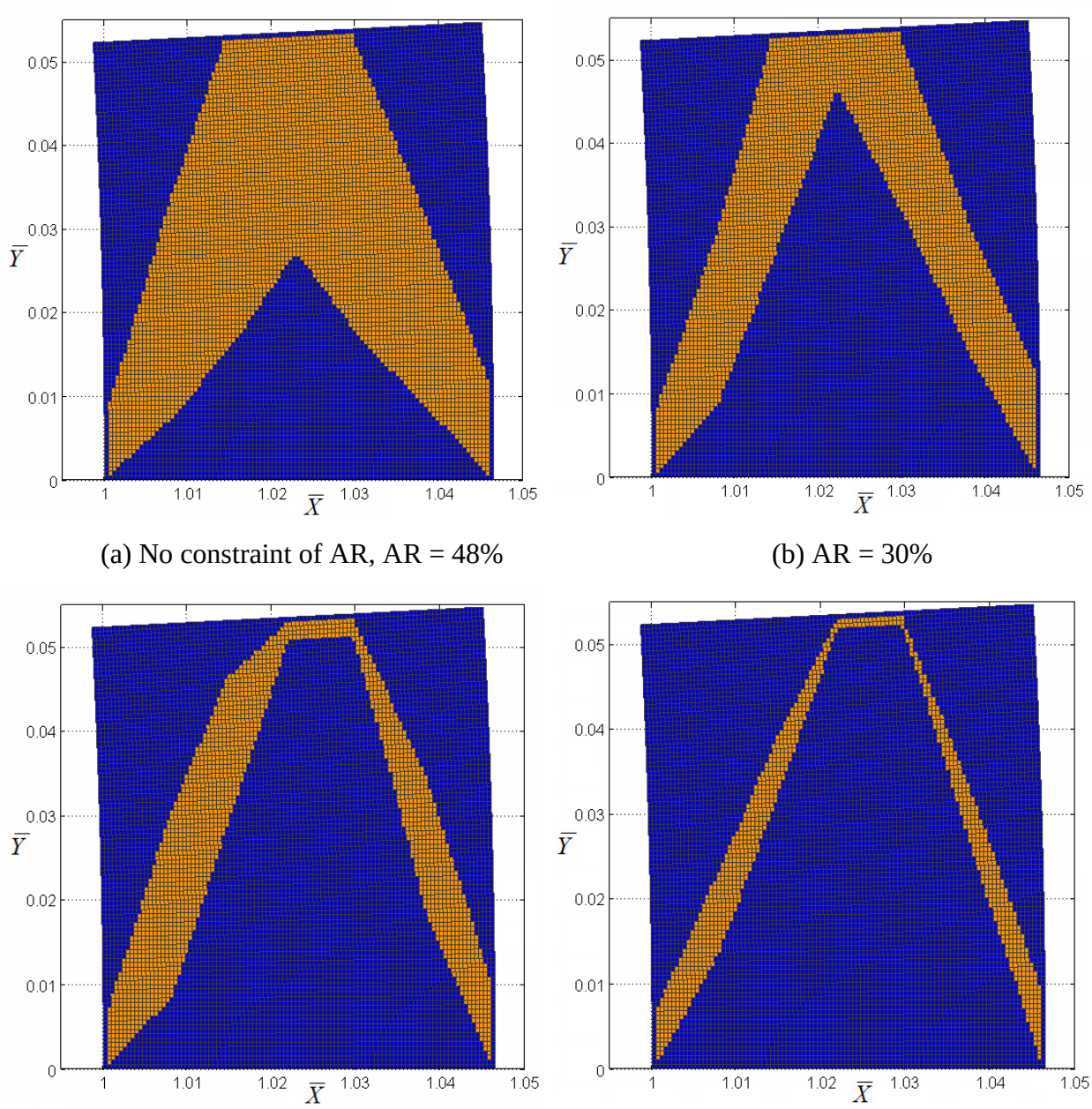

(a) No constraint of AR, AR = 48%

(b) AR = 30%

(c) AR = 20%

(d) AR = 10%

Figure 5-2 Optimum texture shapes for different area ratios

Four cases of constraints are considered for shape optimization in this study. The first case does not impose a constraint on the area ratio (AR); the area ratios of the three other cases are fixed at 30%, 20% and 10%. The area ratio is defined as the ratio of the textured area to the total surface area. It has a significant influence on the tribological performance of textured surfaces [6]. Optimal

area ratios in the range of 5-20% are reported by different theoretical and experimental studies [4-7, 12].

Figure 5-2 shows the optimum texture shapes obtained with different area ratios. The corresponding dimensionless design variables are listed in Table 5-2. It can be seen that the four optimum texture geometries have similar chevron-shapes with flat fronts. As the AR decreases, the groove widths of the optimum textures decreases; however, their general shapes do not change. The possible physical reasons that these shapes can generate the maximum load-carrying capacities are as follows. The chevron-like shape can help increase the formation of the hydrodynamic pressure due to its pumping-in effect with lateral flow restriction. And the flat front can increase the area of high-pressure region. As a result, the total load-carrying capacity is greatly enhanced by texture shapes with these two features. It needs to be noted that the optimization results in Table 5-2 are non-dimensional. Therefore, if the dimensions (sector angle and radius) of the unit cell are changed, the optimum shapes would change accordingly.

Table 5-2 Dimensionless design variables for texture shapes with different area ratios

$\overline{\theta}_1$	$\overline{L}_1$	$\overline{\theta}_2$	$\overline{L}_2$	$\overline{\theta}_3$	$\overline{L}_3$	$\overline{\theta}_4$	$\overline{L}_4$	$\overline{\theta}_5$	$\overline{L}_5$	$\overline{\theta}_6$	$\overline{L}_6$	$\overline{\theta}_7$	$\overline{L}_7$	$\overline{h}_g$
No constraint of area ratio														
0.09	0.16	0.38	0.48	0.65	0.68	0.75	0.48	0.65	0.68	0.38	0.44	0.11	0.20	1.72
Area Ratio = 30%														
0.08	0.14	0.36	0.38	0.76	0.46	0.93	0.12	0.78	0.42	0.41	0.30	0.12	0.22	1.95
Area Ratio = 20%														
0.07	0.12	0.36	0.40	0.72	0.30	0.97	0.04	0.97	0.04	0.50	0.32	0.10	0.18	2.13
Area Ratio = 10%														
0.07	0.12	0.35	0.18	0.68	0.12	0.98	0.02	0.98	0.02	0.52	0.14	0.09	0.16	2.58

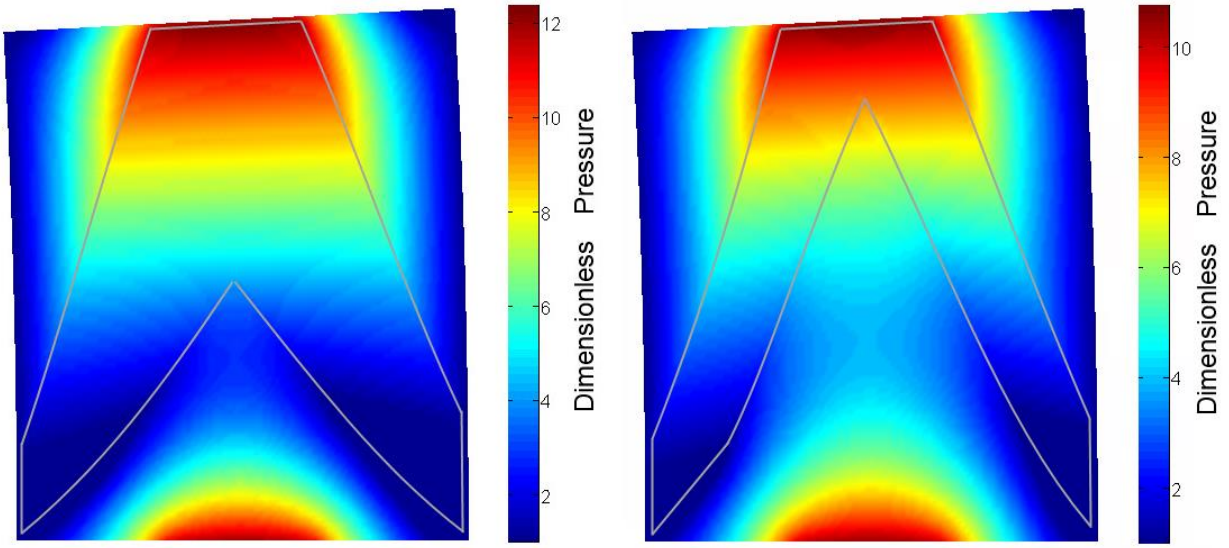

(a) No constraint of AR, $\overline{W}$ = 0.177 (b) AR = 30%, $\overline{W}$ = 0.162

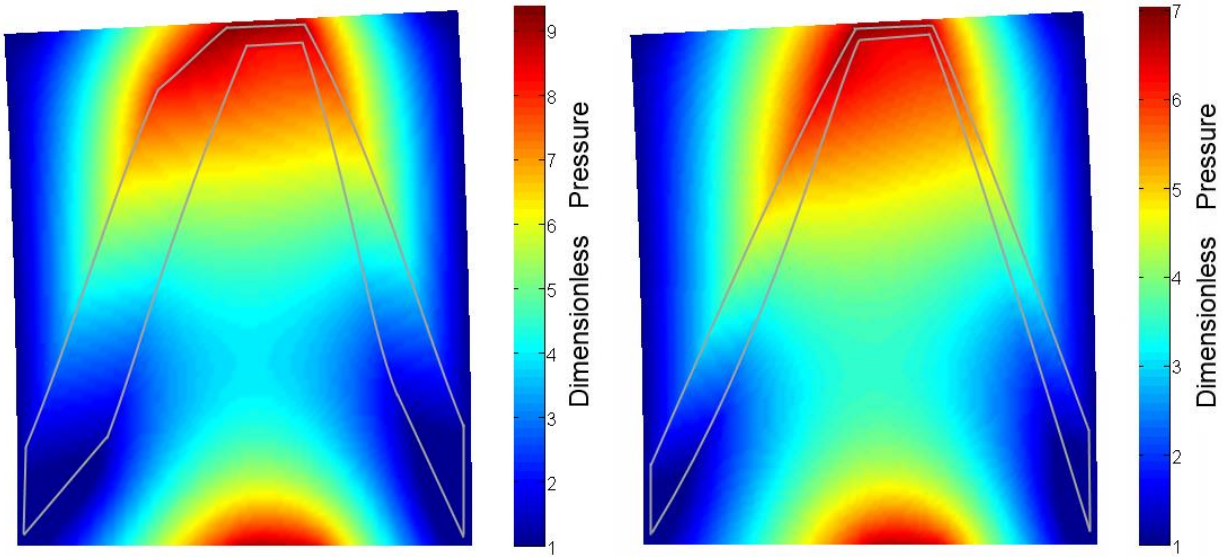

(c) AR = 20%, $\overline{W}$ = 0.147 (d) AR = 10%, $\overline{W}$ = 0.114

Figure 5-3 Pressure distributions of optimum texture shapes

Figure 5-3 shows the dimensionless hydrodynamic pressure distributions generated by the optimal texture shapes. Comparison of peak pressures and LCCs in the figure reveals that there is an optimum value for AR which maximizes the LCC. According to the optimization results without any constraint on AR, the optimum AR is 48% under the conditions simulated. Then as the AR

decreases the LCC of optimal texture shapes decreases. However, it should be noted that the optimum AR discussed here is only based on the LCC of textures under hydrodynamic lubrication. In tribological applications, to allow for the potential detrimental effects caused by surface texturing, such as reduction of the contact area and stress concentration, it is recommended to use an area ratio no greater than 20% [12]. Therefore, for the purpose of this study, the optimal shape with AR of 20% is used in the following experiments.

5.5 Experiment

The tribological performances of an optimum texture shape (AR = 20%) are evaluated by ring-on-ring friction tests under different operating conditions. The results are compared with those of regular shapes in order to validate the optimization results obtained in previous section.

5.5.1 Specimen Preparation

The upper specimen of the tests is a rotating ring with a smooth surface (roughness average Ra = 0.01 μm). Its inner diameter (I.D.) is 30.5 mm and outer diameter (O.D.) is 50.8 mm. Textures are fabricated on the surface of the stationary lower specimen. It is smaller in size with I.D. = 38.1 mm and O.D. = 48.3 mm. The upper and lower specimens are made of tungsten carbide and carbon graphite, respectively. Both materials are commonly used for the seal rings of mechanical seals.

A laser marking system (Electrox Inc.) is used to fabricate textures on the lower specimen surface. The design of textures is first generated with CAD software and then imported into the laser machine. The machine uses Nd:Ytterbium fiber laser to remove material from specimen surface and engrave the desired patterns. The depth of textures can be controlled by the number of times that laser scans the specimen surface.

Three regular texture shapes are considered for comparison with the optimal shape (AR = 20%) in this study. In order to concentrate on the effect of texture shapes, all the patterns are fabricated with the same area, distribution and texture depth. Theoretically, the size of the optimal texture should change in radial direction according to the non-dimensional optimization results in Section 5.3. However, since the sizes of the regular textures are fixed, the area of the optimal textures needs to be maintained the same for comparison purposes. The dimensions of optimal texture are calculated based on a unit cell around the mid-radius of the seal ring to minimize the deviation from the optimal size. Table 5-3 lists the geometrical parameters for textures used in the experiments. A total number of 480 patterns are fabricated on the surface of each ring specimen with 120 pattern columns with 4 patterns in each column. This distribution of the textures is chosen based on the dimensions of the ring specimen and the size of a single texture. The amplified images of textured specimens are shown in Figure 5-4. Since there is a distance of 0.25 mm between unit cells in radial direction, not all the surface area is used for texturing. The final area density of textures is 15.9%. Also, as the spacing is relatively small, there could be interactions between textures in radial direction. But since the spacing and distribution of all textures are the same, this should not affect the comparison between the optimal and regular textures.

After laser texturing, the lower specimens are lapped to achieve a surface roughness (Ra) of 0.04 μm for un-textured area. Measurements of the textured specimens show that laser texturing has sufficient precision for the current designs. The variation of texture size is always less than 5% of the design value and the depth variation is less than 2 μm for all specimens.

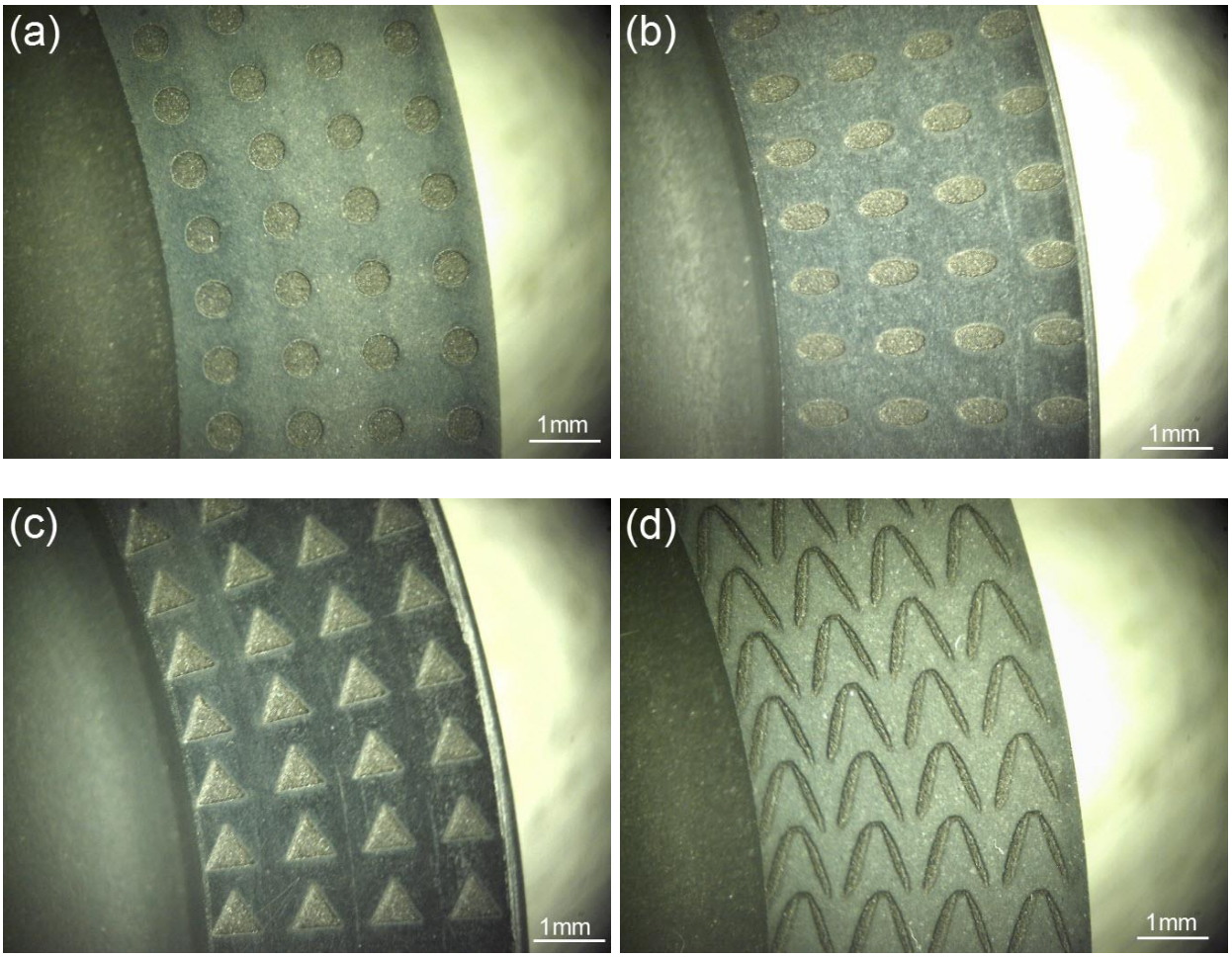

Figure 5-4 Images of textured specimens (a) circle, (b) ellipse, (c) triangle and (d) optimal

Table 5-3 Geometric parameters of the textures

Texture shape	Characteristic length (mm)	Area of a pattern (mm^2)	No. of patterns	Area density (%)	Depth (μm)
Circle	0.270 (radius)	0.229	480	15.9	11
Ellipse (a = 2b)	0.382/0.191 (radius)	0.229	480	15.9	11
Triangle	0.728 (side length)	0.229	480	15.9	11
Optimal	—	0.229	480	15.9	11

5.5.2 Test Apparatus and Procedure

The Lewis LRI-1a tribometer is used for the experimental testing in this study. Figure 5-5 shows the sketch of the experiment set up. The upper rotating specimen is driven by the spindle via the upper holder. The holder is equipped with a ball-joint mechanism which ensures that the surfaces of upper and lower specimens align automatically. The lower specimen is fixed on the inner seat of a lubricant cup. During the tests, both specimens are submerged in the lubricant in a cup as shown in Figure 5-5. The load is applied to the lower specimen through the lever arm. Its magnitude is monitored and controlled by a load cell attached to the loading system. The friction force is measured by another load cell connected to the tension bar.

The tribological test procedure is described as follows. First, the upper and lower specimens are installed in the tribometer. Then, the lubricant is filled into the cup until it reach the required level. Before any measurement is taken, all the specimens were subjected to a running-in period of 3 hours with a load of 80 N and a speed of 360 rpm. After completion of the running-in period, the friction tests are performed with a fixed load and varying speed. The loads of 100 N and 200 N are used in the tests. For a constant load, the rotational speed is decreased from 1000 rpm to 20 rpm in a stepwise manner. The test duration of each step is 3 minutes. The reported friction results correspond to stable data averaged over the last minute of each step. All the tests are conducted at room temperature (around 25°C). Purified water and Paratherm heat transfer oil are used as lubricants in this study. Their dynamic viscosities at room temperature are 8.9×10^{-4} and 6.4×10^{-3} Pa.s, respectively.

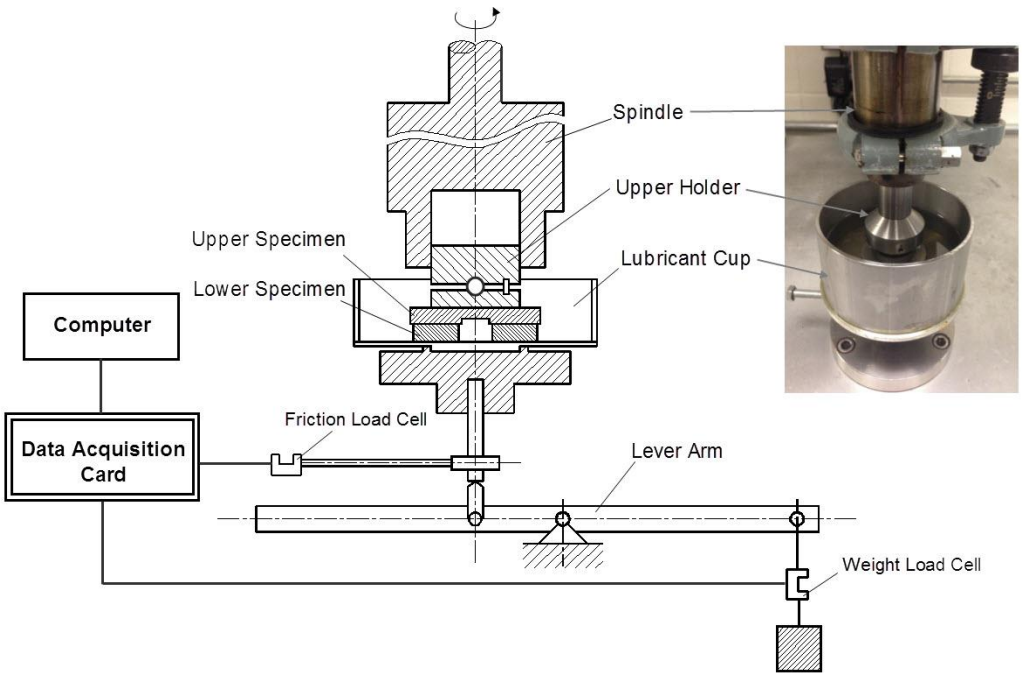

Figure 5-5 Schematic of the test rig

5.5.3 Results and Discussion

Figure 5-6 shows the relationship between friction coefficient and rotational speed for specimens with different texture shapes. As the rotational speed increases, the friction coefficients of all specimens show a similar trend. They first decreases from a high value to a low value and then slightly increase with increasing speed. This is consistent with the transition from mixed to hydrodynamic lubrication of the Stribeck curve. The lift-off speed of each specimen can be seen at the transition point which marks the watershed between the mixed and hydrodynamic lubrication regimes [26]. This usually occurs where the friction coefficient is the minimum.

Comparison of the test results with different specimens show that the texture shape has a major influence on the tribological performance of textured surface. As can be seen, under the conditions tested, the optimal texture shape has the lowest friction coefficient in the mixed lubrication regime while that of the triangular shape is the highest. Since all the specimens have identical surface

roughness and texture area density, the difference of the friction coefficients is due to the texture shape. Under the mixed lubrication, the total load is shared by both fluid film and asperity contact. The friction force also includes contribution from both of these components. Usually, the friction coefficient of asperity contact is much higher than that of full film lubrication. As a result, the higher the load-carrying capacity of a texture, the less is the load supported by asperity contact. Hence, the asperity contact contributes less to friction force resulting in a lower friction coefficient. This is the reason that optimal texture shape obtained from maximum load-carrying capacity is capable of producing low friction coefficient.

Another indication of the texture shape effect is the difference of lift-off speed (transition point). As shown in Figure 5-6, the lift-off speed for optimal texture shape is around 400 rpm while those for regular shapes are about 600 rpm. This means the optimal texture shape can help reach hydrodynamic lubrication regime with a lower speed.

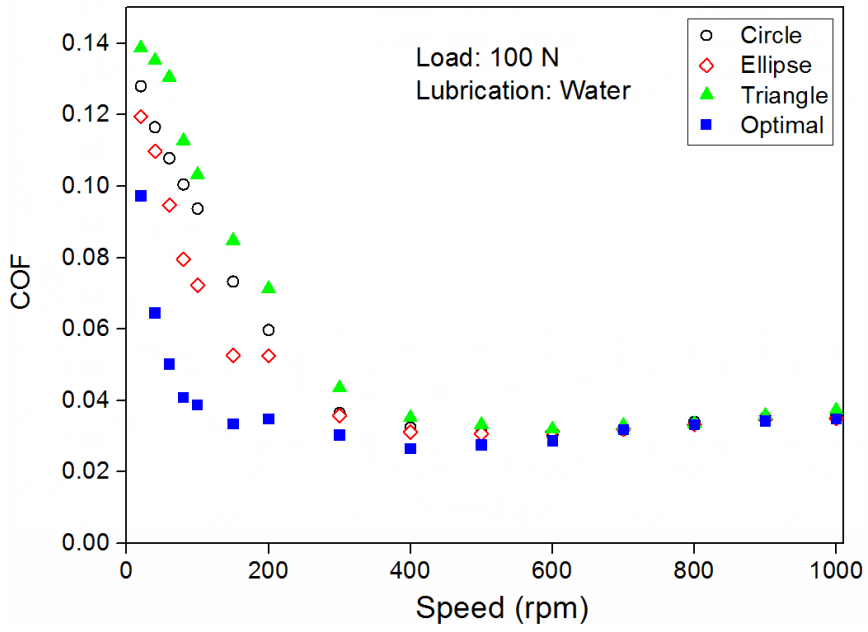

Figure 5-6 Variation of friction coefficient with speed under the load of 100N

Figure 5-7 demonstrates the test results for different specimens under the load of 200 N. It can be seen that the lift-off speeds of all specimens are shifted to the right (higher values) as the load is increased from 100 to 200 N. This shift can be explained by the hydrodynamic lubrication theory that a higher speed can generate more hydrodynamic pressure, which helps balance the increased load. Comparison of the test results shows that the optimal texture shape consistently perform better than the regular texture shapes in terms of lower friction coefficient. Also, the specimen with optimal textures presents a lower lift-off speed compared to those with regular textures.

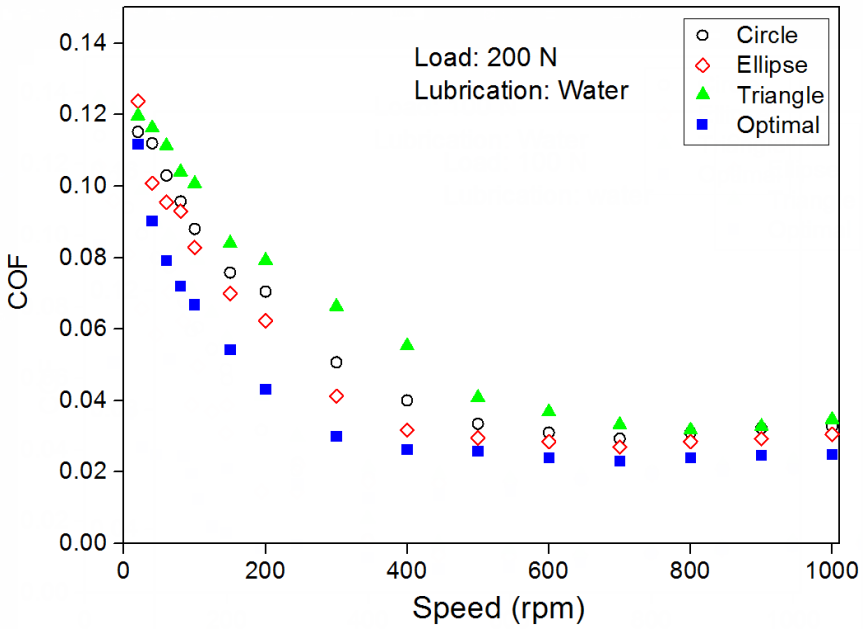

Figure 5-7 Variation of friction coefficient with speed under the load of 200N

Figure 5-8 shows the experimental results under lubrication of Paratherm oil, which has a viscosity six times higher than that of purified water at room temperature. As compared with Figure 5-7, a higher lubricant viscosity shifts the lift-off speed to the left (lower values). This agrees with the lubrication theory that hydrodynamic lift increases with increasing viscosity. Hence, in order to balance the same load, a lower speed is needed for a more viscous lubricant. Comparison of tribological behavior of the four textures indicates that the optimal shape has the lowest friction

coefficient for all rotational speeds. Even in the hydrodynamic lubrication regime the optimal texture still shows a clear advantage. A possible reason for that is the viscous shear force is high when lubricated with high-viscosity oil. The surface textures can affect the film thickness between seal rings and hence make a difference on the shear force and friction coefficient. But differences between the lift-off speeds become insignificant when lubricated with the high-viscosity oil.

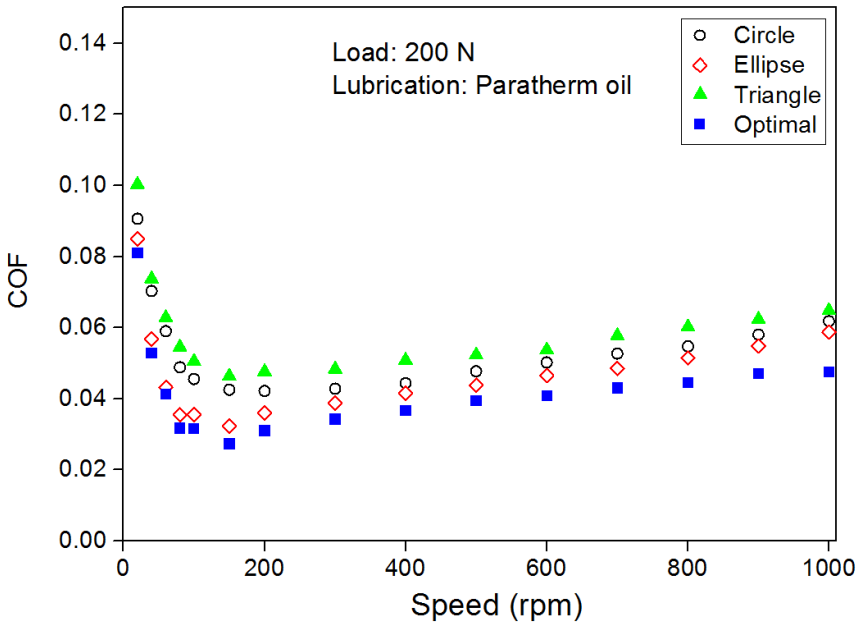

Figure 5-8 Relationship between friction coefficient and speed under lubrication of Paratherm oil

The above test results suggest that the optimal texture shape provides lower friction coefficient than the regular shapes under different operating conditions. It can also reduce the lift-off speed for full-film lubrication when lubricated with low-viscosity liquid. The reason for these results is thought to be that the optimal texture shape can generate more hydrodynamic lift. In the mixed lubrication regime, when the hydrodynamic lift is increased by the optimal shape, less asperity contact occurs. This leads to a reduction of the friction coefficient. In the hydrodynamic lubrication regime, the friction comes from viscous shear force, which is dependent on the film thickness and lubricant viscosity. Since the optimal texture shape can generate more lift, it will increase the film

thickness and hence reduces the friction. The tribological performance of optimal texture obtained in this study indicates that it is more efficient for hydrodynamic pressure generation than other regular shapes. This validates the optimization results in previous section. Numerical simulation of the above tests is not conducted in this work because it requires a comprehensive mixed-lubrication model with consideration of surface roughness, thermal effects, surface deformation and even consideration of the mechanisms of load-carrying capacity in parallel surfaces [27-29]. These considerations are beyond the scope of the current study. The interested readers can refer to reference [30], which presented a numerical study of textured mechanical face seals using mass-conservative algorithm and a deterministic Hertz contact model.

5.6 Conclusions

This study presents novel texture shapes for ring specimens, which generates the maximum LCC under different constraints. A numerical optimization approach based on the SQP algorithm is first applied for the texture shape optimization. The optimization results show that the general shape of optimum textures does not change with area ratio under the conditions simulated. They all have chevron shapes with flat fronts. But the width of texture groove decreases as the area ratio decreases. The optimization results are validated by a series of experiments. The tribological performances of optimum texture shape (AR = 20%) are evaluated under different test conditions and compared with those of regular shapes. It is shown that the optimal texture shape has superior performance than regular shapes in terms of lower friction coefficient and lower lift-off speed. The reason for the performance enhancement is that the optimal texture shape is more efficient for hydrodynamic pressure build-up.

5.7 References

[1] Xiao N., Zhang Q., Ligrani P. M., Mongia, R., 2009, "Thermal Performance of Dimpled Surfaces in Laminar Flows," Int. J. Heat Mass Transf., 52, pp. 2009–2017.

[2] Xiao N., Khonsari M.M., 2012, "Thermal performance of mechanical seals with textured side-wall," Tribol. Int., 45, pp. 1-7.

[3] Etsion I., 2004, "Improving tribological performance of mechanical components by laser surface texturing," Tribol. Lett., 17, pp. 733–737.

[4] Etsion, I., Kligerman Y., 1999, "Analytical and experimental investigation of laser-textured mechanical seal faces," Tribol. Trans., 42(3), pp. 511–516.

[5] Wang X., Kato K., Adachi K., Aizawa K., 2003, " Loads carrying capacity map for the surface texture design of SiC thrust bearing sliding in water," Tribol. Int., 36, pp. 189–97.

[6] Yan D., Qu N., Li H., Wang X., 2010, Significance of dimple parameters on the friction of sliding surfaces investigated by orthogonal experiments. Tribol. Trans., 53, pp. 703-712.

[7] Kovalchenko A., Ajayi O., Erdemir A., Fenske G., Etsion I., 2005, "The effect of laser surface texturing on transitions in lubrication regimes during unidirectional sliding contact," Tribol. Int., 38, pp. 219-225.

[8] N. Talalghil, M. Fillon, P. Maspeyrot, 2011, "Effect of textured area on the performances of a hydrodynamic journal bearing," Tribol. Int., 44, pp. 211-219.

[9] Qiu, Y., Khonsari M.M., 2011, "Performance analysis of full-film textured surfaces with consideration of roughness effects", ASME J. Tribol., 133, pp. 021704:1-10.

[10] Qiu, Y., Khonsari M.M., 2011, "Experimental investigation of tribological performance of laser textured stainless steel rings", Tribol. Int., 44, pp. 635-644.

[11] Shen C., Khonsari M. M., 2013, "Effect of dimple's internal structure on hydrodynamic lubrication", Tribol. Lett., 52, pp. 415–430.

[12] Wang, X., Wang, J., Zhang, B., Huang W., 2014, "Design principles for the area density of dimple patterns", Proc. IMechE. Part J: J. Engineering Tribology, 229, pp. 538-546.

[13] Ibatan T., Uddin M.S., Chowdhury M.A.K, 2015, "Recent development on surface texturing in enhancing tribological performance of bearing sliders", Surface & Coatings Technology, 272, pp.102-120.

[14] Lu, X., Khonsari, M.M., 2007, “An experimental investigation of dimple effect on the stribeck curve of journal bearings”, Tribol. Lett., 27, pp. 169–176.

[15] Galda L., Pawlus P., Sep J., 2009, “Dimples shape and distribution effect on characteristics of Stribeck curve”, Tribol. Int., 42, pp.1505–1512.

[16] Yu, H., Wang, X., Zhou, F., 2010, “Geometric shape effects of surface texture on the generation of hydrodynamic pressure between conformal contacting surfaces”, Tribol. Lett., 37, pp.123-130.

[17] Zhang, J., Meng, Y., 2012, “Optimal design of surface texture in parallel thrust bearings”, Journal of Mechanical Engineering, 48(17), pp. 91-99.

[18] Rahmani R, Shirvani A, Shirvani H., 2007, “Optimization of partially textured parallel thrust bearings with square-shaped micro-dimples”, Tribol. Trans., 50, pp. 401-406

[19] Qiu M, Delic A, Raeymaekers B, 2012, “The effect of texture shape on the load carrying capacity of gas lubricated parallel slider bearings”, Tribol. Lett., 48(3), pp. 315-328

[20] Qiu M, Minson B, Raeymaekers B, 2013, “The effect of texture shape on the friction coefficient and stiffness of gas lubricated parallel slider bearings”, Tribol. Int., 67, pp. 278-288.

[21] Shen C., Khonsari M. M., 2015, “Numerical optimization of texture shape for parallel surfaces under unidirectional and bidirectional sliding”, Tribol. Int., 82, pp.1–11.

[22] Fesanghary M., Khonsari M.M., 2013, “On the optimum groove shapes for load-carrying capacity enhancement in parallel flat surface bearings: theory and experiment”, Tribol. Int., 67, pp. 254 – 262.

[23] Thorson J., 1979, “Gaussian elimination on a banded matrix”, Stanford University, (Stanford Exploration Project).

[24] Qiu, Y., Khonsari, M. M., 2009, “On the prediction of cavitation in dimples using a mass-conservative algorithm”, ASME J. Tribol., 131, pp. 041702:1-11.

[25] Spellucci P., 1998, “An SQP method for general nonlinear programs using only equality constrained subproblems”, Mathematical Programming, 82 (3), pp. 413–48.

[26] Lu, X., Khonsari, M.M., 2005, “On the lift-off speed in journal bearings”, Tribol. Lett., 20, pp. 299–305.

[27] Lebeck, A. O., 1987, “Parallel sliding load support in the mixed friction regime, Part 1: the experimental data,” ASME J. Tribol., 109, pp. 189−195.

[28] Lebeck, A. O., 1987, “Parallel sliding load support in the mixed friction regime, Part 2: evaluation of the mechanisms,” ASME J. Tribol., 109, pp. 196−205.

[29] Yang, P., Kaneta, M., 2013, “Thermal wedge in lubrication,” Encyclopedia of Tribology, Springer, New York, pp. 3617−3622.

[30] Brunetiere, N., Tournerie, B. 2012, “Numerical analysis of a surface-textured mechanical seal operating in mixed lubrication regime,” Tribol. Int., 49, pp. 80-89.

CHAPTER 6 THE EFFECT OF LASER MACHINED POCKETS ON THE LUBRICATION OF PISTON RING PROTOTYPES [4]

6.1 Nomenclature

B Unit cell width (m)

h Local film thickness (m)

h_0 Minimum film thickness (m)

h_g Pocket depth (m)

$\bar{h}$ Dimensionless local film thickness, h/h_0

$\bar{h}_g$ Dimensionless pocket depth, h_g/h_0

L Unit cell length (m)

p Local Pressure (Pa)

p_0 Ambient pressure (Pa)

p_c Cavitation Pressure (Pa)

$\bar{p}$ Dimensionless pressure, p/p_0

U Sliding speed (m/s)

$\overline{W}$ Dimensionless load-carrying capacity

θ Fluid fraction variable

[4] This chapter previously appeared as Shen C., Khonsari M. M., "The effect of laser machined pockets on the lubrication of piston ring prototypes", Tribology International, 101(2016), pp. 273-283.. It is reprinted by permission of Elsevier.

μ Lubricant viscosity (Pa.s)

κ Dimensionless curvature of piston ring, δ / h_0

Λ Characteristic number, $6\mu UL / p_0 h_0^2$

6.2 Introduction

The stringent requirements on fuel efficiency, emission and durability of the internal combustion (IC) engines have led to a growing interest in reducing engine frictional losses. According to references [1-3], the piston ring/cylinder liner contact is one of the major sources of friction that accounts for approximately 40% of the total mechanical loss. In recent years, a significant volume of research efforts has been dedicated to the friction reduction of piston/cylinder system, which has already yielded a wide variety of solutions including low-friction hard coatings [4-5], surfaces with modified topology [6-11], and lubricants with nanoparticles [12]. Among these techniques, surface texturing has emerged as a promising method for the industrial application. This approach essentially modifies the surface topology in a controlled manner by producing specific surface structures (dimples, grooves or asperities) that benefit lubricated contacts. One example of surface texturing that has been widely applied in the piston ring/cylinder liner (PRCL) contact is the honing of the inner surface of a cylinder liner. The surface patterns created by the honing process are cross-hatched grooves that are deeper than surface roughness. These grooves have proven to be effective in enhancing the lubrication characteristics and even prevent scuffing.

In the last two decades, various texture manufacturing techniques have been developed to enable fabrication of micro surface features with high accuracy and good controllability. Laser surface texturing that uses laser ablation to remove material from the surface is one of the most common methods. Etsion and his colleagues have conducted a series of studies to investigate the effect of

laser textured surface on the reciprocating PRCL contact. Ronen et al. [6] developed a numerical model for the lubrication between flat piston rings textured with spherical micro-pores and cylinder liners. Their analysis shows that pores with optimum geometries can result in significant friction reduction (30% or even more). This effect was confirmed by an experimental study of Ryk et al [7]. Later, they proposed partial laser surface texturing for piston rings, which creates circular dimples that are partially distributed on the contact surface and are able to generate "collective dimple effect" (strong interaction between neighboring dimples). This effect can result in a step-like pressure distribution over the textured region. Ryk et al [8, 9] evaluated the effect of optimum partial surface textures obtained by Kligerman [10] using a reciprocating test rig. Their experimental results show that flat piston rings with partial surface texturing can lead to a friction reduction of up to 25% comparing with both fully textured and barrel-shaped non-textured piston rings. More recently, Etsion and Sher [11] compared the performance of partially textured flat ring and conventional barrel-shaped ring using dynamometer tests on an IC engine. They found that the partially textured piston ring exhibited a reduction of up to 4% in fuel consumption depending on the engine load. Bolander and Sadeghi [13] also investigated the influence of surface texturing on the friction at PRCL interface using a specially designed test rig and specimens made of segments of production piston ring and cylinder liner. They concluded that frictional performance of the piston ring can be improved by shallow dimples while deep dimples (10 μm) have detrimental effects. Other recent work have dealt with laser surface texturing of barrel-shaped ring, oil control ring and non-spherical dimples. Gadeschi et al. [14] conducted numerical simulations to investigate the performance of fully and partially textured piston rings with various surface curvatures. Under the conditions simulated, it is found that partial surface texturing with a central dimple distribution has a significant friction reduction effect on the barrel-shaped rings.

Tomanik [15] developed a mixed lubrication model to simulate the effect of surface texturing on PRCL interface. They concluded that significant hydrodynamic support can be generated by the micro-dimples, which can help to reduce friction and wear, especially for the flat surface of oil control rings. Zavos et.al [16] compared effects of spherical and rectangular dimples on the tribological performance of flat compression rings using computational fluid dynamics. Their analyses show that the rectangular dimples with depth of 4 μm, texture density of 61% and aspect ratio of 20 resulted in the best friction reduction.

In the above studies, surface texturing was applied to the outer surface of piston rings. The same technique can also be employed to treat the inner surface of cylinder liners for reducing friction at PRCL interface. Tomanik [17] performed friction and wear tests on cylinder liners with different surface finishes (plateau honing and laser texturing) using a reciprocating tester. But their results show that liners after conventional honing have less friction than those textured with grooves of 1mm- and 3mm- length. Grabon et al. [18] used impulsive burnishing to create micro dimples on the liner surface after plateau honing and experimentally investigated its effect on the tribological behavior. They observed that the cylinder liner surface texturing significantly reduced the friction at PRCL contact and that its effect is more substantial under fully lubricated conditions. The details of the burnishing technique that allows the fabrication of dimples with various sizes and distribution on the inner surface of a cylinder liner can be found in reference [19].

Some theoretical studies are also conducted on the effect of textured liner surface. Yin et al. [20] developed a mixed lubrication model for the contact between flat piston ring and cylinder liner textured with dimples. It is found that the textured liner surface can help generate effective hydrodynamic lubrication during most of the stroke except near the dead centers. Mezghani et al. [21] investigated the effects of the groove textures on the frictional performance of the PRCL

contact with a hydrodynamic lubrication model considering lubricant film rupture and cavitation. The optimal groove texture characteristics, such as cross-hatch angle, groove width and density, were obtained to reduce the friction at the interface. Checo et al. [22] used a mass-conservative cavitation model for numerical simulations of the PRCL contact with textures on the liner. Their results show that the beneficial effect of textured cylinder liner is dependent on the ring profile. As the ring curvature increases, the PRCL contact becomes more conformal and the obtained friction reduction increases. In a very recent research, Morris et al. [23] presented a numerical study on the effect of surface texturing of the liner surface during reversals, where momentary cessation of motion and friction peak occur. Their analysis suggests that only a marginal reduction in friction can be obtained by adding shallow chevron features around the top dead centers.

In this paper, a new design of surface modification is proposed for the PRCL interface. It involves using a laser to engrave appropriately shaped and distributed pockets on the piston ring to improve lubrication performance and reduce friction. Then, the pocketed piston ring specimens were prepared and friction tests were conducted on a tribometer equipped with a reciprocating drive. The effect of pocket geometries on the tribological behavior of PRCL contact was investigated by a series of experiments. After that, a preliminary numerical model, which implements mass-conserving algorithm for cavitation, was used to analyze the relationship between pocket geometric parameters and the performances of pocketed rings.

6.3 Design of Pocketed Piston Ring

Figure 6-1 illustrates a piston ring with micro pockets on its outer surface. These pockets are distributed evenly on the two sides of the surface and one of their boundaries coincides with the edges of the ring so that the lubricant can flow directly into the pockets. During the reciprocating motion, although the sliding direction changes, the pockets on one of the two sides will always

function as tiny step bearings and thus generate hydrodynamic pressure to improve the lubrication. Moreover, the pockets could also act as oil reservoir and supply lubricant in cases of starved lubrication, especially during the reversals of the reciprocating motion. The distribution of the pockets is staggered on two sides in order to reduce the possible interaction of the pockets in the sliding direction and minimize its effect on the blow-by past the ring when it is implemented in an actual engine. By optimizing the geometric parameters, such as size, depth and shape, it is possible to maximize the beneficial effect of the pockets on the piston ring lubrication.

Compared with the texturing of dimples, the fabrication of pockets using a laser is less demanding because their sizes are larger and the total number of patterns is less. This leads to a lower requirement on the precision of machining and positioning for the pockets. Moreover, the performance enhancement mechanisms are different for the two types of surface modifications. Dimpled ring forms a diverging-converging geometry within each dimple. The lubricant film cavitates in the diverging region, which results in an asymmetric pressure distribution within the dimple and a net force that gives load-carrying capacity. In pocketed rings, the pockets at the leading edge form converging step shapes in the ring profile to generate hydrodynamic pressure, akin to step bearings that accommodate pressure build-up.

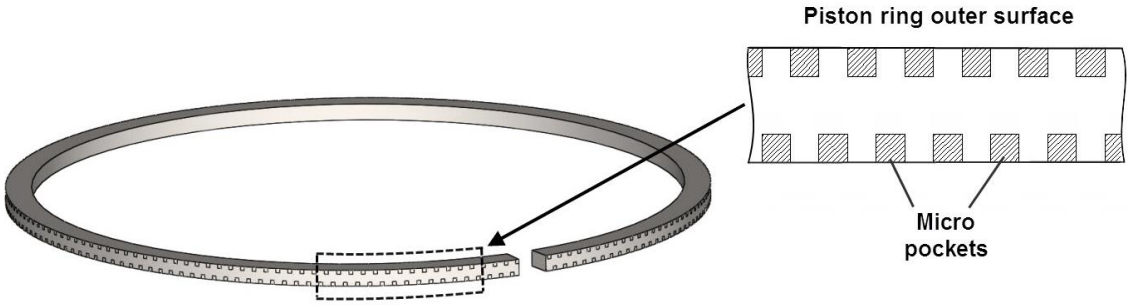

Figure 6-1 Schematic of pocketed piston ring surface

In the following sections, the results of both experimental and numerical analyses are reported to investigate the influence of the pocket geometry on the tribological performance of piston ring prototype. It needs to be mentioned that only idealized flat piston rings are considered in this study, wherein their plane surfaces are parallel to the cylinder liner. Also, the width of specimen surface in the experiments is larger than those of regular piston rings so that relatively large pockets can be created on the contact surface and the effect of the pockets can be easily measured. For applications of the pockets in real piston rings, the pocket dimensions need to be reduced according to the ring width.

6.4 Experiment

6.4.1 Test Rig

The experimental tests were carried out on a tribometer (CETR UMT-3) equipped with an instrumented reciprocating drive to simulate the contact between the piston ring and cylinder liner. Figure 6-2 shows the schematic and a picture of the test rig. An adjustable crank mechanism converts the rotational motion of electric motor into the reciprocating motion of the stage, resulting in stroke lengths that vary up to 25 mm. The displacement of the stage is measured by a linear positioning sensor with a resolution of 5 μm.

The lower specimen is fixed on the inner seat of a lubricant container and driven by the reciprocating stage. During the tests, the specimens are submerged in the lubricant container. The load is applied to the upper specimen via a ball-joint holder, which ensures that the contact surfaces align automatically. High precision lateral and normal force sensors in the apparatus allow simultaneous measurement of the friction and normal forces (with a resolution of 0.05 N). All the

test data are recorded and stored in a computer via a data acquisition system with a maximum sampling rate of 1 kHz.

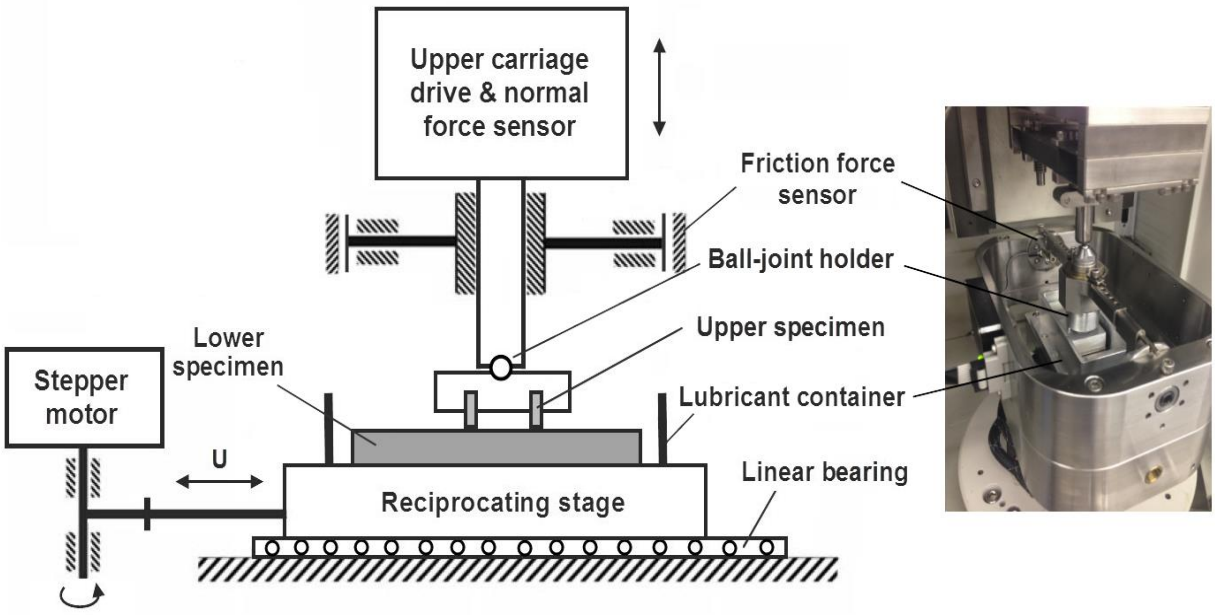

Figure 6-2 A schematic and photo of the test rig

6.4.2 Specimens

The experiments use upper specimens made of low-carbon steel to replicate the segments of flat piston rings and lower specimens made of cast iron to simulate the cylinder liner. Two "piston ring" specimens, with a width of 4 mm and length of 20 mm, are fixed in the specially designed ball-joint holder, as shown in Figure 6-2. The pockets are fabricated on their contact surfaces. The lower specimen is a reciprocating plane plate, with a width of 30 mm and length of 70 mm. Its top surface is ground to a surface roughness (Ra) of 0.5 μm. Figure 6-3 shows the photos of the upper and lower specimens.

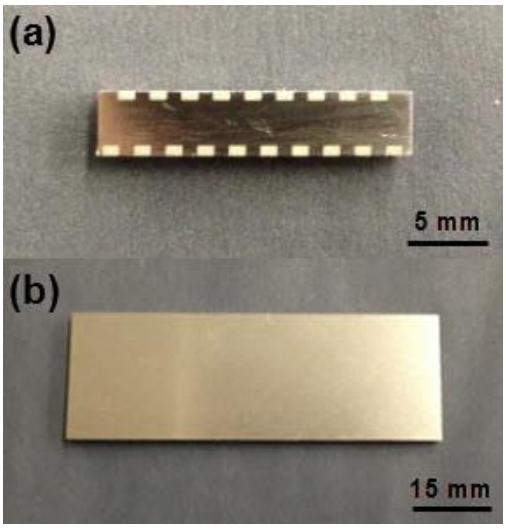

Figure 6-3 Test specimens: (a) upper specimen with pockets; (b) lower specimen of flat plate

The pockets on the specimen surface were machined by a laser device (Electrox Inc.) that uses Nd:Ytterbium fiber laser to remove materials. The design of pockets (shape and distribution) is first generated with a CAD software and then imported into the laser machine to engrave desired patterns. The pocket depth is controlled by the number of times that laser scans the specimen surface. Some performance parameter selected for the laser machining are: frequency of 12 kHz, wavelength of 1064 nm and average power of 10 W.

Pockets with various sizes and shapes were prepared and tested in this study. Tables 6-1 and 6-2 list the geometrical parameters of pockets used in the experiments. Note that the specimen R6 has a smooth surface without pockets, prepared for comparison purposes only. The pocket geometries can be divided into three groups: Group 1 (R1-R3 with various pocket lengths or area ratios), Group 2 (R2, R4, R5 with various depths) and Group 3 (R2, E1, T1 with various pocket shapes). The spacing and distribution of the pockets are kept the same for all specimens. After laser machining, the upper specimens were lapped to achieve a surface roughness (Ra) of 0.1 μm for un-textured area. The surface inside the pocket has an average roughness around 0.3 μm. Figure 6-4 shows the amplified images of the pocketed specimen surfaces.

Table 6-1 Geometric parameters of rectangular pockets

No.	Pocket length (mm)	Pocket width (mm)	Pocket spacing (mm)	Area ratio (%)	Depth (μm)
R1	0.5	1.0	2.0	12.5	5.2
R2	1.0	1.0	2.0	25.0	5.3
R3	1.5	1.0	2.0	37.5	5.3
R4	1.0	1.0	2.0	25.0	11.8
R5	1.0	1.0	2.0	25.0	25.6
R6	0.0	0.0	0.0	0.0	0.0

Table 6-2 Geometric parameters of the semi-elliptical and trapezoidal pockets

No.	Texture shape	Characteristic length (mm)	Pocket spacing (mm)	Area ratio (%)	Depth (μm)
E1	Semi-ellipse	Radius $a = 1.27$; $b = 0.50$	2.0	25.0	5.2
T1	Trapezoid	Side length $a = 1.0$; $b = 0.60$ $h = 1.25$	2.0	25.0	5.2

6.4.3 Test Procedure

Reciprocating friction tests were conducted with a stroke length of 25 mm under full lubrication conditions. An additive-free SAE 10 oil with a dynamic viscosity of 0.06 Pa.s at room temperature was used in the tests. The experimental procedure is described as follows. First, the “piston ring” and flat plate specimens were installed in the tribometer and fresh oil with a volume of 3 ml was supplied to the container. This volume is adequate for fully-flooded lubrication. After a running-in process of 20 minutes, the friction tests were performed under various load and speed conditions. The test rig was programmed so that a sequence of multiple tests can be executed automatically. In each test sequence, the load was fixed while the rotational speed of the crank was changed from 240 to 15 rpm in a stepwise manner. The test period of each step was 3 minutes, and there was a

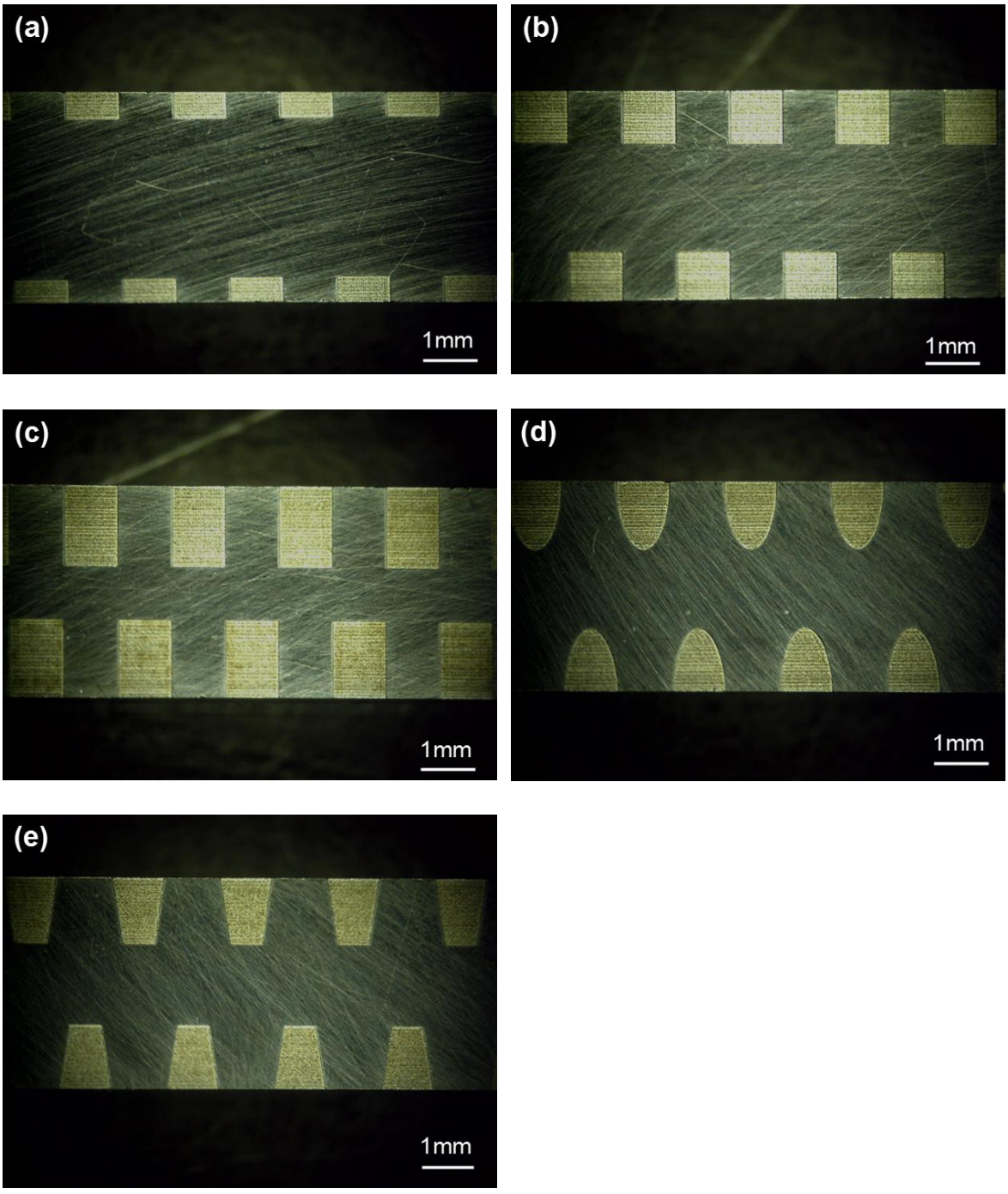

Figure 6-4 Images of pocketed specimens: (a) rectangular pocket R1; (b) square pocket R2; (c) rectangular pocket R3; (d) semielliptical pocket E1; (e) trapezoidal pocket T1

two-minute rest period between consecutive steps to minimize the possible temperature rise. All the tests were conducted at room temperature (around 25°C). The loads of 40 and 80 N were applied in the tests, which resulted in nominal contact pressures of 0.25 and 0.5 MPa, respectively.

The average coefficient of friction (COF) is used to represent the test result of each load-speed condition. It is calculated by averaging the absolute values of the friction coefficients over 40 reciprocating cycles in each test step.

6.4.4 Experimental Results

6.4.4.1 Effect of Area Ratio

The pocket's area ratio (AR) is defined as the ratio of the pocketed area to the total surface area. Figure 6-5 shows the frictional performance of the specimens with different pocket area ratios (R1, R2 and R3) as well as that of the specimen with plain surface. The pocketed specimens have the same pocket depth and width, but their pocket area ratios are varied from 12.5% to 37.5%. The results presented in Figure 6-5 show a persistent decrease in COF with increasing the rotational speed of the crank. Comparing with the plain surface, the specimens with pocket area ratios of 12.5% and 25% have lower average friction coefficients at relatively high speeds (greater than 60 rpm). For example, under the rotational speed of 180 rpm and load of 40 N, the specimen with a pocket area ratio (AR) of 25% shows a friction reduction of 52%. For both of the loading conditions, pockets with the AR of 25% presents consistently better performance than others at high speeds, while the specimen with AR of 37.5% has the highest COF under most of the testing conditions. The results show that the pocket area ratio has a major influence on the frictional behavior of the "piston ring" specimen and a high AR of 37.5% is not beneficial for lowering the COF. This agrees with findings of Wang et al. [24] who pointed out that a high dimple density usually caused an increase in the friction of textured surface. In addition, the test results reveal that the difference between the specimens at the load of 40 N is more pronounced than that at a higher load of 80 N. This implies the friction reduction effect of the pockets becomes less significant under higher applied loads.

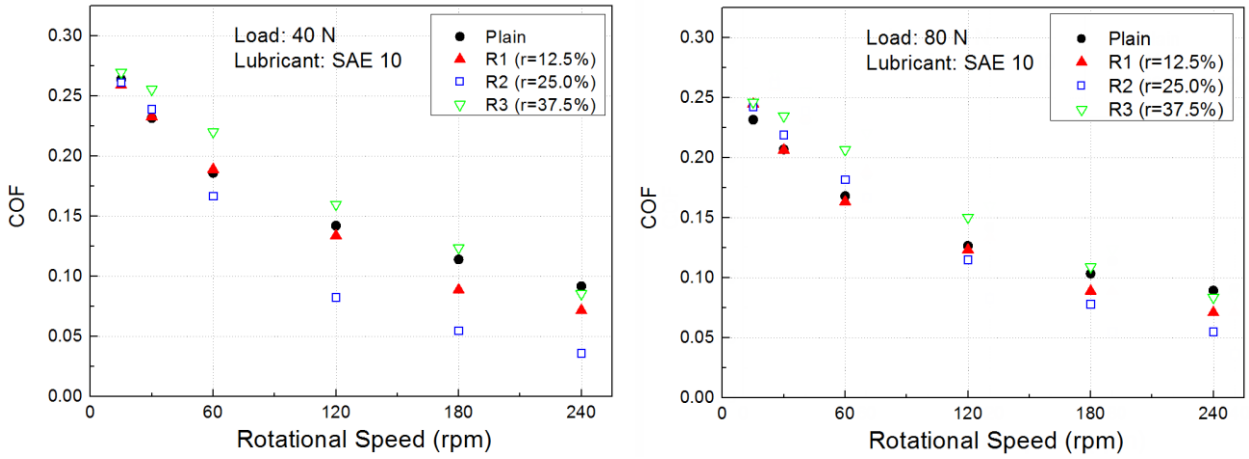

Figure 6-5 The effect of pocket area ratio on the frictional performance

The high value of COF at low speeds and the declining trend of COF with increasing speed suggest that under the conditions tested these specimens operate in the mixed lubrication (ML) regime. In ML the applied load is shared by the asperity contacts and fluid film. Accordingly, both of these components contribute to the friction force. At low speed, the load is mostly supported by the contact of asperities and the asperity-to-asperity contact portion of the friction is dominant in the overall COF. As the speed increases, the hydrodynamic action of the lubricant becomes more dominant and the fluid film portion contributes more to the load-carrying capacity. As a result, the COF decreases. Furthermore, as can be seen in Figure 6-5, the friction reduction effect of the pockets is more obvious at relatively high speeds (120 – 240 rpm). It is because these pockets work as tiny step bearings and generate additional hydrodynamic pressure, and their load-carrying capacities increase with the speed. As a result, less load is supported by asperity contacts at high speeds, which leads to a higher friction reduction. However, although the pockets can help to improve lubrication, they could also have negative effects similar to those of surface textures, e.g. stress concentration around the rim of the pockets with “cutting edge” effect [24-26]. When the pocket area ratio is high, the detrimental effects could have more influence and cause friction

increase. This is a possible reason for the high COF of the specimen with pocket area ratio of 37.5%.

Figure 6-6 depicts the friction force variation of all specimens over two complete cycles (four strokes). The friction force exhibits a similar trend. Two "friction spikes" at the beginning and end of the reciprocating strokes (top and bottom dead centers) and minimum values around the mid-stroke are typically observed. These trends are due to the variation of the sliding velocity generated by the crank mechanism. As the crank rotates, the sliding velocity increases to a maximum from the top dead center (TDC) to the mid-stroke and then decreases towards the bottom dead center (BDC). Since the specimens operate in the mixed lubrication regime, the higher the sliding velocity, the greater is the hydrodynamic lift and the lower the friction becomes. Therefore, the lowest friction occurs around the mid-stroke, where the magnitude of the sliding velocity is the highest. This trend of friction variation over the entire stroke agrees with the test results using segments of production piston ring and cylinder liner [27]. It is worthwhile to mention that comparing with the plain surface, the specimen with AR of 25% shows a consistently lower friction over the full stroke, especially around the top and bottom dead centers where the friction force reaches its maximum values. As shown in the magnified section of Figure 6-6, the magnitude of the peak friction is greatly reduced by the pockets with AR of 25%. This could be a major source of friction reduction at PRCL interface, because the peak friction occurs twice at every stroke and accumulates over time. There are two possible reasons for the reduced friction spikes associated with the pocketed specimen. One factor is that the pockets can provide additional load-carrying support and increase the maximum film thickness at high speeds (around the mid-stroke). This helps improve the squeeze film lubrication around the dead centers when the film thickness is decreasing due to the low sliding velocity. Another reason can be attributed to the benefits of oil-reservoir associated

with the pockets, which help to supply oil between the surfaces to reduce asperity contacts at low speeds.

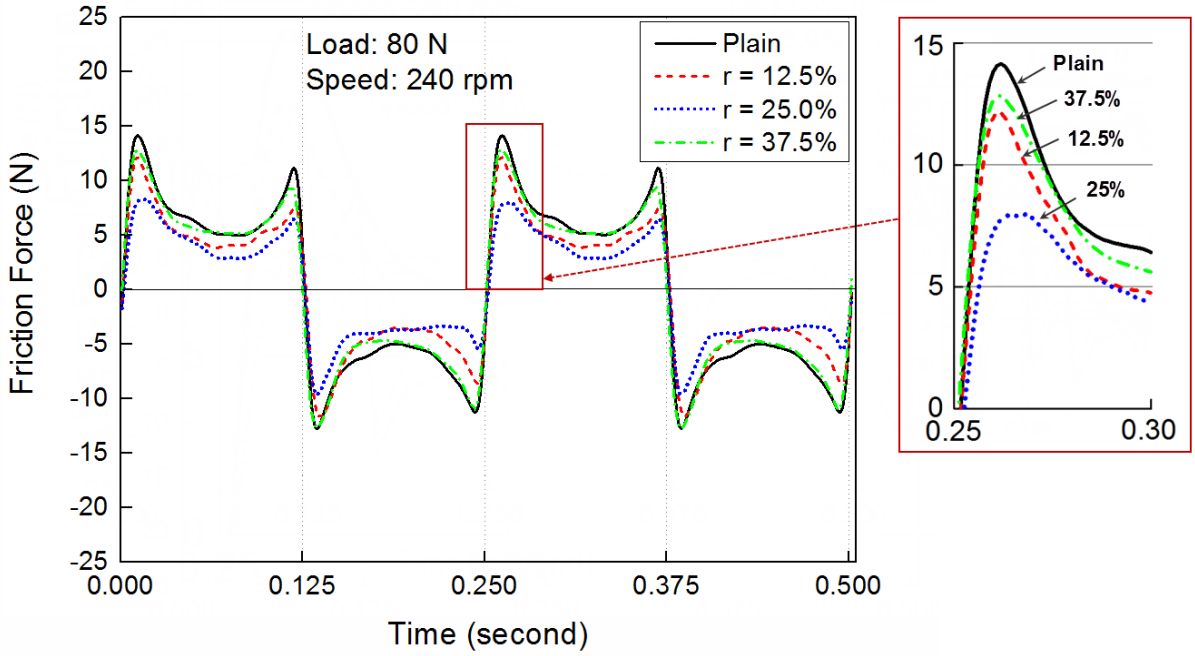

Figure 6-6 Friction force comparison between specimens with different pocket area ratios

6.4.4.2 Effect of Pocket Depth

Figure 6-7 illustrates the effect of pocket depth on the average friction coefficient operating under different loads and rotational speeds. The specimens (R2, R4 and R5) have an identical area ratio of 25%, which performs the best in the tests presented in the previous section. Their pocket depths are varied from 5.3 to 25.6 µm. The results show that, under the conditions tested, the specimen with pocket depth of 5.3 µm has the lowest overall COF, while the specimen with pocket depth of 25.6 µm exhibits the highest COF. In addition, the friction coefficient of deep pockets is consistently higher than that of the plain surface specimen, even under relatively high-speed conditions. This indicates that the pocket depth plays an important role in the tribological performance of the pocketed surfaces and that deep pockets do not improve the frictional

characteristics. In fact, their performance in terms of friction coefficient is inferior to plane surfaces. The reason for these results is thought to be related to the hydrodynamic lubrication of the pockets, which work similar to the step bearings. According to the Rayleigh step bearing theory, if the ratio between step height and lubricant film thickness is too high, the step bearing can hardly generate any load-carrying capacity [28]. Hence, deep pockets in this study cannot produce additional hydrodynamic pressure and yield higher COF.

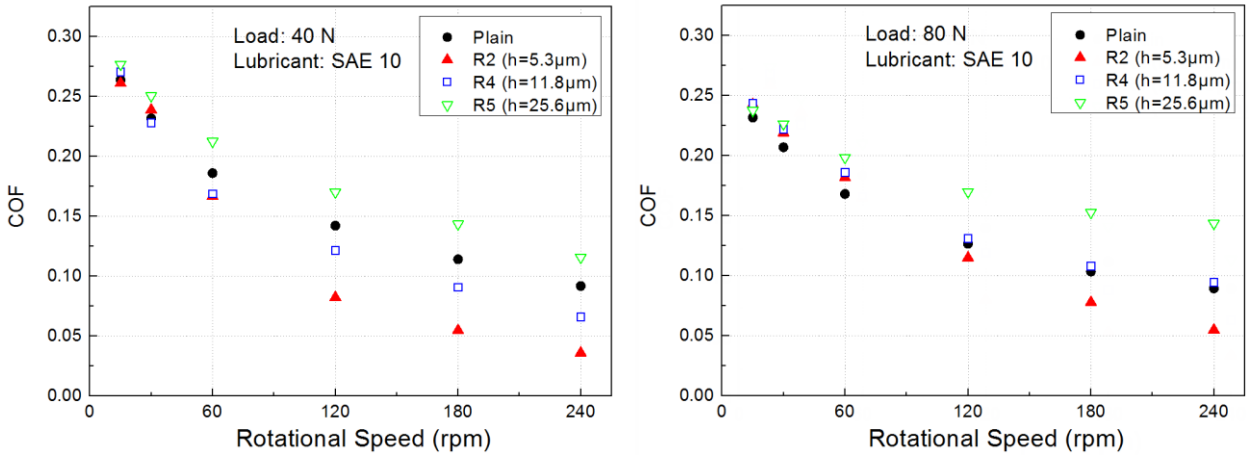

Figure 6-7 The effect of pocket depth on the frictional performance

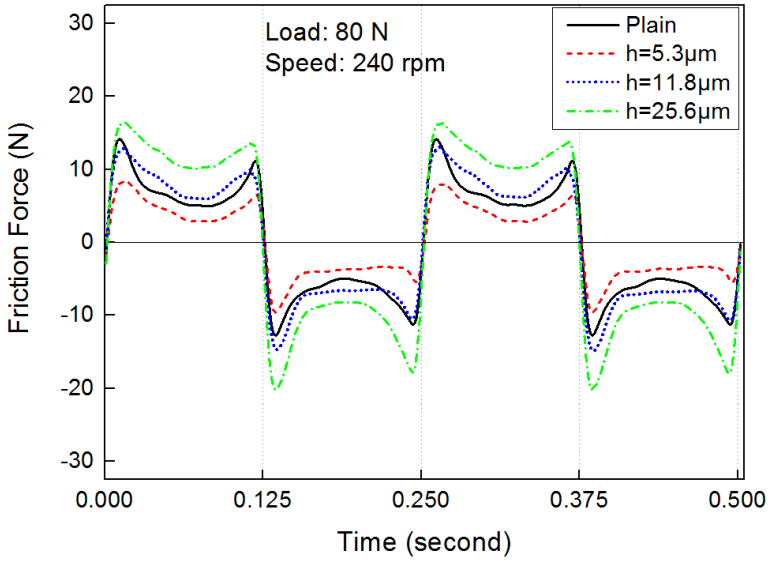

Figure 6-8 Friction force comparison between specimens with different pocket depths

Figure 6-8 shows the friction force comparison between the specimens with different pocket depths. It can be seen that shallow pockets (with depth of 5.3 μm) show superior performance compared to others throughout the full cycle of the reciprocating motion while deep pockets (with depth of 25.6 μm) yield higher friction.

6.4.4.3 Effect of Pocket Shape

Figures 6-9 and 6-10 present the effect of pocket shape on the frictional behavior of pocketed specimens. Three shapes are considered for comparison in this study: square (R2), semiellipse (E1) and trapezoid (T1). In order to concentrate on the shape effect, all the pockets have the same area ratio, depth and inlet width. The figures show that, under the conditions tested, the pocket shape has a minor effect on the friction performance. All the pocketed specimens have nearly identical COF, except that semiellipse and trapezoid pockets show a slightly lower COF under low load and high speed conditions. Furthermore, the friction variations of the three pocketed specimens are also similar during a full reciprocating cycle. They are consistently lower than that of the plain surface specimen. The influence of pocket shape on the fluid lubrication is further discussed in Section 6.4.4.

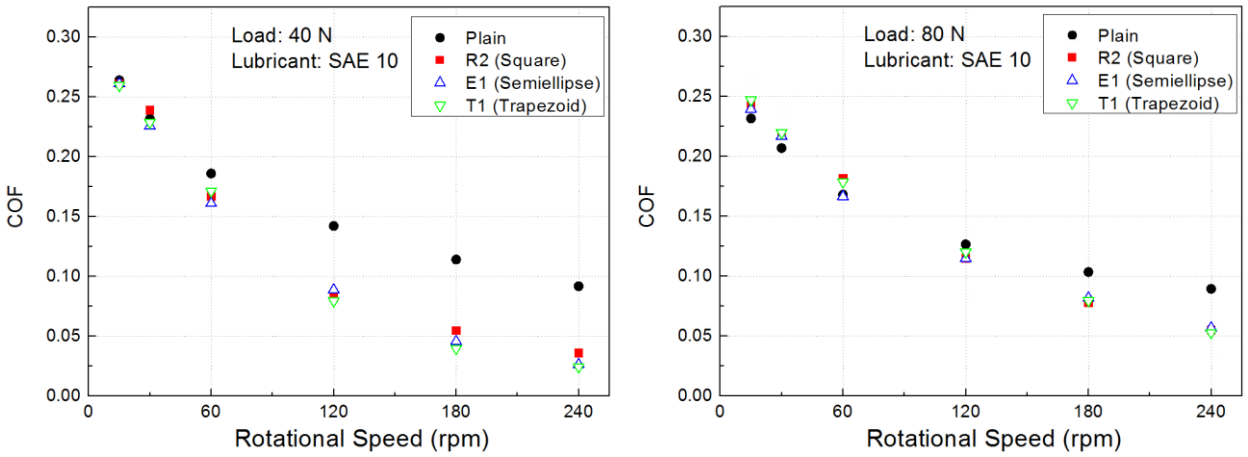

Figure 6-9 The effect of pocket shape on the frictional performance

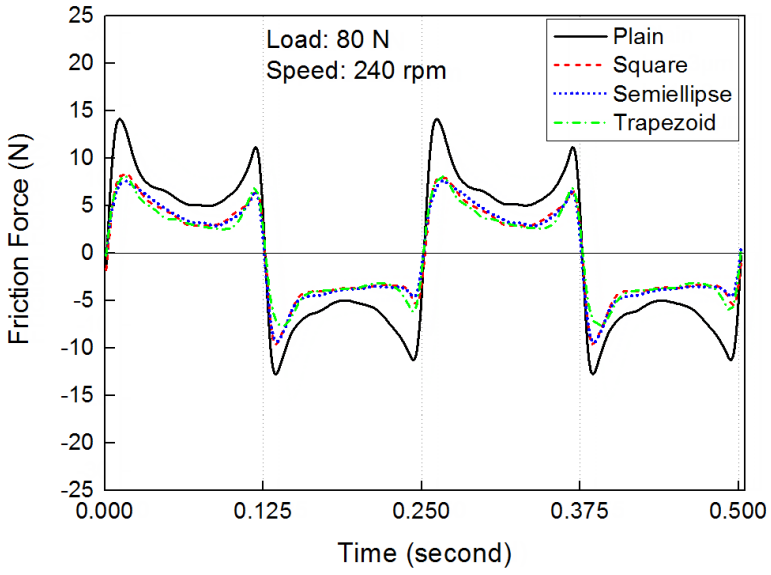

Figure 6-10 Friction force comparison between specimens with different pocket shapes

6.5 Numerical Analysis

Although the tested specimens operate in the mixed lubrication regime wherein both the asperity contact and hydrodynamic pressure contribute to load-carrying capacity, this numerical analysis only concentrates on the fluid film portion because the major mechanism of friction reduction is associated with the hydrodynamic lift that the pockets generate. The overall trend of the pocketed specimens' performance can be explained by examining the hydrodynamic lubrication prediction. Generally, the greater the hydrodynamic load generated within the pockets, the less is the load supported by the asperities so that the frictional contribution of surface asperities drops and the total friction decreases. Therefore, in this numerical study we focus our attention to the effect of pocket geometries on fluid film lubrication. The simulation results are primarily used to help explain the test results of pocketed specimens in previous section.

6.5.1 Governing Equations

Assuming that the lubricant is Newtonian and incompressible and that the flow remains laminar and steady, the hydrodynamic pressure within lubricant film can be predicted by the Reynolds equation:

$$\frac{\partial}{\partial x}\left(h^3\frac{\partial p}{\partial x}\right)+\frac{\partial}{\partial y}\left(h^3\frac{\partial p}{\partial y}\right)=6\mu U\frac{\partial h}{\partial x} \tag{1}$$

To deal with cavitation in the lubrication, a modified Reynolds equation (p-θ model) is used in this study. This formulation is capable of describing both the full-film and cavitation regions and distinguish the boundaries of cavitated zone automatically [29-30]. It has been successfully applied in the prediction of cavitation within surface textures [31-33]. The mass-conservative form of the Reynolds equation can be written as

$$\frac{\partial}{\partial x}\left(h^3\frac{\partial p}{\partial x}\right)+\frac{\partial}{\partial y}\left(h^3\frac{\partial p}{\partial y}\right)=6\mu U\frac{\partial(\theta h)}{\partial x} \tag{2a}$$

$$p > p_c \qquad \theta = 1 \tag{2b}$$

$$p = p_c \qquad \theta < 1 \tag{2c}$$

where θ is fluid fraction variable and p_c is cavitation pressure. To non-dimensionalize Eq. (2), the following dimensionless terms are defined:

$$\bar{x}=\frac{x}{L},\ \bar{y}=\frac{y}{L},\ \bar{h}=\frac{h}{h_0},\ \bar{p}=\frac{p}{p_0},\ \Lambda=\frac{6\mu UL}{p_0h_0^2} \tag{3}$$

where L is the length of the unit cell, h_0 is the minimum film thickness and p_0 is the ambient pressure. Substituting Eq. (3) in Eq. (2) yields the dimensionless form of the modified Reynolds equation:

$$\frac{\partial}{\partial \bar{x}}\left(\bar{h}^3 \frac{\partial \bar{p}}{\partial \bar{x}}\right)+\frac{\partial}{\partial \bar{y}}\left(\bar{h}^3 \frac{\partial \bar{p}}{\partial \bar{y}}\right)=\Lambda \frac{\partial\left(\theta \bar{h}\right)}{\partial \bar{x}} \tag{4}$$

6.5.2 Geometric Model and Boundary Conditions

The geometric model of the pocketed piston ring surface is illustrated in Figure 6-11. The micro pockets are distributed uniformly on the two sides of the surface. Due to the periodicity in the Y direction, it is sufficient to analyze only one imaginary unit cell that contains a pocket on each side, as shown in Figure 6-11.

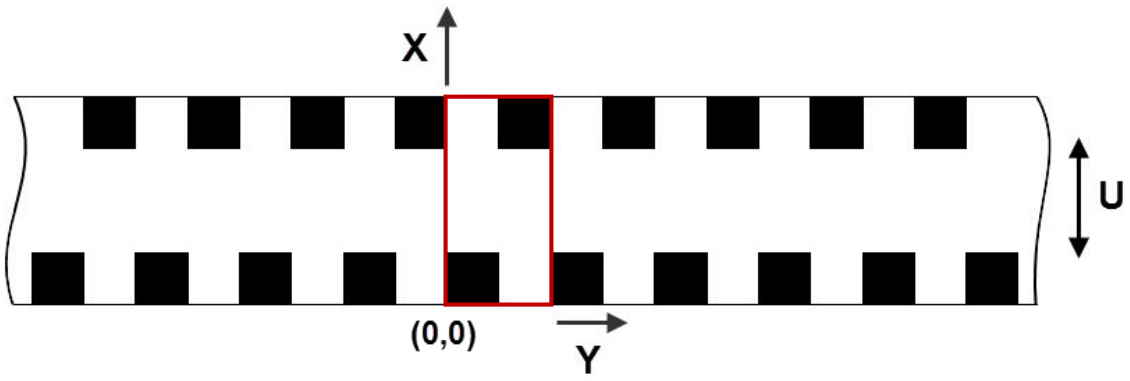

Figure 6-11 Geometric model of pocketed piston ring surface

The dimensionless local film thickness $\bar{h}$ for a unit cell can be described as

$$\bar{h}=\begin{cases}1+\bar{h}_g & \left(\bar{x},\bar{y}\right)\in \text{pocket area} \\ 1 & \text{else}\end{cases} \tag{5}$$

where $\bar{h}_g$ is the dimensionless pocket depth. Figure 6-12 shows the lubricant film profiles of the unit cells with different pocket shapes.

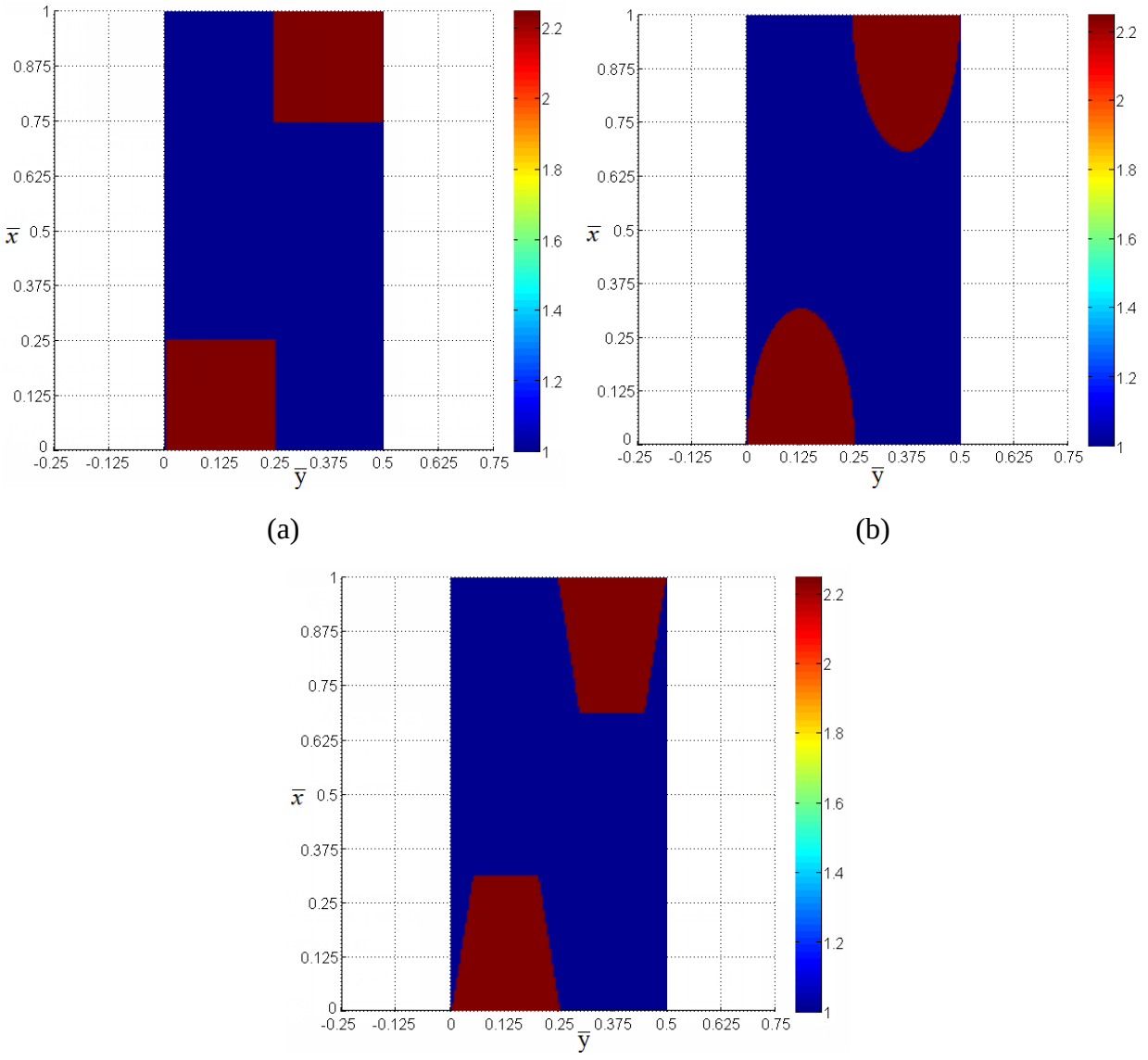

Figure 6-12 Lubricant film profiles of specimens R2, E1 and T1 ($\bar{h}_g$ =1.25)

To gain further insight into the effect of the pockets, the barrel-shaped ring configuration with a symmetric parabolic surface is also considered in the numerical simulation. The film thickness of pocketed barrel-shaped ring can be expressed as

$$\bar{h} = \begin{cases} 1 + 4\kappa\left(\bar{x} - 1/2\right)^2 + \bar{h}_g & \left(\bar{x}, \bar{y}\right) \in \text{ pocket area} \\ 1 + 4\kappa\left(\bar{x} - 1/2\right)^2 & \text{else} \end{cases} \tag{6}$$

where κ is dimensionless piston ring curvature and is defined as the ratio between the piston ring crown height (δ) and the minimum film thickness.

$$\kappa = \frac{\delta}{h_0} \tag{7}$$

Since the piston ring segment is fully lubricated in this study, the dimensionless boundary conditions at the leading and trailing edges of the ring are given by:

$$\bar{p} = 1 \qquad \text{at } \bar{x} = 0 \text{ and } \bar{x} = 1 \tag{8}$$

The periodic boundary conditions in Y direction are as follows

$$p(\bar{x}, 0) = p(\bar{x}, \frac{B}{L}) \tag{9}$$

$$\frac{\partial p(\bar{x}, 0)}{\partial y} = \frac{\partial p(\bar{x}, \frac{B}{L})}{\partial y} \tag{10}$$

where B is the width of the unit cell.

6.5.3 Solution and Performance Parameters

The finite difference formulation is applied to discretize the modified Reynolds Equation Eq. (4), which leads to a set of linear algebraic equations. These equations are then solved with an iterative algorithm proposed by Ausas et al. [30, 34]. This algorithm combines a relaxation scheme with corrections to implement the cavitation boundary conditions in Eqs. (2b) and (2c). Once Eq. (4) is solved based on the given film profile and boundary conditions, the hydrodynamic pressure

distribution is determined. The non-dimensional load-carrying capacity (LCC) of a unit cell can be obtained by integrating the dimensionless pressure over the computational domain:

$$\overline{W} = \int_0^{B/L} \int_0^1 \bar{p} d\bar{x} d\bar{y} \tag{11}$$

This parameter is used for evaluating the effectiveness of different pocket geometries to improve the tribological performance.

6.5.4 Performance Study

Table 6-3 shows the input parameters used in the simulations. For the parametric study of the pocket geometry, both pocket area ratio and pocket depth are varied over a wide range to determine their influence on the hydrodynamic lubrication. Other geometric parameters of the pockets are kept the same as those used in the experiments. The LCC of three pocket shapes are also compared under different operating conditions to investigate its effect on the lubrication performance.

Table 6-3 The input parameters for the simulation

Parameter	Value
Unit cell length L (mm)	4
Unit cell width B (mm)	2
Minimum film thickness h_0 (μm)	4
Viscosity μ (Pa.s)	0.06
Cavitation pressure p_c (Pa)	0.3×10^5
Ambient pressure p_a (Pa)	1×10^5 Pa
Pocket area ratio r	5% - 50%
Dimensionless pocket depth $\bar{h}_g$	0.1 - 5
Sliding Speed U (m/s)	0.1 - 1

Figure 6-13 presents the relationship between the load-carrying capacity and the pocket area ratio under different sliding speeds. The area ratio (AR) is varied from 5% to 50%, corresponding to pocket lengths from 0.2 to 2 mm, and the pocket depth is fixed at 5 μm ($\bar{h}_g$=1.25). The results show that, under the conditions simulated, the LCC exhibits a similar trend for different speeds: it increases to a maximum value and then decreases rapidly with increasing pocket area ratio.

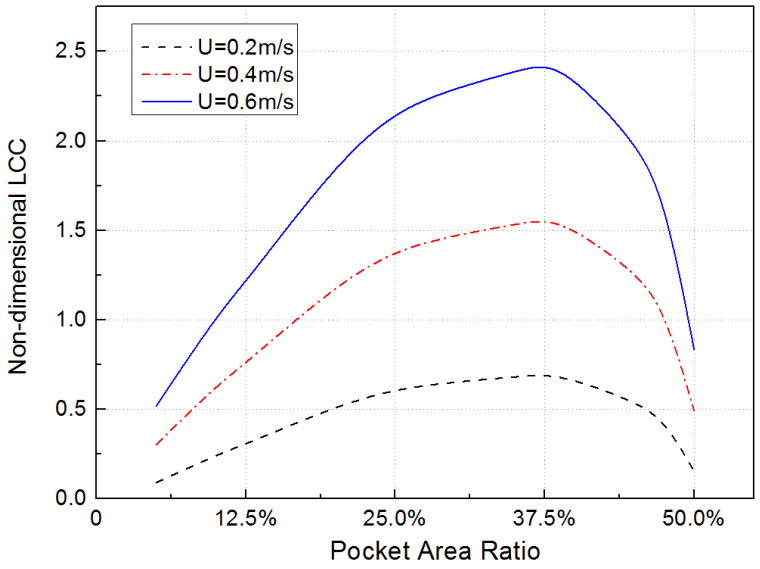

Figure 6-13 The influence of the area ratio on the load-carrying capacity (rectangular, $\bar{h}_g$=1.25)

This indicate that there exists an optimum area ratio of the pockets which produces the highest LCC and its value is not affected by the sliding speed. This trend agrees with the test results that the area ratio plays an important role in the performance of pocketed specimen. Neither the high nor the low area ratio is beneficial in reducing the friction, and an optimum area ratio can be found corresponding to the lowest COF. However, the best area ratio is 25% among the specimens tested, which is lower than that from the simulations (37.5%). This discrepancy is thought to be due to the detrimental effects of the pockets that tend to increase the friction. As can be seen in Figure 6-

13, when the area ratio is increased from 25% to 37.5%, the benefits gained from the pockets (the rate of LCC improvement) becomes small. On the other hand, the detrimental effects of the pockets could increase with the area ratio. As a result of the two factors, the friction-reduction effect of the pockets decreases when the area ratio is high, and according to the experimental results, pockets perform optimally with an area ratio around 25%.

Figure 6-14 shows the behavior of load-carrying capacity as a function of the pocket depth at three sliding speeds. As can be seen, the pocket depth has a major influence on the LCC and its optimum value in dimensionless form is around 0.8 for the maximum LCC. When the pocket depth is greater than the film thickness ($\bar{h}_g$>1), the LCC drops with increasing depth. As a result, the LCC produced by deep pockets ($\bar{h}_g$>5) is very limited. This trend is in good agreement with the experimental results that deep pockets do not have friction reduction effect.

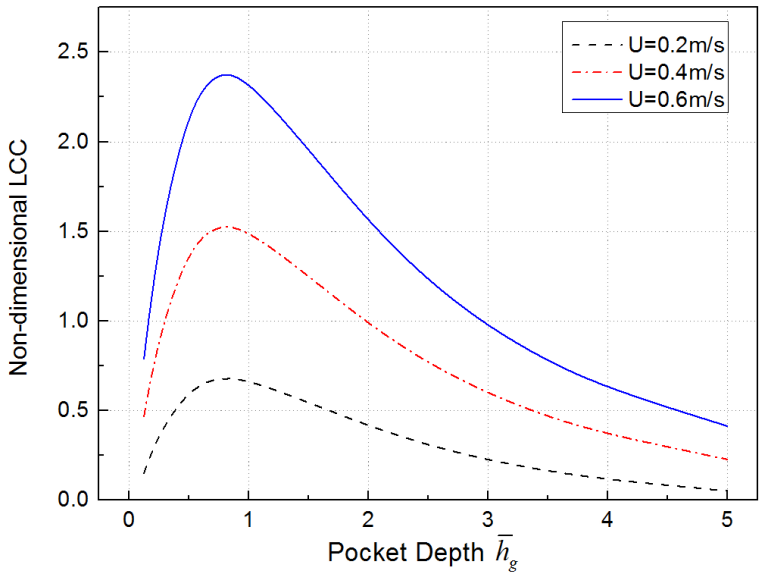

Figure 6-14 The influence of the pocket depth on the load-carrying capacity

The load-carrying capacities of three pocket shapes are compared in Figure 6-15. The results show that, under the conditions simulated, the pocket shape has a very minor effect on the LCC and

semiellipse and trapezoid pockets show a slight advantage over the square pocket at high speeds. This trend also agrees with the experimental comparison of different pocket shapes since the specimens R2, E1 and T1 have similar frictional behavior and specimens E1 and T1 show a slightly lower COF under low load and high speed conditions.

Figure 6-16 presents the dimensionless pressure distribution of the pocketed surfaces. The flow direction of the lubricant is from bottom to top in the figure. Their hydrodynamic pressure distributions show similar features: the peak pressure occurs around the rim of the pocket at the leading edge and the lubricant film cavitates within the pocket at the trailing edge. The LCC of the pocketed surface depends on both the area and magnitude of the hydrodynamic pressure. It can be seen that the semi-ellipse and trapezoid pockets generates higher peak pressure than the square pocket, which is due to the converging geometry they have in the motion direction. But the square pocket possess a larger area of pressure build-up. As a result, the total LCC of the three pocket shapes are quite close (see Figure 6-15).

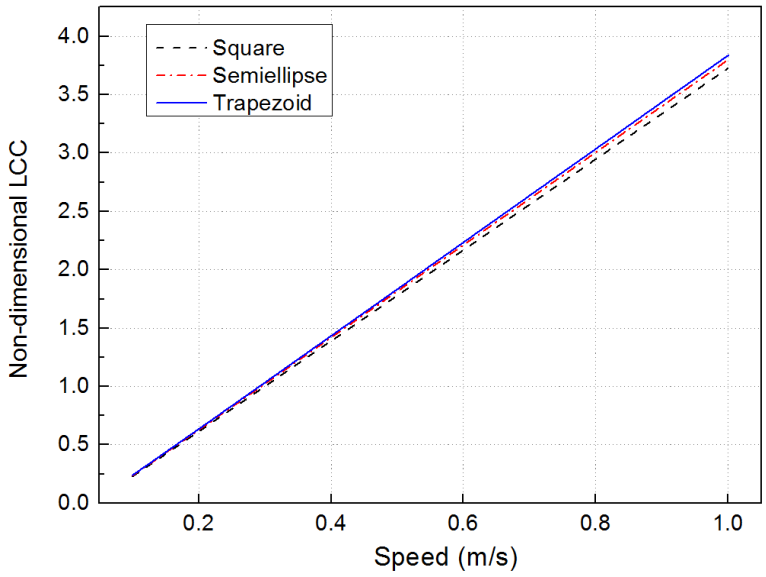

Figure 6-15 The influence of the pocket shape on the load-carrying capacity

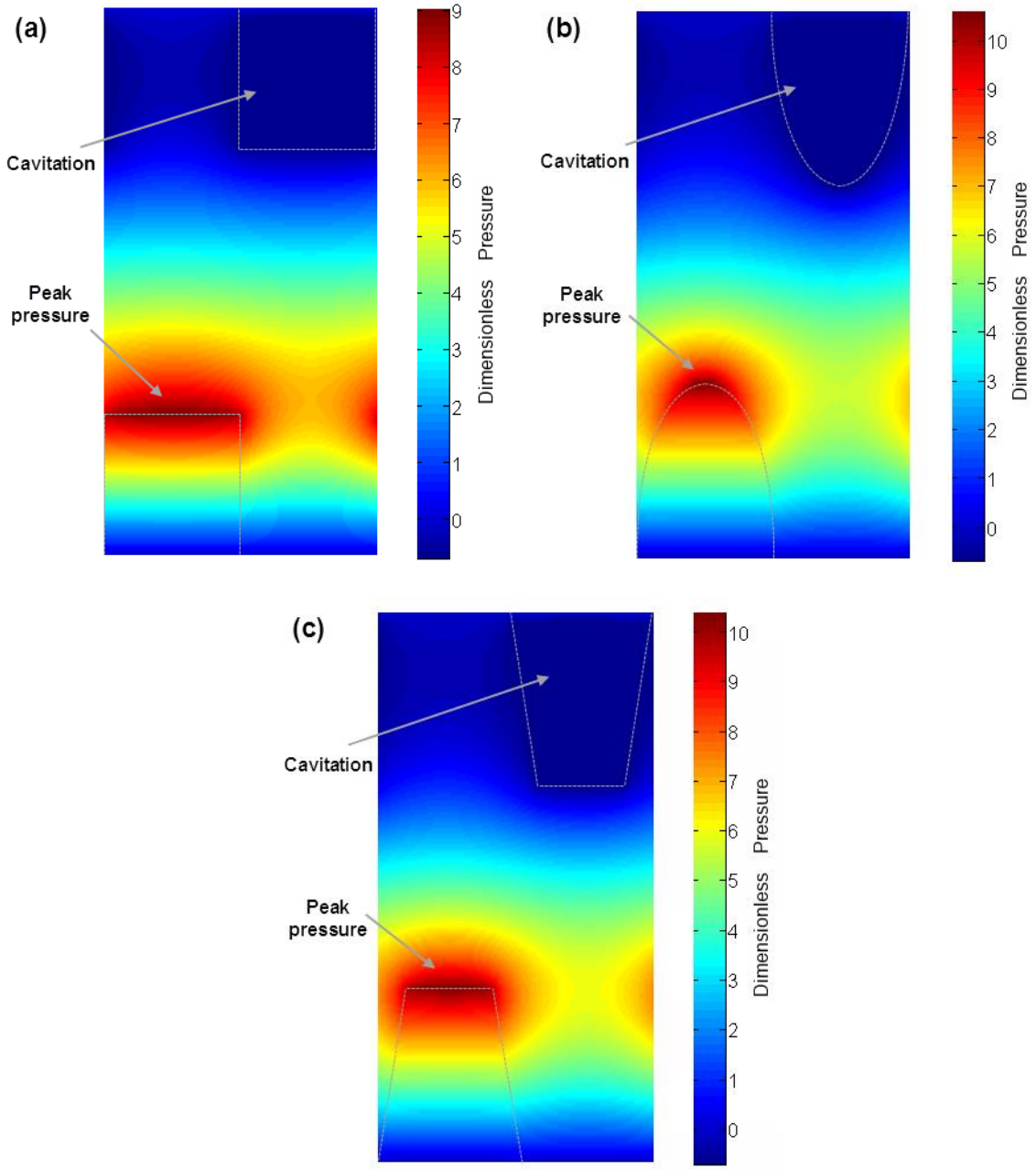

Figure 6-16 Pressure distributions of different pocket shapes (AR = 25%, $\bar{h}_g$ =1.25, U = 0.4m/s)

The surface profile plays an important role in the tribological performance of the piston ring. A barrel shape is usually formed on the ring surface either by the wear-in process or by the manufacturing to improve the lubrication characteristics. Preliminary numerical simulations were also conducted to investigate the effect of the laser machined pockets on the performance of the

barrel-shaped ring. Figure 6-17 show the load-carrying capacity of smooth and pocketed rings as a function of the piston ring curvature. As can be seen, the LCC of different rings show similar trend. They increase to a maximum value at $\kappa \approx 1.5$ and then decrease with increasing value of κ. Compared with smooth ring, the pocketed rings generate significantly higher LCC for the dimensionless curvature with relatively small values ($\kappa < 1.5$). As the curvature is further increased, the beneficial effect of the pockets on the LCC becomes negligible. However, it needs to be mentioned that another benefit of the pockets is their ability to supply oil into the contact surface under starved lubrication, especially around the dead centers. This beneficial effect should also exist for barrel-shaped ring. Based on the above analysis, the laser machined pockets should also be able to improve the performance of barrel-shaped ring, especially for those with small curvature. Further studies on the pocketed barrel-shaped ring are needed for a better understanding and application of the laser machined pockets.

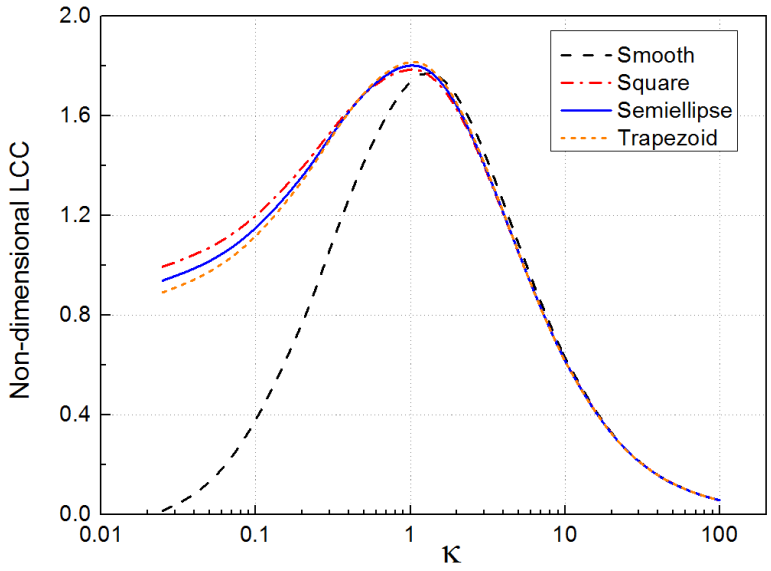

Figure 6-17 The load-carrying capacity of smooth and pocketed barrel-shape rings as a function of the piston ring curvature (AR=25%, $\bar{h}_g$ =0.25, U = 0.4 m/s)

6.6 Conclusions

This study presents a new design of pocketed piston rings for the friction reduction at the piston ring/cylinder liner (PRCL) interface. Miro-pockets with different geometric parameters (area ratio, depth and shape) were fabricated on the flat piston ring specimens using a laser. Their frictional performances were evaluated in a tribometer equipped with a reciprocating drive. The experimental results show that the pocket area ratio and depth have a major influence on the frictional behavior while the effect of the pocket shape is very limited. Under the conditions tested, the pockets with appropriate size (AR = 25%, depth = 5μm) can greatly lower the friction of PRCL contact. On the other hand, those pockets with large area ratio or depth do not show friction reduction effect.

Numerical simulations, based on the mass-conservative model of Elrod and Adams, were also performed to investigate the effect of pocket geometric parameters on the fluid lubrication. The simulation results agree with the trend in experimental results that large pocket area ratio and depth do not favor the hydrodynamic lubrication. Furthermore, the predicted load-carrying capacities of three pocket shapes are quite close. This agrees with the limited influence of the pocket shape in the experiments.

6.7 References

[1] Richardson D.E., 2000, "Review of power cylinder friction for diesel engines," Trans. ASME J. Eng. Gas Tur. Power, 122, pp. 506 – 519.

[2] Tung S.C., McMillan M.L., 2004, "Automotive tribology overview of current advances and challenges for the future," Tribol. Int., 37, pp. 517–536.

[3] Holmberg, K., Andersson, P., Erdemir, A., 2012, "Global energy consumption due to friction in passenger cars," Tribol. Int., 47, pp. 221–34.

[4] Donnet C., Erdemir A., 2004, “Historical developments and new trends in tribological and solid lubricant coatings,” Surf. Coat. Technol., 180–181, pp.76–84.

[5] Erdemir A., 2005, “Engineered tribological interfaces for improved boundary lubrication,” Tribol. Int., 38, pp. 249–256.

[6] Ronen A., Etsion I., Kligerman Y., 2001, “Friction-reducing surface texturing in reciprocating automotive components,” Tribol. Trans., 44(3), pp. 359–366.

[7] Ryk, G., Kligerman, Y., Etsion, I., 2002, “Experimental investigation of laser surface texturing for reciprocating automotive components,” Tribol.Trans., 45(4), pp. 444–449.

[8] Ryk G., Kligerman Y., Etsion I., Shinkarenko A., 2005, “Experimental investigation of partial laser surface texturing for piston rings friction reduction,” Tribol.Trans., 48(4), pp.583–588.

[9]] Ryk G., Etsion I., 2006, “Testing piston rings with partial laser surface texturing for friction reduction,” Wear, 261(7-8), pp.792–796.

[10] Kligerman Y., Etsion I., Shinkarenko A., 2005, “Improving tribological performance of piston rings by partial surface texturing,” ASME J. Tribol., 127(3), pp. 632–628.

[11] Etsion, I., and Sher, E., 2009, “Improving fuel efficiency with laser surface textured piston rings,” Tribol. Int., 42(4), pp. 542–547.

[12] Martin J.M., Ohmae N., 2008, “Nanolubricant,” John Wiley & Sons, Inc., Sussex, UK.

[13] Bolander, N. W., Sadeghi, F., 2006, “Surface modification for piston ring and liner,” IUTAM Symposium on Elastohydrodynamics and Microelastohydrodynamics, Snidle R.W. and Evans H.P., eds., Springer, The Netherlands, pp. 271–283.

[14] Gadeschi G.B., Backhaus K., Knoll G., 2012, Numerical analysis of laser-textured piston-rings in the hydrodynamic lubrication regime,” ASME J. Tribol., 134, pp. 041702.

[15] Tomanik E., 2013, “Modelling the hydrodynamic support of cylinder bore and piston rings with laser textured surfaces,” Tribol. Int., 59, pp. 90–96.

[16] Zavos A.B., Nikolakopoulos P.G., 2015, “Simulation of piston ring tribology with surface texturing for internal combustion engines,” Lubr. Sci., 27(3), pp. 151-176.

[17] Tomanik E., 2008, “Friction and wear bench test of different engine liner surface finishes,” Tribol. Int. 41, pp.1032–1038.

[18] Grabon W., Koszela W., Pawlus P., Ochwat S., 2013, “Improving tribological behaviour of piston ring–cylinder liner frictional pair by liner surface texturing,” Tribol. Int., 61, pp. 102–108.

[19] Koszela W., Pawlus P., Rejwer E., Ochwat S., 2013, “Possibilities of oil pockets creation by the burnishing technique,” Arch. Civ. Mech. Eng., 13(4), pp. 465–471.

[20] Yin B., Li X., Fu Y., Wang Y., 2012, “Effect of laser textured dimples on the lubrication performance of cylinder liner in diesel engine,” Lubr. Sci. 24, pp. 293–312.

[21] Mezghani S., Demirci I., Zahouani H., Mansori M. El., 2012, “The effect of groove texture patterns on piston-ring pack friction,” Precis. Eng., 36(2), pp. 210-217.

[22] Checo H.M., Ausas R.F., Jai M., Cadalen J.P., Choukroun F., Buscaglia G.C., 2014, “Moving textures: simulation of a ring sliding on a textured liner,” Tribol. Int., 72, pp. 131–142.

[23] Morris N., Rahmani R., Rahnejat H., King P.D., Howell-Smith S., 2016, “A numerical model to study the role of surface textures at top dead center reversal in piston ring to cylinder liner contact,” ASME J. Tribol., 138, pp. 021703.

[24] Wang, X., Wang, J., Zhang, B., Huang W., 2014, “Design principles for the area density of dimple patterns,” Proc. IMechE. Part J: J. Engineering Tribology, 229, pp. 538–546.

[25] Qiu, Y., Khonsari M.M., 2011, “Experimental investigation of tribological performance of laser textured stainless steel rings,” Tribol. Int., 44, pp. 635–644.

[26] Ripoll M.R., Podgornik B., Vizintin J., 2011, “Finite element analysis of textured surfaces under reciprocating sliding,” Wear, pp. 952–959.

[27] Bolander N.W., Steenwyk B.D., Sadeghi F., Gerber G.R., 2005, “Lubrication Regime Transitions at the Piston Ring-Cylinder Liner Interface,” Proc. Inst. Mech. Eng., Part J, 219(1), pp. 19–31.

[28] Khonsari, M.M., Booser, E.R., 2008, “Applied Tribology–Bearing Design and Lubrication,” Second Edition, John Wiley & Sons, Inc., Sussex, UK.

[29] Elrod H.G., Adams M., 1974, “A computer program for cavitation,” 1st Leeds-Lyon Symposium on Cavitation and Related Phenomena in Lubrication, I.M.E., Mechanical Engineering Publication, New York, 103, pp. 37-41.

[30] Ausas R., Ragot P., Leiva J., Jai M., Bayada G., Buscaglia G., 2007, “The impact of the cavitation model in the analysis of microtextured lubricated journal bearings,” ASME J. Tribol., 129, pp. 868-875.

[31] Qiu, Y., Khonsari M.M., 2011, “Performance analysis of full-film textured surfaces with consideration of roughness effects”, ASME J. Tribol., 133, pp. 021704:1-10.

[32] Shen, C. and Khonsari, M. M., 2013, “On the magnitude of cavitation pressure of steady-state lubrication,” Tribol. Lett., 51, pp.153-160.

[33] Shen C., Khonsari M. M., 2013, “Effect of dimple's internal structure on hydrodynamic lubrication”, Tribol. Lett., 52, pp. 415–430.

[34] Ausas, R., Jai, M., Buscaglia, G. 2009, “A mass-conserving algorithm for dynamical lubrication problems with cavitation,” ASME J. Tribol., 131, pp. 031702.

CHAPTER 7 EXPERIMENTAL INVESTIGATION OF TRIBOLOGICAL AND SEALING PERFORMANCE OF LASER POCKETED PISTON RINGS

7.1 Introduction

As an effective method to improve the tribological performance, surface texturing has been used in a wide range of applications, including mechanical seals, journal bearings, thrust bearings, cutting tools and even artificial hip joints [1-8]. Due to stricter requirements on the efficiency and emission of internal combustion engines, there is a heightened need for reducing friction losses in an engine, especially at the interface between piston rings and cylinder liners. As a result, the application of surface texturing to the piston ring/cylinder liner contact has received increasing attention over the past years [9-20]. Because of the ease in manufacturing, most previous studies applied surface texturing to the outer surface of piston rings using a laser, which generated an array of micro dimples on the ring surface.

One of the early experimental studies on the textured piston rings was carried out by Ryk, et al [9]. They designed a reciprocating test rig to measure the friction between two production piston ring segments and a cylinder liner segment under controlled lubricant feeding rate. Based on the results of a theoretical modelling, they fabricated dimples with diameter of 100 μm, depth of 10 μm and area ratio of 20% on the surface of piston ring segments. A friction reduction from 20 to 30 percent due to texturing was observed in their experiments. In a following work [10,11], they proposed a design of partial laser surface texturing for piston rings where textures were fabricated on only a portion of the ring face, and evaluated its effect on the friction reduction. The comparison of frictional performance was made between cylindrical shape rings with partial texturing and non-textured barrel face rings. It was reported that cylindrical face rings with partial surface texturing can lead to a friction reduction of up to 25%. Later, real engine tests with a dynamometer were

conducted by Etsion and Sher [12] to compare the fuel efficiency and exhaust gas composition of engines using partially textured piston rings and non-textured barrel-shaped piston rings. They found that optimum partial surface texturing resulted in a reduction of up to 4% in fuel consumption but had no significant influence on the exhaust gas composition. Bolander and Sadeghi [13] also modified the piston ring surface by laser texturing and compared the performances of circular dimples with different dimensions (dimple diameter and depth). Their experimental results showed that textured piston rings with shallow dimples exhibit lower friction on a polished liner segment. In a recent study of the present authors [20], a new design of surface modification was proposed for the piston ring surface, which involves creating micro oil pockets at the inlet and outlet of the ring face. During the reciprocating motion, the pockets at the leading edge can function as tiny step bearings and hence generate hydrodynamic pressure to improve the lubrication. A series of experiments were performed to investigate the geometric parameters (area ratio, depth and shape) of the pockets on the tribolgoical performance of piston ring prototypes. It was found that the pockets with appropriate size can greatly lower the friction at the piston ring/cylinder liner contact.

In most of the previous experimental work on textured piston rings, a reciprocating test rig was utilized to measure the friction between piston ring segments and cylinder liner segment and the ring specimens were fixed in a holder while the cylinder liner had a reciprocating motion. This test configuration oversimplified the motion of piston rings and did not account for the secondary motion of piston and piston rings (radial motion, elastic deformation and twist) in a cylinder, which could have a significant influence on the piston ring lubrication [21]. Therefore, a motorized engine tests using a piston and a piston ring-pack is desirable for evaluation of textured piston rings, since it can better simulate the piston ring motion and lubrication in real engines. Moreover, the sealing

performance of textured piston ring should also be assessed, since the primary function of piston rings is to form a moving seal between the piston and cylinder wall. If the design of surface texturing reduces the sealing capability of piston rings, it would increase the blow-by and lubricant oil consumption and hence decrease the engine efficiency, even though the texturing could help reduce friction loss.

In the present study, a motorized test apparatus was developed to evaluate the frictional and sealing performance of piston rings. It reciprocates a production piston and piston ring-pack from a diesel in a corresponding cylinder liner. This test rig was used in a series of friction and compression pressure tests to compare the performance of flat and pocketed piston rings.

7.2 Experiment

7.2.1 Description of Experimental Apparatus

The experiments were conducted using a custom-built reciprocating piston test apparatus that enables both friction and compression pressure measurements. This test apparatus applies the floating liner method [22, 23] to directly measure the piston friction and utilizes the cylinder liner, piston, piston rings and connecting rod from a diesel engine (Perkins 4.236). Figure 7-1 shows the schematic of the machine. The reciprocating motion of the piston assembly is achieved with an electric motor driving the crankshaft through a set of pulleys. The pulley drive ratio is 3.4:1, and the large pulley connected to the crankshaft can work as a flywheel to ensure the smooth motion of the piston. The stroke length used in the study is 114.3 mm, which is similar to that in a typical engine. The rotating speed and angular position of the crankshaft is recorded by a rotary encoder, attached to the end of the crankshaft.

The test apparatus has two configurations for the cylinder liner: a suspended configuration for measuring the friction force and a fixed configuration for measuring the compression pressure. During the friction tests, the cylinder liner is suspended by a load cell to measure the axial friction force, as shown in Figure 7-2a. The radial motion of the cylinder liner is prevented by three lateral supports positioned at 120° spacing. Each lateral support is equipped with two ball bearings that maintain the center position of the liner and allow for its smooth motion in the axial direction. The weight of the cylinder liner and its fixture is counterbalanced by a lever and weight assembly to eliminate its influence on the friction measurement. The cylinder liner is open at its end without a cylinder head in the friction tests so that the compression gas is not sealed and the friction is the only force acting on the suspended liner.

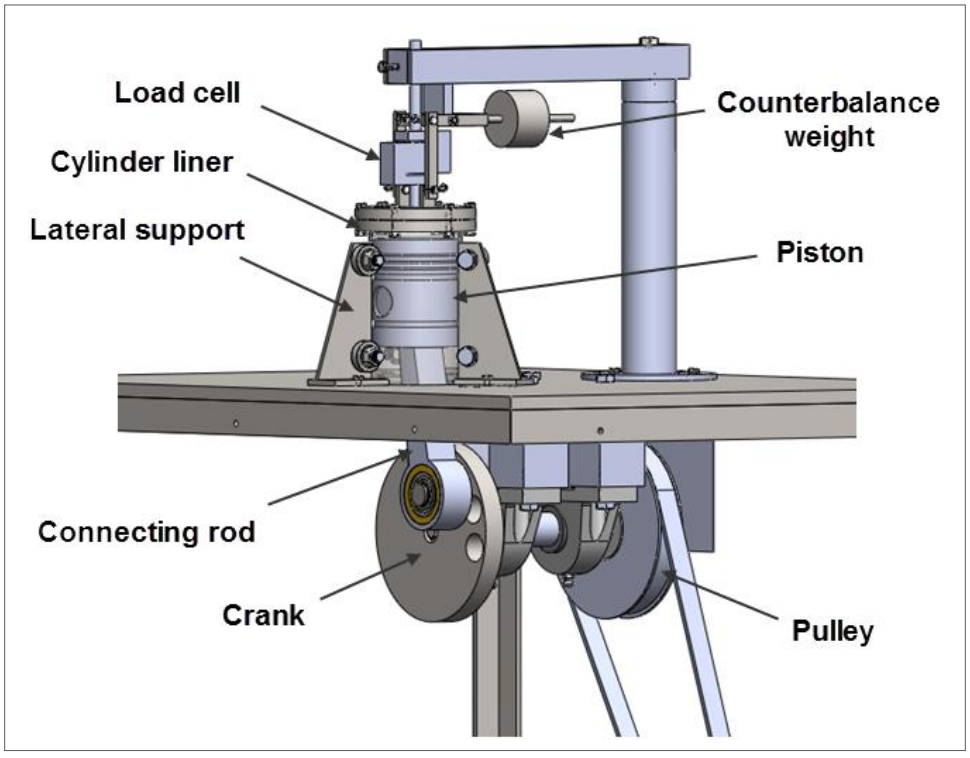

Figure 7-1 Schematic of the test rig

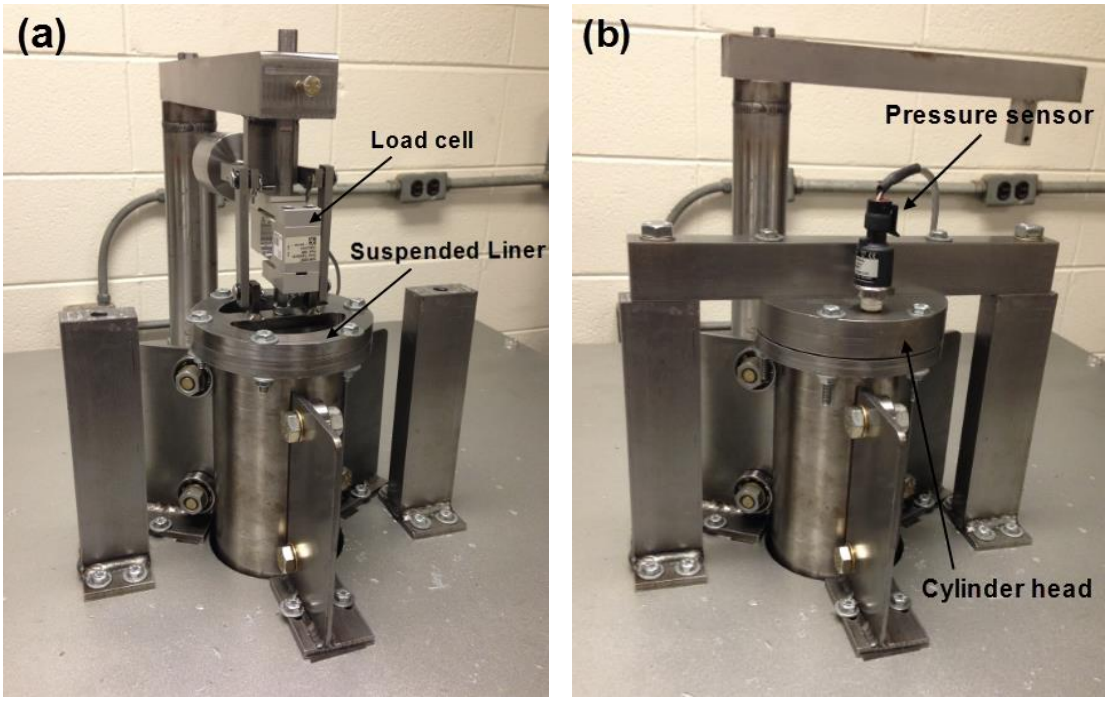

Figure 7-2 Final assembly of the test rig: (a) suspended-liner configuration for friction test; (b) fixed-liner configuration for compression pressure test

In the compression pressure tests, the cylinder liner is sealed with a cylinder head and a gasket. Due to the high pressure loading, the liner is fixed to a support bar, as shown in Figure 7-2b. The lateral force acting on the liner is also balanced by three lateral supports. A pressure transducer with a range of 200 psi and accuracy of 1% is inserted through the cylinder head to monitor the pressure variation inside the liner.

Figure 7-3 shows the lubrication arrangement of the test rig. The lubricating oil is sprayed to the bottom of the piston and cylinder liner by using a nozzle connected to the oil circulation system. Some of the lubricant could flow through the holes in piston to the cylinder wall and then be regulated by the oil control rings. This is very similar to the lubricant flow in a real engine. The lubricant oil is stored in an oil tank before being pumped through a filter and its temperature can be controlled by a heater attached to the tank. An oil catcher is used to collect the lubricant that

falls out of the cylinder liner and drain it back to the tank. The oil flow rate is controlled by a valve available next to the gear pump and monitored by a flowmeter.

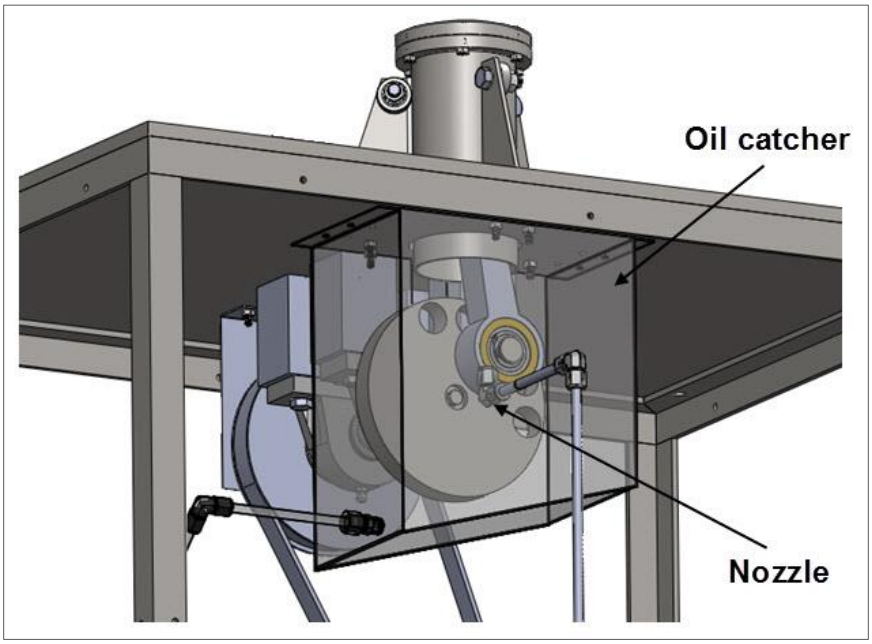

Figure 7-3 Lubrication arrangement of the test rig

All measurement data (including the data from the rotary encoder, load cell, pressure transducer and the thermocouple in the oil tank) are acquired with a data acquisition system and a LabVIEW program. This program is also capable of real-time data processing for reducing noise in the signal.

7.2.2 Specimen Preparation

The piston ring-pack used in this study consists of three compression rings and two oil control rings. Since the oil rings are too narrow for laser texturing, the micro pockets were only machined on the sliding surface of the compression rings, which are made of cast iron with a diameter of 99 mm and a width of 2.36 mm. All the compression rings have a flat surface with a surface roughness (Ra) of 0.32 μm, and only the top compression ring is coated with chrome.

A Nd:Ytterbium fiber laser (wavelength of 1064 nm) is used to fabricate micro pockets on the piston ring surface. The shape and distribution of the pockets are first designed using a CAD software and then imported into the laser device. The pocket depth is controlled by the power of the laser and the number of repeats the laser beam scans the surface. Figure 7-4 shows the surface of a laser pocketed compression ring. The geometric parameters of the pockets are listed in Table 7-1. These dimensions are selected based on a previous study [20], which identified the optimal range of the pocket size. The pocket depth is shallower than the previous study, because the piston ring/cylinder liner contact is not under submerged lubrication in this study and the lubricant film thickness is expected to be lower than that in previous tests.

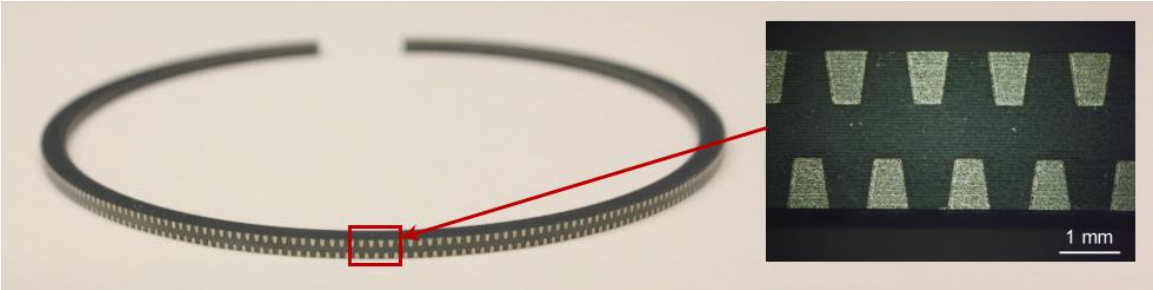

Figure 7-4 Image of pocketed compression ring

Table 7-1 Geometric parameters of lasered pockets

Parameters	Value
Pocket shape	Trapezoidal
Characteristic length	a = 0.6 mm; b = 0.36 mm; h = 0.75 mm
Pocket depth	3.9 – 4.2 µm
Pocket spacing	2.8 ° (circumferentially)
Total no. of pockets	516
Area ratio	25.3%

7.2.3 Experimental Procedure

Two types of experiments were performed: friction tests and compression pressure tests. Each piston ring-pack underwent both tests. The adjustable parameters in the experiments include: crank rotational speed, oil temperature (viscosity), oil supply rate and surface finish of the compression rings. In this study, the rotational speed was varied from 60 to 600 rpm. Testing at even higher speeds would be affected by the test rig vibration and require an ultrahigh sampling rate. An additive-free SAE 30 oil was used in the tests, and its bulk temperature was precisely controlled. Figure 7-5 shows the dynamic viscosity of the oil as a function of temperature. In order to evaluate the effect of lubricant viscosity, the friction tests were conducted at temperatures of 25 and 60 °C, which corresponds to dynamic viscosities of 0.17 and 0.03 Pa·s. The oil flow rate was maintained at 1.2 L/min for all the experimental tests.

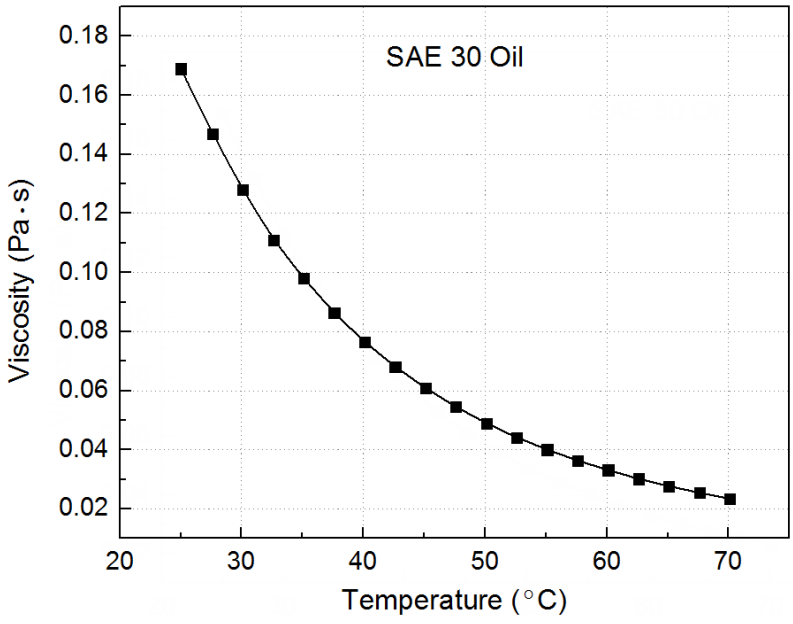

Figure 7-5 Dynamic viscosity of the lubricant oil as a function of temperature

The test procedure for friction measurement is as follows. First, the weight of cylinder liner and its fixture was balanced by adjusting the position of the counterbalance weight. Then, the piston

rings were installed in the test rig and the gear pump of the lubricant circulation system was turned on. After a running-in process of 6 hours, the friction tests were performed under various crank speeds ranging from 60 to 600 rpm. Friction data of 100 reciprocating cycles were collected for each test condition with 1000 data points per cycle, and a low pass filter was applied to reduce high frequency noise in the signal. The averaged friction force is used to represent the result of each test. It is calculated by averaging the absolute values of the friction force over 100 reciprocating cycles. A minimum of three non-consecutive tests were conducted for each test condition and their friction variations were compared to ensure the measurement consistency.

After the friction tests, the compression pressure tests were conducted with the same piston ring-pack at room temperature (25°C). A cylinder head and a gasket were installed to form a compression chamber. The rotational speed of the crank was set to 120, 180, 240 and 360 rpm in the compression tests. The oil flow rate and data sampling rate were the same as those in the friction tests. The pressure variation in the reciprocating cycles was recorded with a pressure transducer. The peak pressure of 100 cycles was averaged and used to evaluate the sealing performance of piston rings.

7.3 Results and Discussion

7.3.1 Friction Test Results

Figure 7-5 presents the average friction force versus the crank rotational speed for both smooth and pocketed piston rings. As can be seen, the average friction shows a persistent increase with the increasing crank speed. The measured friction consists of contributions from each piston ring and the piston skirt, and the friction force acting on each part includes a viscous shear force in the lubricant film and friction from contacting asperities. An increase in the speed would improve the hydrodynamic action, leading to increased fluid film separation and hence reduced asperity contact

and friction. On the other hand, the viscous shear force would increase with the sliding speed, since it is proportional to the shear rate and viscosity. These two competing factors influence the total measured force. The trend of increased friction with speed indicates that the increase of viscous force is more dominant in the total friction.

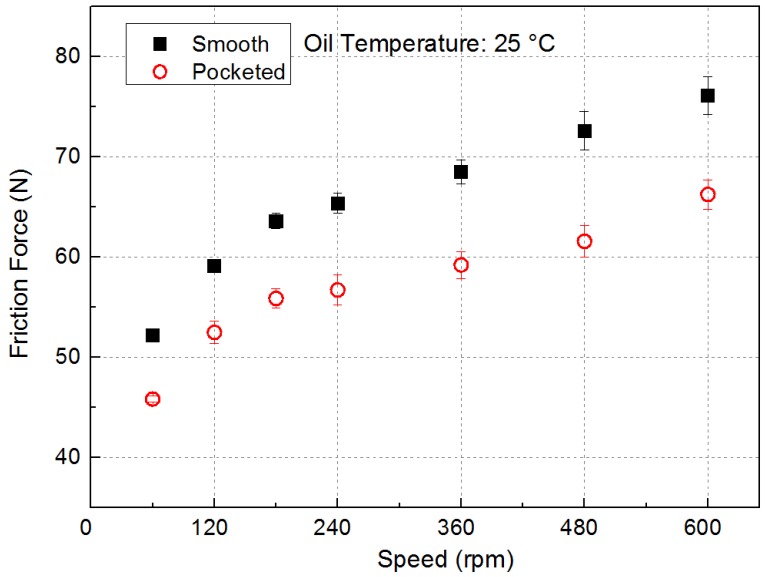

Figure 7-6 Comparison of averaged friction force at oil temperature of 25 °C

Comparing with the smooth piston rings, the pocketed rings have a consistently lower value of averaged friction over the entire speed range. The friction reduction resulted from the lasered pockets is about 11–15% of the total friction. The mechanism for the reduced friction is thought to be different depending on the operating conditions. The lubrication arrangement in this study is similar to that in real engines. Excess oil on the cylinder wall falls down to the oil catcher due to gravity and is also wiped off by the oil control ring, leaving only a thin layer of oil retained on the surface to provide lubrication. As a result, there would be a certain degree of oil starvation at the piston ring/cylinder liner interface, especially when the rotational speed is low and oil cannot be splashed onto the cylinder wall. The possible reason for the friction reduction of pocketed rings at low speed is that these pockets can act as oil-reservoirs during sliding, which helps to supply oil

to the contact surface and reduce asperity contacts. However, at high speeds where the hydrodynamic action is more dominant, the pockets are expected to work as tiny step bearings and generate additional hydrodynamic pressure and load-carrying capacity. Due to the above two mechanisms, the pocketed rings exhibits better performance over a wide speed range.

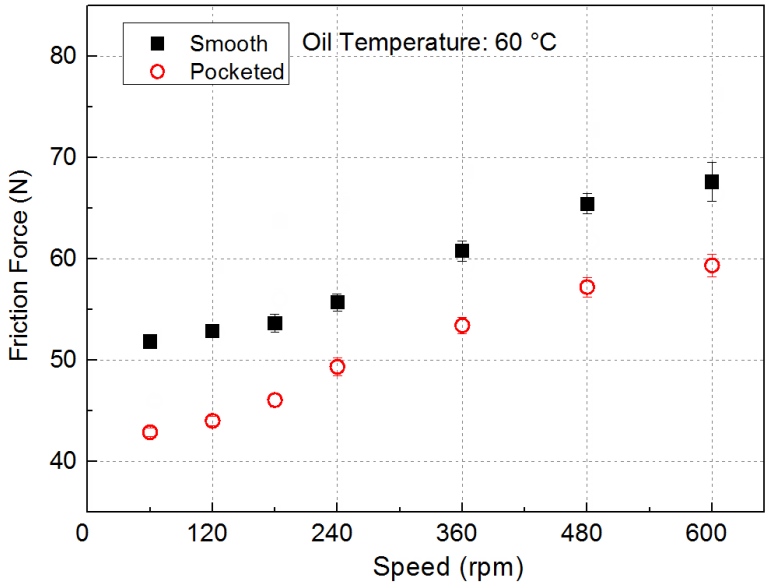

Figure 7-7 Comparison of averaged friction force at oil temperature of 60 °C

Figure 7-7 illustrates the friction test results under lubrication of SAE 30 oil at temperature of 60 °C. As the oil temperature is increased from 25 to 60 °C, its viscosity is decreased from 0.17 to 0.03 Pa·s. Comparing with Figure 7-6, it can be seen that the magnitude of average friction is reduced at oil temperature of 60 °C, especially under high speeds. This is attributed to the reduction of viscous shear force by the decrease in the lubricant viscosity. The friction reduction effect of the lasered pockets is also observed with a higher oil temperature (lower oil viscosity), and it is more noticeable at low speeds than at high speeds. This behavior can be explained by the friction reduction mechanism of the pockets. As the oil temperature is increased, the fluidity of the oil increases and the oil can flow off or be wiped off the cylinder wall more easily, which increases the degree of oil starvation at the piston ring/cylinder liner contact under low speeds and makes

the oil-reservoir effect of the pockets more distinct. On the other hand, the hydrodynamic lift generated by the pockets could be decreased at high speeds due to a lower oil viscosity.

Figure 7-8 shows typical friction force variation over two reciprocating cycles. As the speed is increased from 60 to 480 rpm, the friction force exhibits different trends. Under low speeds (60 rpm), the friction force reaches its highest value at the beginning and end of the reciprocating strokes (top and bottom dead centers), where the sliding velocity is the lowest and the friction is dominated by asperity contacts. Increasing the crank speed to 120 and 240 rpm results in lower friction spikes at dead centers and friction build-up around mid-stroke. This trend is attributed to increased hydrodynamic action at the piston ring/cylinder liner interface and the rise in viscous shear force due to higher sliding speeds. Further increase of the crank speed to 480 rpm leads to a friction trace with a sinusoidal shape. The asperity interaction is greatly reduced near the dead centers, and the friction force has its highest value in the middle of the stroke, where the sliding velocity is the highest throughout the reciprocating cycle. This indicates that the viscous shear force is dominant in the total friction under high speeds. Since shear force is proportional to the shear rate (sliding speed divided by the film thickness), a higher speed usually results in a higher shear force, although film thickness could also increase with speed but this effect is less significant than the impact of increased speed.

Comparison of the friction traces for smooth and pocketed piston rings show that the friction reduction effects of the pockets vary depending on the operating conditions. At lower speeds, their major effect is to reduce the friction spikes near the dead centers. However, at higher speeds, they can help lower the magnitude of the hump in the friction trace that occurs around the mid-stroke. These two effects can be explained by the friction reduction mechanisms of the laser pockets discussed above.

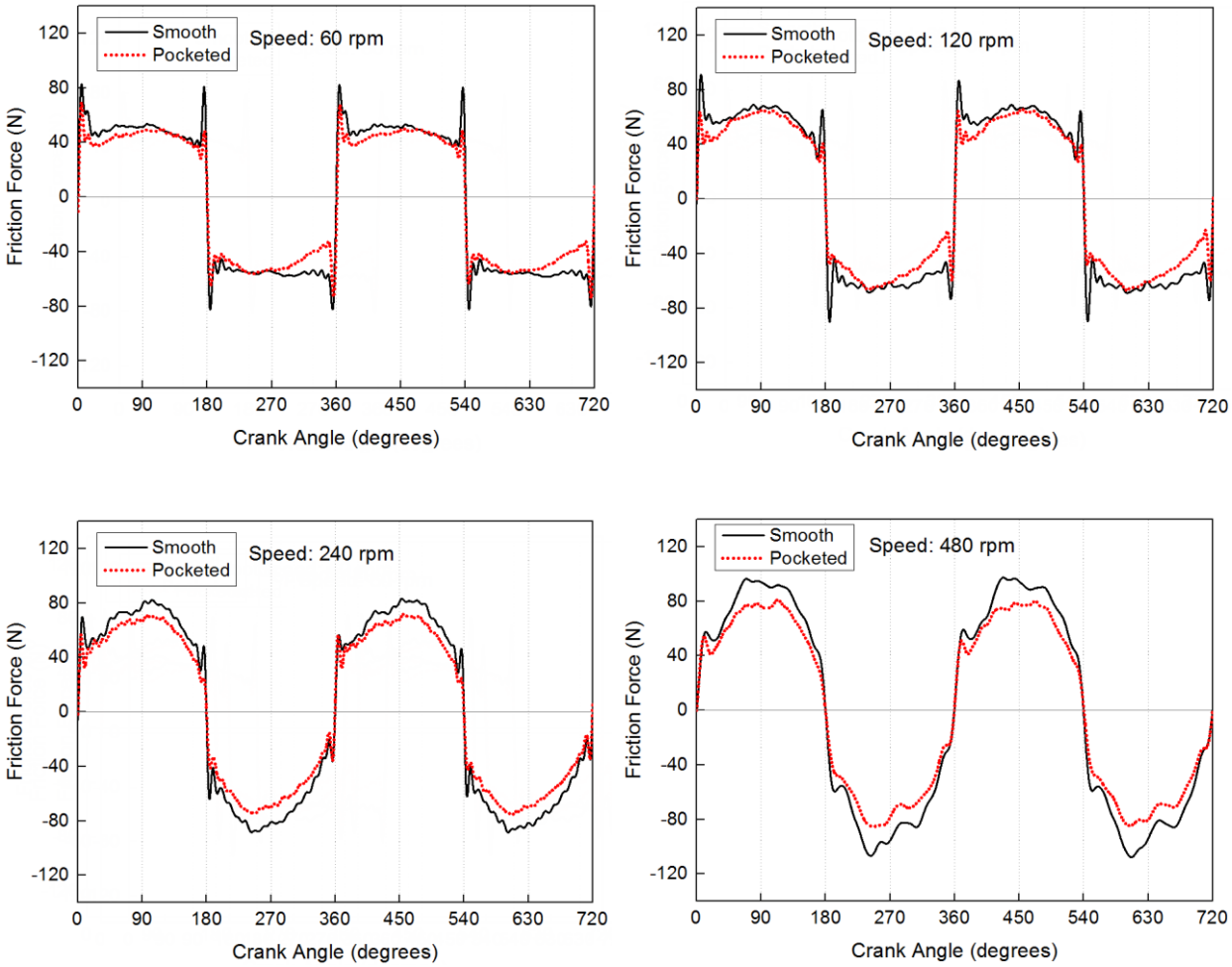

Figure 7-8 Friction force variation over two reciprocating cycles at oil temperature of 25 °C

7.3.2 Pressure Test Results

Compression pressure tests were performed to evaluate the effects of lasered pockets on the sealing performance of piston rings. The cylinder pressure was measured with a pressure transducer at crank speeds of 120, 180, 240 and 360 rpm. For each test condition, the cylinder pressure was recorded for 100 cycles with 1000 data points per cycle. Figure 7-9 show typical pressure variation of both smooth and pocketed piston rings. The peak cylinder pressure occurs around the top dead center and its value is extracted from the pressure traces to assess thee sealing performance. Figure 7-10 shows the averaged peak pressure of 100 cycles for smooth and pocketed piston rings. As

can be seen the peak pressure of the pocketed piston rings is consistently higher than that of the smooth rings. This suggests that the lasered pockets do not have detrimental effects on the sealing performance of the piston rings. On the contrary, they could improve the cylinder's compression to some extent. One possible reason for that is the oil stored in the pockets can be supplied to the contact surface under starved lubrication and fill some of the gap between piston ring and cylinder wall, which helps to improve the sealing at the interface.

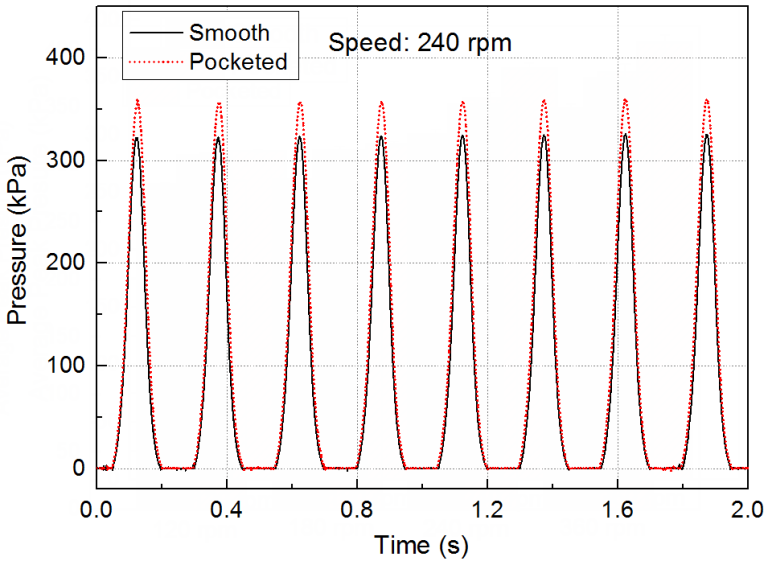

Figure 7-9 Chamber pressure variation at the speed of 240 rpm

After all experimental tests, the pocketed piston rings were taken out of the test rig and the wear of the pockets was assessed with a microscope. Figure 7-11 shows the piston ring surface after the tests. It can be seen that some pockets on the cast iron ring were worn during the tests while those on the ring with chrome coatings were still in a good condition after the experiments. This implies that the hard coatings of chrome helps protect the features of lasered pockets and improve their durability. Therefore, it is suggested that lasered pockets be used with hard coatings for the friction reduction of piston rings in practical applications.

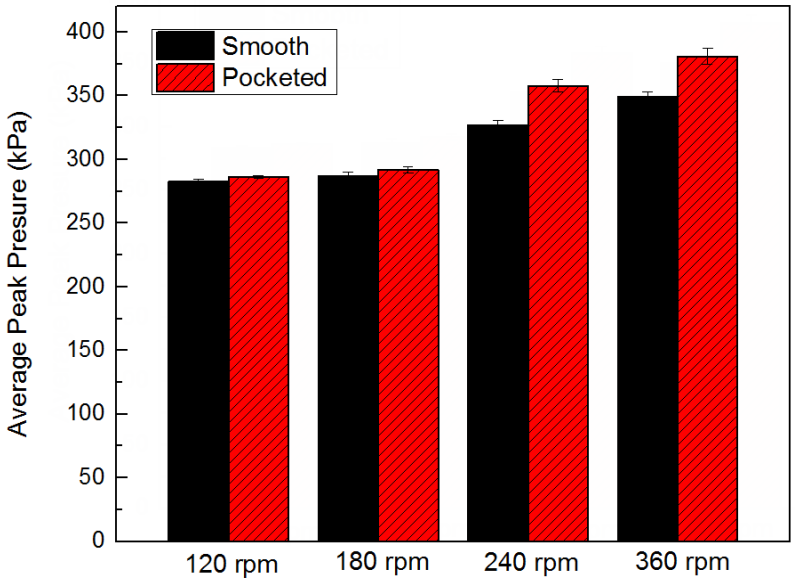

Figure 7-10 Comparison of averaged peak pressure

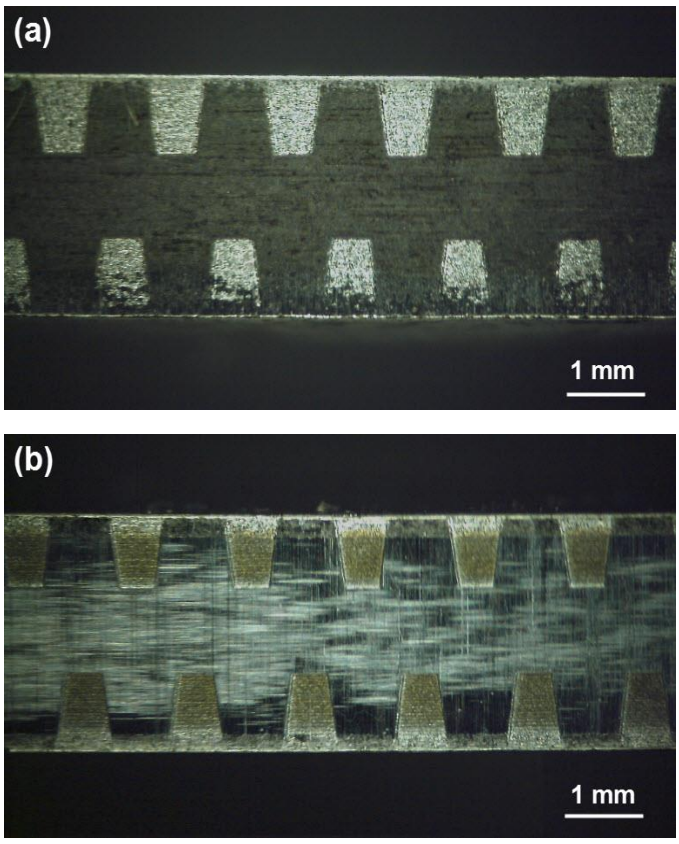

Figure 7-11 Piston ring surface after the tests: (a) without coatings (b) with chrome coating

7.4 Conclusions

An experimental study was performed to investigate the effect of lasered pockets on the frictional and sealing performance of production piston rings. The piston ring set, piston, cylinder liner and connecting rod from a diesel engine were utilized in a newly developed test apparatus for the measurement of friction force and compression pressure. Micro-pockets with optimal geometries were selected based on a previous study and fabricated on the running surface of compression rings using a laser. The friction test results show that lasered pockets lead to a reduction of 11–15% in the total friction between cylinder liner and piston assembly over a wide speed range. This effect can be attributed to mechanisms of the pockets which can act as micro oil reservoirs under starved lubrication and work as tiny step bearings under full film lubrication. The compression pressure test results show that sealing performance of the piston rings was not reduced by the pockets. On the contrary, they can improve compression in the cylinder to some extent. Observation of wear damage on the piston ring surface suggests that hard coatings can help improve the durability of lasered pockets.

7.5 References

[1] Etsion, I., Kligerman Y., 1999, "Analytical and experimental investigation of laser-textured mechanical seal faces," Tribol. Trans., 42(3), pp. 511–516.

[2] Wang X., Kato K., 2003, "Improving the anti-seizure ability of SiC seal in water with RIE texturing," Tribol. Lett., 14, pp. 275–280.

[3] Lu, X., Khonsari, M.M., 2007, "An experimental investigation of dimple effect on the stribeck curve of journal bearings," Tribol. Lett., 27, pp. 169–176.

[4] Tala-Ighil, N., Fillon M., 2015, "A numerical investigation of both thermal and texturing surface effects on the journal bearings static characteristics," Tribol. Int., 90, pp. 211–219.

[5] Wang X., Kato K., Adachi K., Aizawa K., 2003, " Loads carrying capacity map for the surface texture design of SiC thrust bearing sliding in water," Tribol. Int., 36, pp. 189–97.

[6] Herry, Y., Bouyer, J., Fillon M., 2015, "An experimental analysis of the hydrodynamic contribution of textured thrust bearings during steady-state operation: A comparison with the untextured parallel surface configuration," Proc. IMechE. Part J: J. Engineering Tribology, 229, pp. 362-375.

[7] Ling, T.D., Liu, P., Grzina D., Cao, J., Wang Q.J., 2013, "Surface texturing of drill bits for adhesion reduction and tool life enhancement," Tribol. Lett., 52, pp. 113–122.

[8] Chyr, A., Qiu M., Speltz, J.M., Jacobsen R.L., Sanders, A.P., Raeymaekers, B., 2014, "A patterned microtexture to reduce friction and increase longevity of prosthetic hip joints," Wear, 315, pp.51-57.

[9] Ryk, G., Kligerman, Y., Etsion, I., 2002, "Experimental investigation of laser surface texturing for reciprocating automotive components," Tribol.Trans., 45(4), pp. 444–449.

[10] Ryk G., Kligerman Y., Etsion I., Shinkarenko A., 2005, "Experimental investigation of partial laser surface texturing for piston rings friction reduction," Tribol.Trans., 48(4), pp.583–588.

[11] Ryk G., Etsion I., 2006, "Testing piston rings with partial laser surface texturing for friction reduction," Wear, 261(7-8), pp.792–796.

[12] Etsion, I., and Sher, E., 2009, "Improving fuel efficiency with laser surface textured piston rings," Tribol. Int., 42(4), pp. 542–547.

[13] Bolander, N. W., Sadeghi, F., 2006, "Surface modification for piston ring and liner," IUTAM Symposium on Elastohydrodynamics and Microelastohydrodynamics, Snidle R.W. and Evans H.P., eds., Springer, The Netherlands, pp. 271–283.

[14] Gadeschi G.B., Backhaus K., Knoll G., 2012, Numerical analysis of laser-textured piston-rings in the hydrodynamic lubrication regime," ASME J. Tribol., 134, pp. 041702.

[15] Tomanik E., 2013, "Modelling the hydrodynamic support of cylinder bore and piston rings with laser textured surfaces," Tribol. Int., 59, pp. 90–96.

[16] Zavos A.B., Nikolakopoulos P.G., 2015, "Simulation of piston ring tribology with surface texturing for internal combustion engines," Lubr. Sci., 27(3), pp. 151-176.

[17] Vladescu S.C., Medina, S., Olver A.V., Pegg, I.G., Reddyhoff, T., 2016, "Lubricant film thickness and friction force measurements in a laser surface textured reciprocating line contact simulating the piston ring–liner pairing," Tribol. Int., 98, pp. 317-329.

[18] Vladescu S.C., Olver A.V., Pegg, I.G., Reddyhoff, T., 2016, "Combined friction and wear reduction in a reciprocating contact through laser surface texturing," Wear, 358, pp. 51-61.

[19] Gu, C., Meng, X., Xie, Y., Fan, J., 2016, "A thermal mixed lubrication model to study the textured ring/liner conjunction," Tribol. Int., 101, pp. 178-179.

[20] Shen C., Khonsari, M.M., 2016, "The effect of laser machined pockets on the lubrication of piston ring prototypes," Tribol. Int., 101, pp. 273-283.

[21] Taylor, R.I., Evans, P.G., 2004, "In-situ piston measurements," Proc. IMechE, Part J: J. Engineering Tribology, 218, pp. 185-200.

[22] Liao, K., Liu, Y., Kim, D., Urzua, P., Tian, T., 2012, "Practical challenges in determining piston ring friction," Proc. IMechE, Part J: J. Engineering Tribology, 227, pp. 112–125.

[23] Gore, M., Theaker, M., Howell-Smith, S., Rahnejat, H., King, P.D., 2014, "Direct measurement of piston friction of internal-combustion engines using the floating-liner principle," Proc. IMechE, Part D: J. Automob Eng, 228, pp. 344–354.

CHAPTER 8 SUMMARY AND FUTURE WORKS

8.1 Summary

In this dissertation, novel designs of surface textures are proposed, fabricated and investigated for the enhancement of tribological performance. The research focuses on three subtopics: texture internal structure, texture shape optimization and new texture design for piston rings. A summary of main results is given in the following sections.

8.1.1 Texture Internal Structure

- The choice of cavitation pressure can strongly influence the simulation results from Elrod algorithm which implements the JFO theory. The JFO model using cavitation pressure of 90 kPa usually overestimates the cavitation region and underestimates the load-carrying capacity. Low gaseous cavitation pressure around 30 kPa is more reasonable in many cases.
- Based on the mechanism of cavitation, it is proposed that the cavitation pressure in steady-state lubrication film is affected by the gas supply from the oil film. If the gas emitted from lubricant film is sufficient to form the cavitation zone, the cavitation pressure will be close to ambient pressure. Otherwise, a sub-ambient pressure, as low as 30 kPa, can be reached.
- An approach to fabricate dimples with different profiles is developed using a laser device. Experimental results show that the dimple internal structure has a profound influence on the load-carrying capacity (LCC) and the cylindrical dimple with a rectangular profile is the better than dimples with triangular profiles for LCC.
- The numerical simulation results show that a possible reason for the higher LCC of cylindrical dimples is that the step shape in the profile is more efficient for building up hydrodynamic pressure than the wedge shape.

8.1.2 Texture Shape Optimization

- A numerical optimization approach based on the SQP algorithm is developed for the texture shape optimization of parallel surfaces. The results show that the optimum directional textures for unidirectional sliding have chevron-shapes with flat fronts while the optimum symmetric textures for bidirectional sliding is composed of pairs of the trapezoid-like shapes.
- The performances of optimum textures are compared with regular texture shapes using a mass-conservative algorithm. Simulation results show that the proposed optimum symmetric shape always have greater LCC than the regular shapes at area ratio of 30%, but its advantage diminishes as the area ratio is decreased.
- The shape optimization algorithm is further applied to a ring-shape geometry using the polar coordinates. The results show that the optimum textures of different area ratios (AR) have similar chevron-shapes with flat fronts.
- Experiments are carried out to compare the tribological performances of optimum texture shape (AR = 20%) with those of regular shapes. It is shown that the optimal texture shape has superior performance in terms of lower friction coefficient and lower lift-off speed.

8.1.3 New Texture Design for Piston Rings

- A new design of laser pocketed piston rings for the friction reduction at the piston ring/cylinder liner (PRCL) interface is proposed. Frictional performances of pockets with different geometric parameters are evaluated in a tribometer. The test results show that the pocket area ratio and depth have a major influence on the frictional behavior while the effect of the pocket shape is very limited.

- Numerical simulations, based on the mass-conservative model of Elrod and Adams, are also performed to investigate the effect of pocket geometric parameters on the fluid lubrication. The simulation results agree with the trend in experimental results.
- The design of lasered pockets is applied to the production piston rings and its effect on the frictional and sealing performance is evaluated with a motorized engine test apparatus. The test results show that lasered pockets lead to a reduction of 11-15% in the total friction and a slightly improved sealing capability of the rings.

8.2 Recommendation of Future Works

Surface texture design and optimization is an important topic in the development of surface texturing technology, because textures with optimal geometries could maximize their beneficial effects on the tribological performance. More research work is needed to fully understand the design principle of surface textures in different applications. The following recommendations are given for potential future work:

- In the comparison of dimples with different internal structural shapes, the maximum depths of dimples are kept the same in current study. Comparison can also be made between dimples with the same volume but different profiles in order to eliminate the possible influence from the dimple volume.
- The texture shape optimization with JFO boundary condition and with consideration of thermal effects needs to be studied.
- Minimizing the friction coefficient can be used as an objective function for texture shape optimization, and a multiple-texture model could be applied in the simulation to take account the interaction between textures.

- The effect of laser machined pockets on the performance of barrel-shaped piston ring needs to be investigated thoroughly.
- New designs of surface texturing can be developed for the oil control ring and piston skirt in order to further reduce engine friction.

APPENDIX LETTER OF PERMISSION TO USE PUBLISHED MATERIAL

Letter of Permission for Chapter 2

SPRINGER LICENSE
TERMS AND CONDITIONS

May 20, 2016

This Agreement between Cong Shen ("You") and Springer ("Springer") consists of your license details and the terms and conditions provided by Springer and Copyright Clearance Center.

License Number	3873280173220
License date	May 20, 2016
Licensed Content Publisher	Springer
Licensed Content Publication	Tribology Letters
Licensed Content Title	On the Magnitude of Cavitation Pressure of Steady-State Lubrication
Licensed Content Author	Cong Shen
Licensed Content Date	Jan 1, 2013
Licensed Content Volume Number	51
Licensed Content Issue Number	1
Type of Use	Thesis/Dissertation
Portion	Full text
Number of copies	1
Author of this Springer article	Yes and you are the sole author of the new work
Order reference number	None
Title of your thesis / dissertation	DESIGN OF SURFACE TEXTURE FOR THE ENHANCEMENT OF TRIBOLOGICAL PERFORMANCE
Expected completion date	Jun 2016
Estimated size(pages)	200
Requestor Location	Cong Shen Patrick Taylor Hall Louisiana State University BATON ROUGE, LA 70803 United States Attn: Cong Shen
Billing Type	Invoice
Total	0.00 USD

Letter of Permission for Chapter 3

SPRINGER LICENSE
TERMS AND CONDITIONS

May 20, 2016

This Agreement between Cong Shen ("You") and Springer ("Springer") consists of your license details and the terms and conditions provided by Springer and Copyright Clearance Center.

License Number	3873281012521
License date	May 20, 2016
Licensed Content Publisher	Springer
Licensed Content Publication	Tribology Letters
Licensed Content Title	Effect of Dimple’s Internal Structure on Hydrodynamic Lubrication
Licensed Content Author	Cong Shen
Licensed Content Date	Jan 1, 2013
Licensed Content Volume Number	52
Licensed Content Issue Number	3
Type of Use	Thesis/Dissertation
Portion	Full text
Number of copies	1
Author of this Springer article	Yes and you are the sole author of the new work
Order reference number	None
Title of your thesis / dissertation	DESIGN OF SURFACE TEXTURE FOR THE ENHANCEMENT OF TRIBOLOGICAL PERFORMANCE
Expected completion date	Jun 2016
Estimated size(pages)	200
Requestor Location	Cong Shen 3942 Gourrier Ave Apt 245 BATON ROUGE, LA 70808 United States Attn: Cong Shen
Billing Type	Invoice
Total	0.00 USD

Letter of Permission for Chapter 4

ELSEVIER LICENSE
TERMS AND CONDITIONS

May 20, 2016

This is a License Agreement between Cong Shen ("You") and Elsevier ("Elsevier") provided by Copyright Clearance Center ("CCC"). The license consists of your order details, the terms and conditions provided by Elsevier, and the payment terms and conditions.

All payments must be made in full to CCC. For payment instructions, please see information listed at the bottom of this form.

Supplier	Elsevier Limited The Boulevard,Langford Lane Kidlington,Oxford,OX5 1GB,UK
Registered Company Number	1982084
Customer name	Cong Shen
License number	3873290065657
License date	May 20, 2016
Licensed content publisher	Elsevier
Licensed content publication	Tribology International
Licensed content title	Numerical optimization of texture shape for parallel surfaces under unidirectional and bidirectional sliding
Licensed content author	Cong Shen,M.M. Khonsari
Licensed content date	February 2015
Licensed content volume number	82
Licensed content issue number	n/a
Number of pages	11
Start Page	1
End Page	11
Type of Use	reuse in a thesis/dissertation
Intended publisher of new work	other
Portion	full article
Format	both print and electronic
Are you the author of this Elsevier article?	Yes
Will you be translating?	No
Title of your thesis/dissertation	DESIGN OF SURFACE TEXTURE FOR THE ENHANCEMENT OF TRIBOLOGICAL PERFORMANCE
Expected completion date	Jun 2016
Estimated size (number of pages)	200
Elsevier VAT number	GB 494 6272 12
Permissions price	0.00 USD

VAT/Local Sales Tax	0.00 USD / 0.00 GBP
Total	0.00 USD

Letter of Permission for Chapter 6

ELSEVIER LICENSE
TERMS AND CONDITIONS

May 20, 2016

This is a License Agreement between Cong Shen ("You") and Elsevier ("Elsevier") provided by Copyright Clearance Center ("CCC"). The license consists of your order details, the terms and conditions provided by Elsevier, and the payment terms and conditions.

All payments must be made in full to CCC. For payment instructions, please see information listed at the bottom of this form.

Supplier	Elsevier Limited The Boulevard,Langford Lane Kidlington,Oxford,OX5 1GB,UK
Registered Company Number	1982084
Customer name	Cong Shen
License number	3873290369308
License date	May 20, 2016
Licensed content publisher	Elsevier
Licensed content publication	Tribology International
Licensed content title	The effect of laser machined pockets on the lubrication of piston ring prototypes
Licensed content author	Cong Shen,M.M. Khonsari
Licensed content date	September 2016
Licensed content volume number	101
Licensed content issue number	n/a
Number of pages	11
Start Page	273
End Page	283
Type of Use	reuse in a thesis/dissertation
Intended publisher of new work	other
Portion	full article
Format	both print and electronic
Are you the author of this Elsevier article?	Yes
Will you be translating?	No

Title of your thesis/dissertation	DESIGN OF SURFACE TEXTURE FOR THE ENHANCEMENT OF TRIBOLOGICAL PERFORMANCE
Expected completion date	Jun 2016
Estimated size (number of pages)	200
Elsevier VAT number	GB 494 6272 12
Permissions price	0.00 USD
VAT/Local Sales Tax	0.00 USD / 0.00 GBP
Total	0.00 USD

VITA

Cong Shen was born in Jiangsu, China. He received Bachelor of Engineering from Nanjing University of Aeronautics & Astronautics in 2007. In March 2010, he received Master's degree from the same university majored in mechanical engineering. In August 2010, he started to pursue his doctoral study in the Department of Mechanical and Industrial Engineering of Louisiana State University under the guidance of Dr. Michael M. Khonsari. Since then, he has conducted a series of studies in the field of tribology and published six journal papers. Cong Shen is expected to receive his Doctor of Philosophy degree at the 2016 Summer Commencement.